Passive Cooling System: An Integrated Solution to the Application in Power Electronics

by

Zhongchen Zhang

B. Eng, Beijing University of Technology, 2017

Thesis Submitted in Partial Fulfillment of the
Requirements for the Degree of
Master of Applied Science

in the
School of Mechatronic Systems Engineering
Faculty of Applied Sciences

SIMON FRASER UNIVERSITY
[Fall 2019]

Approval

Name:	**Zhongchen Zhang**
Degree:	**Master of Applied Science**
Title:	**Passive Cooling System: An Integrated Solution to the Application in Power Electronics**
Examining Committee:	**Chair:** Amr Marzouk Lecturer
	Majid Bahrami Senior Supervisor Professor
	Jiacheng (Jason) Wang Supervisor Assistant Professor
	Mehrdad Moallem Internal Examiner Professor
Date Defended/Approved:	September 6th, 2019

Abstract

Passive cooling systems are commonly used in power electronic industries to dissipate the tremendous excess heat generated in semiconductors devices to maintain the efficiency, reduce the thermal stress, and prevent the thermal runaway along with component failures. This research, which has been collaborated with our industrial partner, Delta-Q Technologies, aims to enhance the overall heat rejection capacity of a commercially-available naturally cooled battery charger heat sink by focusing on the fundamental heat transfer mechanisms of thermal radiation and natural convection at the same time.

In this study, the effect of anodization in various types of aluminum alloy (die-cast A380, 6061) and its thermal impact was investigated. The thermal emissivity of anodized samples was measured with Fourier Transform Infrared Reflectometer (FTIR) spectroscopy. A customized test chamber was built in our lab to carry out the steady-state thermal tests. A conjugated numerical heat transfer model was developed in Ansys Fluent in case of both natural convection and thermal radiation. Various novel fin geometries for Naturally Cooled Heat Sinks (NCHx) were also designed, prototyped, tested, and compared in terms of different surface conditions and operational orientations. A sensitivity analysis of geometrical parameters in one of the most promising fin geometries, inclined interrupted fins, was performed and analyzed. The results reveal an up to 27% overall enhancement with regard to the current IC650 design (benchmark case).

Keywords: Thermal radiation; Natural convection; Naturally Cooled Heat Sinks (NCHx); Anodization; Die-cast aluminum; Power electronics

To my beloved parents

Acknowledgment

I would like to express my deep gratitude towards my senior supervisor, Dr. Majid Bahrami, for providing me this opportunity to study in this lab and making this thesis possible, and his kindly supports and guidance along the way. I also would like to thank Chris Botting and Eric Lau from Delta-Q Technologies, for their time and mentorship throughout this research, offering me the platform to work within the industry environment.

I also would like to thank my supervisory and examining committee, Dr. Jason Wang and Dr. Mehrdad Moallem, for their help and time to review and improve this thesis.

I would like to thank all my labmates and friends in Laboratory for Alternative Energy Conversion at Simon Fraser University. Their helps, supports, and kindness really make this journey unique and memorable.

Lastly, I would like Natural Sciences and Engineering Research Council of Canada (NSERC), British Columbia Innovation Council (BCIC), Delta-Q Technologies, and Simon Fraser University for their financial support for which I am truly grateful.

Table of Contents

Approval ii
Abstract iii
Dedication iv
Acknowledgment v
Table of Contents vi
List of Tables ix
List of Figures xi
List of Acronyms xiv
Nomenclature xv
Executive Summary xviii
Motivation xviii
Objectives and milestones: xix
Methodology xx
Contributions xxi

Chapter 1. Introduction 1
1.1. Power electronics 1
1.1.1. Heat losses 2
1.1.2. Component failures 3
1.1.3. Importance of thermal management 3
1.2. Passive cooling systems 4
1.2.1. Heat sinks 5
1.2.2. IC650 battery charger thermal design 7
1.3. Research motivations 7
1.4. Literature review 8
1.4.1. Thermal radiation from finned heat sinks 9
1.4.2. Anodization of aluminum and its alloys 10
1.4.3. Natural convection from finned heat sinks 12
Straight fins: 13
Inclined fins: 14
Interrupted fins: 16
Pin fins: 16
1.5. Research objectives and chapter contents 18

Chapter 2. Thermal impact of anodization and radiation 19
2.1. Sample preparation 19
2.2. Emissivity measurement 22
2.2.1. Background 22
2.2.2. Equipment 24
2.2.3. Results 25
2.3. Surface morphology 28
2.4. Experimental setup 31

2.4.1. Testbed 31
2.4.2. Uncertainty analysis 33
2.5. Numerical analysis 34
2.5.1. Assumptions 34
2.5.2. Governing equations 35
2.5.3. Boundary conditions 36
2.5.4. Numerical schemes 37
2.5.5. Mesh independence study 37
2.6. Results and discussion 39
2.6.1. Experimental results 39
2.6.2. Numerical results 41
2.7. Conclusion 43

Chapter 3. Comparison between various fin geometries under natural convection and thermal radiation 45
3.1. Problem statement 45
3.2. Heat sink prototyping 46
3.2.1. Die-cast manufacturing constrains 46
3.2.2. Geometrical details 46
3.3. Experimental setup 51
3.4. Numerical analysis 54
3.4.1. Mesh independence study 54
3.5. Results and discussion 55
3.5.1. Effect of fin geometries (ε=0.03) 55
3.5.2. Effect of surface anodization (ε=0.89) 58
3.6. Conclusion 65

Chapter 4. Thermal performance and parametric study of the Inclined interrupted finned heat sink 67
4.1. Problem statement 67
4.2. Methodology 68
4.2.1. Heat sink prototyping 69
4.3. Numerical analysis 69
4.4. Experimental setup 71
4.5. Results and discussion 73
4.5.1. Numerical model validation 73
4.5.2. Effect of fin spacing 74
4.5.3. Effect of fin inclined angle 75
4.5.4. Effect of column distance 77
4.5.5. Validation of parametric results 78
4.6. Conclusion 79

Chapter 5. Conclusions 80
5.1. Summary of thesis 80
5.2. Future works 81

References.....82

Appendix A. Spectral hemispherical emissivity.....92

Appendix B. Tabulated data from experiments of bare and anodized IC650 heat sinks.....94

Appendix C. Tabulated data from experiments of bare and anodized prototyped heat sinks.....95

List of Tables

Table 1.1 Typical value of the convection heat transfer coefficient [12] 5
Table 1.2 Literature review on the thermal radiation from finned heat sinks 10
Table 2.1 Amount of samples prepared with various types of anodization.....21
Table 3.1 Preliminary comparison for heat sinks with 40 to 60 mm tall fins in die-casting 46
Table 3.2 Comparison of geometrical dimensions between each heat sink 50
Table B1 Experimental data of bare IC650 heat sinks 94
Table B2 Experimental data of Type II-Balck anodized IC650 heat sinks 94
Table B3 Experimental data of Type III-Clear anodized IC650 heat sinks 94
Table C1 Experimental data of bare IC650 Inclined Fins at horizontal orientation 95
Table C2 Experimental data of bare IC650 Inclined Fins at Vertical orientation.....95
Table C3 Experimental data of bare IC650 Inclined Fins at Sideways orientation 95
Table C4 Experimental data of anodized IC650 Inclined Fins at Horizontal orientation .96
Table C5 Experimental data of anodized IC650 Inclined Fins at Vertical orientation 96
Table C6 Experimental data of anodized IC650 Inclined Fins at Sideways orientation ..96
Table C7 Experimental data of bare Inclined Interrupted Fins at Horizontal orientation .97
Table C8 Experimental data of bare Inclined Interrupted Fins at Vertical orientation 97
Table C9 Experimental data of bare Inclined Interrupted Fins at Sideways orientation..97
Table C10 Experimental data of anodized Inclined Interrupted Fins at Horizontal orientation 98
Table C11 Experimental data of anodized Inclined Interrupted Fins at Vertical orientation 98
Table C12 Experimental data of anodized Inclined Interrupted Fins at Sideways orientation 98
Table C13 Experimental data of bare Straight Interrupted Fins at Horizontal orientation 99
Table C14 Experimental data of bare Straight Interrupted Fins at Vertical orientation ...99
Table C15 Experimental data of bare Straight Interrupted Fins at Sideways orientation 99
Table C16 Experimental data of anodized Straight Interrupted Fins at Horizontal orientation 100
Table C17 Experimental data of anodized Straight Interrupted Fins at Vertical orientation. 100
Table C18 Experimental data of anodized Straight Interrupted Fins at Sideways orientation 100
Table C19 Experimental data of bare Pin Fins at Horizontal orientation 101

Table C20 Experimental data of bare Pin Fins at Vertical orientation 101
Table C21 Experimental data of bare Pin Fins at Sideways orientation 101
Table C22 Experimental data of anodized Pin Fins at Horizontal orientation 102
Table C23 Experimental data of anodized Pin Fins at Vertical orientation 102
Table C24 Experimental data of anodized Pin Fins at Sideways orientation 102
Table C25 Experimental data of bare Inclined Interrupted Fins [12 fins each column] tested at horizontal orientation outside the box 103
Table C26 Experimental data of bare Inclined Interrupted Fins [12 fins each column] tested at vertical orientation outside the box 103
Table C27 Experimental data of bare Inclined Interrupted Fins [12 fins each column] tested at sideways orientation outside the box 103
Table C28 Experimental data of bare Inclined Interrupted Fins [14 fins each column] tested at Horizontal orientation outside the box 104
Table C29 Experimental data of bare Inclined Interrupted Fins [14 fins each column] tested at Vertical orientation outside the box 104
Table C30 Experimental data of bare Inclined Interrupted Fins [14 fins each column] tested at Sideways orientation outside the box 104

List of Figures

Figure 1.1 Power electronics devices: (a) Vacuum tube; (b) Silicon controlled rectifier (SCR); (c) Capacitor; (d) Transformer 2

Figure 1.2 Various finned heat sinks with (a) continuous rectangular fins; (b) radial rectangular fins; (c) circular pin fins; (d) square pin fins 6

Figure 1.3 IC Series battery charger, Delta-Q Technologies 8

Figure 1.4 Schematic of Porous Anodic Aluminum Oxide (AAO) layers 11

Figure 1.5 Schematic of inclined fins, IC650 heat sink design, Delta-Q Technologies 14

Figure 1.6 Pin fin alignment: (a) Staggered; (b) In-line 17

Figure 2.1 IC650 heat sinks before and after various anodizing treatment, (a) Bare; (b) Type II-Black; (c) Type III-Clear 21

Figure 2.2 The SOC 400T Spectral Reflectometer 24

Figure 2.3 Total hemispherical emissivity of the metal surface, die-cast, and machined aluminum 26

Figure 2.4 Total hemispherical emissivity for various anodized die-cast Al alloy A380 sample surfaces 27

Figure 2.5 Total hemispherical emissivity for various anodized machined Al alloy 6061 sample surfaces 28

Figure 2.6 Two different surface morphology observed from unsealed anodic layer formed on die-cast Al alloy A380: (a) “Hexagonally packed cells”; (b) Porous and layer-stacked structure 30

Figure 2.7 Surface morphology of sealed anodized surface formed on die-cast Al alloy A380: (a)Type II-Black; (b) Type III-Clear 30

Figure 2.8 Surface morphology of unsealed anodized surface formed on machined Al alloy 6061 31

Figure 2.9 Schematic of the experimental setup, including locations of thermocouples and heating components (a) a customized-built test chamber; (b) back view of the tested heat sink 32

Figure 2.10 Components of the experimental setup 33

Figure 2.11 Unstructured conforming mesh elements of solid-solid (heating components and heat sink) and solid-fluid (heat sink and ambient fluid) interfaces 38

Figure 2.12 Mesh independency study, average temperature change with respect to the number of elements 39

Figure 2.13 Average temperature difference between the heat sink base and chamber ambient 40

Figure 2.14 Experimental data of average heat sink base temperature 40

Figure 2.15 Total thermal resistance in case of natural convection and thermal radiation from various tested heat sinks 41
Figure 2.16 Comparison between presented numerical model (solid lines) and experimental data (solid symbols) 42
Figure 2.17 Radiative heat transfer from bare and anodized heat sinks (a) Radiative heat transfer rate; (b) Percentage of the thermal radiation in overall heat dissipation 43
Figure 3.1 Prototyped heat sinks (a) IC650 design; (b) Inclined interrupted fins; (c)straight fins; (d) pin fins. 47
Figure 3.2 Preliminary parametrical study of pin spacing: (a) The varying trend of vertical to horizontal face to face spacing; (b) Effect of vertical face to face spacing on the average temperature difference 50
Figure 3.3 Schematic of testbed: (a) Assembled tested heat sink; (b) Split view of heat sink test substrate; (c) Location of thermocouples 52
Figure 3.4 Test orientations: (a) Horizontal; (b) Vertical; (c) Sideways 53
Figure 3.5 Experimental Setup in case of the anodized heat sink with IC650 fins tested at vertical orientation 53
Figure 3.6 Mesh independence studies of benchmark geometry 55
Figure 3.7 Comparison of experimental results (symbols) with numerical models (lines) of untreated heat sinks at three orientations: (a) Horizontal; (b) Vertical; (c) Sideways 58
Figure 3.8 Comparison of thermal performance of each prototyped heat sink before and after the anodization at all three orientations: (a) Current IC650 design; (b) Inclined interrupted fins; (c) Straight interrupted fins; (d) Pin fins..... 61
Figure 3.9 Comparison of experimental results (symbols) with numerical models (lines) of anodized heat sinks at three orientations: (a) Horizontal; (b) Vertical; (c) Sideways 63
Figure 3.10 Percentage of thermal radiative heat transfer in overall heat dissipation from various fin geometries at three orientations: (a) Horizontal; (b) Vertical; (c) Sideways..... 65
Figure 4.1 Schematic of heat sink comprised with inclined interrupted fins..... 68
Figure 4.2 Schematic of computational domain: (a) Computational domain; (b) Thermal input at the heat sink base 70
Figure 4.3 Mesh independency study of inclined interrupted fins, 12 fins in each column 71
Figure 4.4 Schematic of experimental setup: (a) Testbed; (b) Location of the thermocouples 72
Figure 4.5 Experimental setup for heat sink test in ambient with sideways placed inclined interrupted fins shown in figure..... 72

Figure 4.6 Comparison between the experimental data (solid symbols) and numerical model (lines) of inclined interrupted fins (fin number of 12 in each column) 74
Figure 4.7 Effect of fin spacing on the average heat sink base temperature with a thermal input of 80W 75
Figure 4.8 Effect of fin inclined angle on the fin width 76
Figure 4.9 Effect of fin inclined angle on the average heat sink base temperature with a thermal input of 80W 76
Figure 4.10 The varying fin spacing and fin width with regard to the column distance ... 77
Figure 4.11 Effect of column distance on the average heat sink base temperature with a thermal input of 80W 78
Figure 4.12 Schematic of inclined interrupted fins design with optimal fin spacing for horizontal orientation 78
Figure 4.13 Comparison between the experimental data (solid symbols) and numerical model (lines) of inclined interrupted fins (fin number of 14 in each column) 79
Figure 5.1 Proposed geometries in the parametric study for future work with various column numbers 81
Figure A1 Spectral hemispherical emissivity for aluminum alloys surfaces 92
Figure A2 Spectral hemispherical emissivity for die-cast Al alloy A380 surfaces after various types of anodization 92
Figure A3 Spectral hemispherical emissivity for machined Al alloy 6061 surfaces after various types of anodization 93
Figure A4 Bare and anodized die-cast aluminum A380 samples 93
Figure A5 Bare and anodized machined aluminum 6061 samples 93

List of Acronyms

AAO	Anodic aluminum oxide
CNC	Computer numerical control
CPCs	Compound parabolic concentrators
DOE	Design of experiments
DAQ	Data acquisition system
DTGS	Pyroelectric deuterated triglycine sulfate
EV	Electric vehicle
FTIR	Fourier transform infrared reflectometer
GTO	Gate turn-off thyristor
IC	Integrated circuit
LED	Light emitting diode
MTBF	Mean time between failures
MOSFETs	Metal oxide semiconductor field effect transistor
NCHx	Naturally cooled heat sinks
PCM	Phase change material
SCR	Silicon controlled rectifier
S2S	Surface to surface radiation model
TIM	Thermal interface material
TCR	Thermal contact resistance
URF	Under relaxation factors

Nomenclature

A	Surface area, [m^2]
c_p	Specific heat, [$J \cdot kg^{-1} \cdot K^{-1}$]
C_1	First radiation constant, [$3.74177 \times 10^8 W \cdot \mu m^4 \cdot m^{-2}$]
C_2	Second radiation constant, [$1.43878 \times 10^4 \mu m \cdot K$]
C_3	Third radiation constant, [2898 $\mu m \cdot K$]
D	Fin diameter, [m]
E	Emissive power
f	Frequency, [Hz]
F	View factor
g	Gravity acceleration, [$m \cdot s^{-2}$]
G	Fin gap distance, [m]
Gr	Grashof number
h	Heat transfer coefficient, [$W \cdot m^{-2} \cdot k^{-1}$]
H	Fin/heatsink height, [m]
I	Fin column distance, [m]
I_0	Current, [A]
J	Radiosity, [$W \cdot m^{-2}$]
k	Thermal conductivity, [$W \cdot m^{-1} \cdot K^{-1}$]
L	Fin/heatsink length, [m]
n	Fin number
N	Fin column number
Nu	Nusselt number
P	Pressure, [Pa]
P_0	Power, [W]
Pr	Prandtl number
q	Heat flux, [$W \cdot m^{-2}$]
Q	Heat transfer rate, [W]
R	Thermal resistance, [$K \cdot W^{-1}$]
R_e	Electrical resistance, [Ω]
Ra	Rayleigh number
S	Fin spacing, [m]
t	Thickness, [m]

T	Temperature, [K]
u	Velocity, [$m \cdot s^{-1}$]
U	Voltage, [A]
W	Fin/Heatsink width, [m]

Greek symbols

α	Thermal diffusivity, [$m^2 \cdot s^{-1}$]
β	Thermal expansion coefficient, [$1 \cdot K^{-1}$]
γ	Surface thermal reflectivity
δ	Absolute uncertainty
Δ	Difference in quantity
ε	Surface thermal emissivity
θ	Fin inclined angle, [degree]
λ	Wavelength, [μm]
ν	Kinematic Viscosity, [$m^2 \cdot s^{-1}$]
ρ	Density, [$kg \cdot m^{-3}$]
σ	Stefan-Boltzmann constant, [5.67×10^{-8} $W \cdot m^{-2} \cdot K^{-4}$]
τ	Surface transmissivity
Φ	Azimuthal angle, [degree]
χ	Surface visibility
ω	Zenith angle, [degree]

Subscripts

a, amb, ∞	Ambient properties
ave	Average properties
b	Fin bottom/Black body
base	Heat sink base properties
back	Heat sink back surface
bulk	Bulk resistance
c, con	Thermal convective heat transfer
front	Heat sink frontal surface
h	Horizontal properties
measured	Recorded spectrums for specimens
opt	Optimal properties

out	Heat flux leaving the surfaces
r, rad	Thermal radiative heat transfer
reference	Recorded spectrums for polished gold
source	Heat generation source
t	Fin top
v	Vertical properties
w	Wall properties
zero	Recorded spectrums for ambient

Executive Summary

Motivation

Thermal management plays a key role in electronic and power electronic industry since the heat generated in semiconductor devices, e.g., diodes, MOSFETs, transformers, and inductors, is a major limiting factor for maintaining their nominal performance and long-term reliable operation. In fact, half of the electronics failure is associated with inadequate temperature control and the need for efficient cooling is at peak loads. The global market for the cooling hardware, e.g., heat sinks and fans, is estimated to grow from $9.8 to $12.9 billion USD in the period of 2018 to 2023 with an annual growth rate of 5.5%, and accounts for 79% of the overall thermal management market share, which reflects the importance of efficient cooling technologies.

Passive cooling technologies has always been a preferred method for heat removal in power electronics equipment. As opposed to the active cooling system, it offers several supreme advantages including high reliability, noise-free operation, and zero-parasitic energy consumption due to the absence of external mechanical parts, e.g., fans and pumps, which makes it a “green” cooling approach. However, the relatively low heat transfer rate of passively cooled systems limits their broad applications, particularly in high power semiconductor devices due to the tremendous excess heat that needs to be dissipated to maintain the efficiency, reduce the thermal stress and prevent thermal runaway along with component failure. Pushing the limits of passive cooling capability is therefore much desired and rather urgent in the implementation of such heat transport/dissipation systems in reliable power electronics products.

In theory, the overall heat dissipation from a naturally cooled heat sinks (NCHx) occurs via the mechanisms of thermal radiation and natural convection. The former represents the heat that transfers in the form of electromagnetic radiation between the heat dissipating area (finned surfaces) and the ambient while the latter is the result of the fluid movement of the cooling medium caused by the density differences induced by the temperature gradients. They are both unique subjects worth studying in terms of improving the overall heat transfer rate. This thesis aims to explore the technologies in the scope of both thermal radiation and natural convection to address the needs for improving the

overall thermal performance of a passively cooled system in the application of power electronics industries.

Objectives and milestones:

The main goal of this study is to improve the overall heat transfer in a commercially-available naturally cooled battery charger, IC650 from Delta-Q Technologies, the industrial collaborator of this project, shown in Figure 1. The roadmap and components of this research project are shown in Figure 2. This study focuses on both radiation and natural convection heat transfer and includes the following milestones:

- Investigate the effect of different types of anodization on the thermal emissivity of both die-cast aluminum alloy A380 and machined aluminum alloy 6061;
- Establish an understanding of the impact and importance of thermal emissivity on thermal radiation in naturally cooled heat sinks (NCHx);
- Explore the potential heat transfer improvement of natural convection and thermal radiation from NCHx with various fin geometries and orientations; and
- Find an optimal fin arrangement for the inclined interrupted finned heat sink to maximize the overall heat transfer.

Figure 1: IC 650 Battery Charger from Delta-Q Technologies

Methodology

A systematic experimental-numerical approach is undertaken in this study. As shown in Figure. 2, this research project can be divided into three sub-projects: i) Effect of surface anodization, ii) Effect of various fin geometries, and iii) Parametric study of inclined interrupted finned heat sinks.

The first part focuses on the anodization of a die-cast aluminum alloy A380, which is currently used in Delta-Q Technologies products. The anodization was performed by a local BC vendor “Spectral Finishing Inc.”, and the thermal emissivity of anodized heat sinks was measured using a 400T Infrared Reflectometer, Surface Optics Corporation, available in Solar Thermal Research Laboratory (STRL), University of Waterloo, ON, Canada. In addition, the thermal radiative behavior for machined 6061 samples was also determined as comparisons. A customized thermal radiation-natural convection test chamber was built in our lab, the Laboratory for Alternative Energy Conversion (LAEC), to conduct the thermal tests of several anodized enclosures and heat sinks for the IC650 battery charger. A new numerical model has been developed in Ansys Fluent and validated using the experimental data collected in the testbed mentioned above. The validated model was then used to further investigate the effect of thermal emissivity on anodized IC650 heat sinks. The results showed that anodized die-cast aluminum naturally cooled heat sinks (NCHx) perform significantly better where a reduction up to 15% of overall thermal resistance can be seen compared to the identical untreated ones. Moreover, it has been observed that thermal radiation contributes 41% maximally to the total heat transfer in this particular design of passively cooled battery charger.

Four new NCHx with various fin geometries, with the same footprint of the existing Delta-Q IC650 battery charger, were designed, prototyped, and tested including: i) fins resembling the current IC650 design, ii) inclined interrupted fins, iii) straight interrupted fins, and IV) pin fins. The heat sinks were all built in-house in the School of Mechatronic Systems Engineering Machining Shop using computer numerical control (CNC) machining tools with aluminum alloy 6061.

A comprehensive experimental study is performed to examine the thermal performance of each NCHx before and after the anodization at various orientations, namely horizontal, vertical, and sideways. The numerical modeling results indicated a

notable potential improvement for each fin geometry contributed by natural convection and thermal radiation, respectively. In terms of natural convection, only inclined interrupted fins can provide the desired thermal improvement at all three orientations, horizontal, vertical and sideways compared to the original IC650 fin design, where the straight interrupted fins fail at sideways orientation, and the pin fins perform even worse except at horizontal orientation. In conclusion, the test results of anodized heat sinks show that an up to 27% enhancement can be achieved compared with current IC650 fin design (benchmark case) depending on the fin geometries and test orientations.

The last sub-subject of this research entails an in-depth study of inclined interrupted finned heat sinks. It follows the procedure of heat sink prototyping, experimental testing, and numerical modeling. A thorough parametric study on the impacts of fin spacing, fin width, inclined angle, and column spacing is carried out using the present verified numerical model under various orientations. An additional inclined interrupted finned heat sink is chosen based on the current modeling results and then prototyped and tested to verify the approaches developed in this study. The parametric study results show that optimal values do exist for fin spacing and column distance which varies based on the work orientations. On the other hand, the chosen of fin inclined angle should depend on the dominant working orientation where no universal optimal value is observed.

Contributions

The contributions of this study are stated below:

- Measured thermal emissivity of various types of anodized die-cast and machined aluminum samples and their impact on the performance;
- Conducted a comprehensive experimental study of natural convection and thermal radiation from NCHx with a number of fin geometries;
- Developed a numerical model capable of predicting the radiative and natural convective heat transfer from NCHx;
- Conducted a comprehensive parametric study of various geometrical parameters from the inclined interrupted finned heat sink.

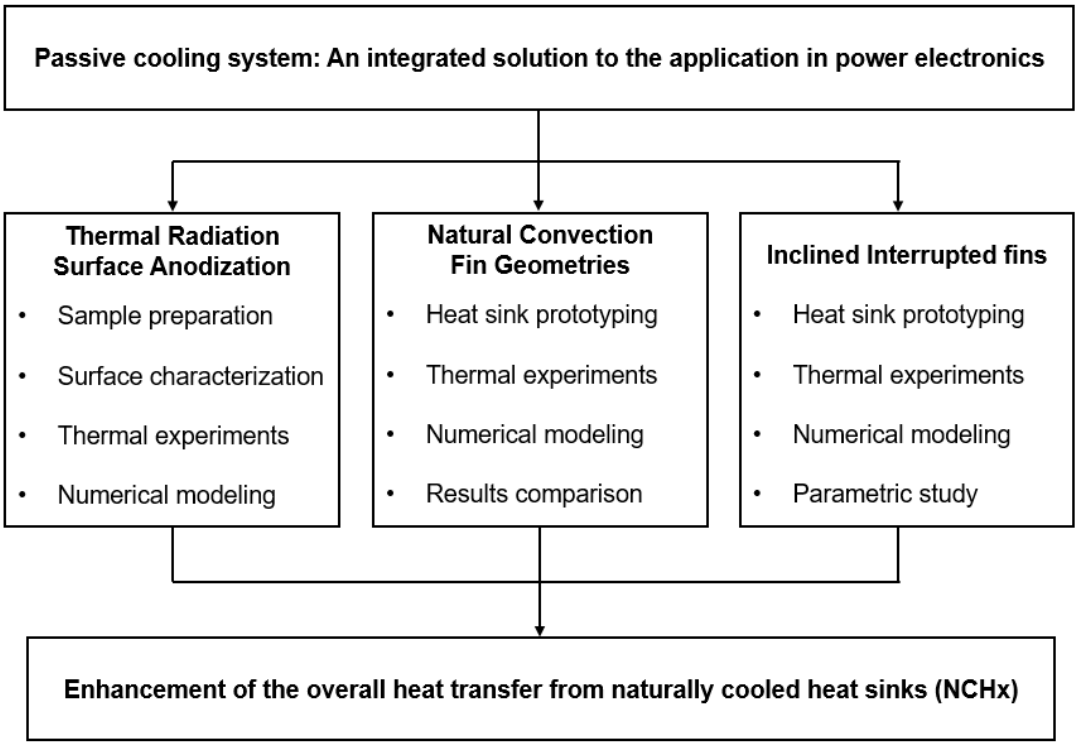

Figure 2: The present research road map

The publication resulted from this research up to date:

[1] Z. Zhang, M. Collins, C. Botting, E. Lau, and M. Bahrami, "The impact of anodization on the thermal performance of passively cooled electronic enclosures made of die-cast aluminum," 2019 35th Thermal Measurement, Modeling & Management Symposium (SEMI-THERM), San Jose, CA, 2019.

[2] Z. Zhang, M. Collins, E. Lau, C. Botting, and M. Bahrami, “The role of anodization in naturally cooled heat sinks for power electronic devices,” Journal of Heat Transfer, under review.

[3] Z. Zhang, E. Lau, C. Botting, and M. Bahrami, “Naturally cooled heat sinks for battery charger, ” International Journal of Heat and Mass Transfer, under review.

Chapter 1.

Introduction

1.1. Power electronics

Power electronics refers to the technologies that emphasize primarily on the control and conversion of electric power. It presents everywhere from our kitchen appliances, computers to large wind turbines and plays a central role in various modern engineering systems, including light emitting diode (LED), telecommunication, automotive, aerospace and renewable energy industries where the distribution and usage of electric energy are essential. Today's technologies advancement expedites our needs for power electronics. It estimates that at least 50% of generated electrical power in the USA flows through power electronic converters and an increase of share to 100% in the next few decades is expected [1]. The significance of power electronics in renewable energy systems is also worth noting, especially with the worldwide trend of electrification of transportation systems. The transition from the traditional combustion engine to the electric motor not only pose new challenges for onboard electronics such as DC/AC inverter, bidirectional DC/DC converter and battery management systems, also require fast ground charging facilities that operate safely and efficiently which becomes part of main focuses of power electronics industries in recent years. With expected global electric vehicle (EV) market grows to $127.7 billion USD by 2022 of growth rate 11.0% [2], the power electronics market is predicted to reach $51.1 billion USD at the end of 2023 [3].

The modern power electronics begin with the invention of the silicon controlled rectifier (SCR) in 1958. This semi-controlled power switch can only be turned on or off by a small electric pulse [1]. Soon after, several fully controlled semiconductor power switches, such as gate turn-off thyristor (GTO) and power metal oxide semiconductor field effect transistor (MOSFET) are introduced to the market. The basis of all semiconductor devices relies on one unique physical phenomenon, the electrical conductive behavior of semiconductor material that can be easily manipulated by deliberately adding atomic impurities, e.g., p-type silicon forms when small proportion of boron or gallium is doped to create excess holes having positive charges and n-type silicon can be doped with phosphorus or arsenic to form excess free electrons carrying negative chargers [4]. The

joint between p-type and n-type semiconductor is called p-n junction, which has the unique unidirectional electrical conducting property that is crucial to most modern-day electronics. Figure 1.1 shows some of the key components in the development of power electronic industries, from early-stage vacuum tube to solid-state devices. Attributing to the advent of semiconductor technologies, the acceleration of miniaturizing power electronics devices enables rapid development of consumer electronics market and also put forward a higher standard for integrating, packaging and regulating the power electronic equipment.

(a) (b) (c) (d)

Figure 1.1 Power electronics devices: (a) Vacuum tube; (b) Silicon controlled rectifier (SCR); (c) Capacitor; (d) Transformer

1.1.1. Heat losses

The energy losses in electrical systems are universal, and the efficiency of power electronic devices are much improved over the years. However, it is unavoidable and always dissipated by unwanted effects, mostly in the form of heat or effects that end up causing temperature rises in the components. There are several mechanisms for heat generation in different types of electronic devices.

Joule heating [5] is a generic heat generation process due to the resistance along the conductor. The superconductor is an exceptional case where the extreme condition is demanded to reach zero electrical resistance state. The Joule's first law, named after British physicist James Prescott Joule, describe that the generated heat by an electrical conductor is proportional to the square of the current and its electrical resistance (R_e), the mathematic formulation as:

$$P_0 \propto {I_0}^2 R_e \tag{1.1}$$

Switching loss occurs in transistors and fast switching diodes when significant voltage and current coexist simultaneously at switch terminals during the phase from on to off and vice versa, especially in high switch frequency [6]. The switching power losses

are proportional to switching frequency (f) and the square of the power supply voltage (U). Other than switching losses, heat dissipation due to dynamic short circuit and leakage current are also the key contributors to the overall power consumption in transistors.

For wound components, e.g., transformers and inductors, heat losses mostly comprise of two parts, the copper losses which are the joule heating in the winding wires and the core losses induced by the alternating magnetic field, i.e., eddy currents and hysteresis losses [5]. It is also crucial to improve the electrical core performance to reach the desired efficiency. It is assumed that no power losses for ideal capacitors under the DC current. Though in reality, some resistance and inductance are observed, and it will result in temperature rises [7].

1.1.2. Component failures

When lost energy in an electric circuit are gathered in the form of heat inside the devices and are not efficiently transferred out, the temperature will rise. If temperature breaks certain limits, devices may burn or catch on fire and will experience severe function failure. It is reported that more than half of malfunctions in modern electronics is associated with poor temperature control or thermal regulation [8]. In fact, there are three main types of component failures dependent on device temperature, which are mechanical, corrosion, and electrical failures [7].

The mechanical failures are led by the excessive deformation in devices, e.g., fractures, cracks, and separation of joints, because of different thermal expansion rate that presents in two different materials, i.e., die and substrate. The corrosion failure refers to the expedited process of aluminum oxidation or wet corrosion in a moisture environment due to the high temperature resulted from waste heat accumulation. The electrical failure is directly contributed by the fact that temperature has an inverse effect and will exert excess on-resistance and overstress on the components [7]. It will deteriorate as temperature increases, which is known as thermal runaway.

1.1.3. Importance of thermal management

In all, operation of the power electronics systems under their maximum allowable temperature is beneficial and will reduce the Mean Time Between Failures (MTBF)

exponentially [7]. Proper thermal management will not only improve the components' performance and reliability but also will expand their operational life expectancy and reduce the operational cost accumulatively. With the trend of decreasing the size and increasing power density in semiconductor devices, effective and efficient thermal management technologies will always be at the center of the power electronics industry.

1.2. Passive cooling systems

The main goal of thermal management in electronic systems is to remove generated excess heat out of electric circuits and prevent any overheating of the component that may negate the full system. During the thermal design process, thermal management ideally should not be the motivation behind the new design, but it needs to be incorporated into the preliminary stage with requirements and constraints that may have a more noticeable impact other than an afterthought. The selection of heat transfer technique used to cool electronics depends on the application, desired heat removal capacity, reliability, and most substantially, the cost. Therefore, cooling technologies must be cost-effective and introduce minimum complexity to the level of integrated circuit (IC), packaging, and operation where it can be economically justified.

The passive cooling systems are the most widely accepted and recognized system to deal with waste heat in power electronic devices. They comprise of one or more passive heat removal methods, such as natural convection air/liquid cooling, thermal radiation, heat pipes, vapor chambers or thermal storage with phase change materials (PCM) [9]. The driving force for those techniques is derived from the temperature gradient between the heat source and cooling medium and in aid of either gravity or phase transition, where the assistance from the external moving mechanical part is no longer needed. As a result of the elimination of moving mechanisms, they offer supreme advantages including noiseless operation, zero parasitic energy consumption, low-cost and high reliability. Especially in the application of harsh environment, e.g., automotive, military and oil exploration, a reliable yet capable cooling solution is required and craved [10] [11] where the improved passive cooling systems can fulfill the needs.

However, passive cooling systems have their limitations regardless of all the preferred features in the design and management of power electronics devices. For example, natural convection is a type of heat transport phenomenon driven by density

change due to the temperature difference between the heat source and adjacent cooling mediums, e.g., air, water, or cooling oil. The amount of heat that can be dissipated is dictated by temperature gradient itself which means it can only be applied to the case either the maximum allowable temperature is high or less cooling capacity is acceptable in the trade-off of reliability. Table 1.1 lists some of the typical value of heat transfer coefficient in convection. Forced convection undoubtedly has more prominent heat transfer capability due to the fact it is driven by pressure difference stirred by moving mechanical parts, i.e., fans or pumps.

Table 1.1 Typical value of the convection heat transfer coefficient [12]

Type of convection		Low end ($W \cdot m^{-2} \cdot K^{-1}$)	High end ($W \cdot m^{-2} \cdot K^{-1}$)
Free convection of	gases	2	25
	liquids	10	1000
Forced convection of	gases	25	250
	liquids	50	20000
Boiling and condensation		2500	100000

1.2.1. Heat sinks

Heat sinks, as an energy exchange device, are often used in passive cooling systems. As a collection of extended surfaces (fins), the heat sink can maximize the contact surface area with adjacent cooling medium and dissipate heat effectively and efficiently. In reality, almost all power electronic devices either incorporate various types of heat sink into the chassis or directly mount on the circuit board to remove waste heat timely.

Aluminum and its alloys are the most commonly used material to manufacture heat sinks because they are relatively low cost, mechanically robust and most importantly, of high thermal conductivity. In mass production, the majority of aluminum heat sinks are made either from extrusion or die-cast process. Due to the significant difference between these manufacturing processes, aluminum alloys that suitable for the die-cast procedure are relatively low thermally conductive ($k \leq 115$ $W \cdot m^{-1} \cdot K^{-1}$), partially because of add-in impurities and non-metal elements, compared to the aluminum extrusion ($k \geq 150$ $W \cdot m^{-}$

$^{1}\cdot K^{-1}$). This will have an adverse impact on heat spreading out/through the heat sink, i.e., increasing spreading resistance and bulk resistance.

At the same time, the fins on a heat sink come in different geometries and surface finishes. Due to manufacturing cost and thermal performance, continuous rectangular fins are the most popular choice while cylindrical/elliptical/square pin fins and interrupted fins are also seen on the market. Most commercial available finned heat sink used in electronic products can be found in Figure 1.2. Fin shape has a decisive impact on heat sink performance, especially for natural convection. Given the fact that the minute density difference is the driving force for the airflow in naturally cooled heat sinks (NCHx), the poor selection of fin geometry can pose more resistance that impedes airflow and minimizes convective heat transfer rate, i.e., higher film resistance. When a finned heat sink is designed to operate at two or more orientations, the fin design needs to be justified, and optimization may be required. Literature review on the related topic is presented in section 1.4.

(a) (b) (c) (d)

Figure 1.2 Various finned heat sinks with (a) continuous rectangular fins; (b) radial rectangular fins; (c) circular pin fins; (d) square pin fins

Surface finish is also crucial for naturally cooled heat sinks because large portions of heat can be dissipated by thermal radiation. The thermal emissivity depends on the surface condition of heat sinks. It assumes that the surface of most electrically conductive material is of low thermal emissivity [12], especially the raw metal surface. General value for the machined and extruded metal surface is nearly zero so that most of the studies of natural convection from finned heat sink are reasonable enough to neglect the effect of thermal radiation. However, improving thermal emissivity can be an effective method to enhance its overall heat removal capacity. For heat sinks made of aluminum, several ways can fulfill this purpose including spray painting, powder coating, abrasive blasting, and ceramic coating. But the most cost-effective and well-adopted technique is aluminum anodizing. In addition to the potential thermal improvement can be gained by alternating

the surface condition, aesthetic appearance needs to be taken into account as well. Section 1.4 shows the review of pertinent literature of aluminum anodization and thermal radiation.

1.2.2. IC650 battery charger thermal design

The thermal design of IC650 battery chargers, Delta-Q Technologies, is an example to illustrate the idea of the passive cooling system. The IC650 is designed for charging lithium-ion and lead-acid batteries in small electric vehicles. The maximum output power is 650W, and the output voltage can range from 24V to 48V. The heat generated by various types of internal electronics is transferred out from devices to the heat sink via an identical thermal path. The heat sink is entirely passive cooled by the fins that integrated directly on the chassis. Several thermal resistances are along the thermal path from heat source to heat sink which are the bulk resistance of thermal interface material (TIM) that provide electrical insulation, thermal contact resistance (TCR) because of the imperfect solid-solid contact, spreading and bulk resistance of the heat sink and finally, the resistance for natural convection (film resistance), and thermal radiation before waste heat dissipates to the ambient.

During the standard operation, surface temperature should not exceed the touch-safe restriction, which is 85℃. It is challenging to maintain the temperature under this threshold and push maximum output power at the same time when the ambient temperature is above 40℃. Therefore, they show a great interest in pursuing passive cooling solutions for their power electronic products and try to extend the heat transfer limits up to the edge.

1.3. Research motivations

Thermal management is always a fast grew market since the crucial role that it plays in the electronic and power electronics industry. The global market for thermal management technologies will hit $16.3 billion USD at the end of 2023 with the growth rate of 5.6% since the year 2018, and 79% of the overall thermal management market is comprised of cooling hardware, i.e., heatsinks, fans, which reflects the importance of efficient cooling technologies [13]. This work has been motivated by a collaborative research project with our industry partner, Delta-Q Technologies, a battery charger design

and manufacture company for small electric vehicles located in Burnaby, BC. To maintain nominal operation and desired efficiency, their products rely on capable yet reliable cooling systems. Most of their products will operate on-board the moving vehicles where the vibration environment will pose a certain risk of failure to the moving mechanical parts and may cause loose wire connections. Some of them may even experience the on-field operation where the outdoor environment will cause severe mechanical failures due to corrosions and potential collisions. The exposure to the harsh environment may also lead to severe failures in moving parts. Therefore, the passive cooling systems are the best solution to confront the extreme environment, and replacement of the current fan-assisted heat sinks is urgent. The improvement of such passively cooled systems which can tackle with high power electronics and remain the surface temperature under the touch-safe allowable limitation is of great interest to their future line of products and is essential to expand the current passive cooling device with high output power. Figure 1.3 shows the current product line of IC series battery charger from Delta-Q Technologies.

Figure 1.3 IC Series battery charger, Delta-Q Technologies

1.4. Literature review

This section provides a general review of three related subjects including: i) thermal radiation from a finned heat sink; ii) thermal emissivity of the anodized aluminum; iii) natural convection from a finned heat sink. As a starting point, the importance of thermal radiation is first explored by comparing the impact of thermal emissivity in various finned heat sinks on the contribution of radiative heat transfer to the overall heat dissipation. The aluminum anodization technologies are also introduced with a summary of the pertinent studies that partially emphasis on the potential revision to the anodizing procedures and the implication on the thermal emissive behaviors. Finally, natural convection in different

heat sinks with various fin geometries is investigated and thoroughly examined to offer an overview of different naturally cooled heat sinks (NCHx) in terms of current availability in the literature.

1.4.1. Thermal radiation from finned heat sinks

The fundamental governing equation for describing the thermal radiation is the Stefan-Boltzmann equation. The generic formation for the radiative heat transfer between heat sink surfaces to the ambient is:

$$Q_r = \sigma\varepsilon\left(T_w^4 - T_{amb}^4\right)\sum_{i=1}^{n} A_i F_{i\rightarrow amb} \tag{1.2}$$

where σ is the Stefan-Boltzmann constant $[5.67 \times 10^{-8}\ \mathrm{W{\cdot}m^{-2}{\cdot}K^{-4}}]$, ε is surface thermal emissivity, A is the surface area, and F is the view factor from the surface to the ambient, respectively. It expresses that the amount of radiative heat transfer is proportional to the temperature difference between two surfaces in a manner of their fourth power. The form of the underlying governing equation for radiation heat transfer is straightforward but it is challenging to solely subtract the thermal radiation from overall heat transfer since the amount of radiative heat transfer is highly coupled with natural convection by surface temperature in a nonlinear fashion. Secondly, the calculation of view factor from heat sink surfaces to the participating heat transfer area is not an easy feat given the complexity of the fin geometry. It is challenging to come up with a full analytical solution to this problem. However, Eq.1.2 clearly shows the radiative heat transfer is linearly associated with surface thermal emissivity.

Most studies available in the literature are conducted by either experimental or numerical approaches. The work done by Edwards and Chaddock [14] is among the earliest to report the significance of thermal radiation where they claim one-third of overall heat transfer in an extended cylindrical surface is contributed by radiation as surface thermal emissivity close to 0.99. Following studies further confirm the critical role of thermal radiation in naturally cooled heat sinks regardless of their fin types. Table 1.2 lists some of the pertinent literature that supports the considerable portion of heat dissipated by radiation.

Table 1.2 Literature review on the thermal radiation from finned heat sinks

Ref.	Approaches	Fin Geometry	Surface Emissivity	*Qr/Q*(%)
Chaddock et al. [14]	Experimental	Cylindrical	0.99	33
			polished	10 - 20
Sparrow et al. [15]	Experimental Analytical	Cylindrical	0.82	25 - 45
Rao et al. [16]	Experimental Numerical	Rectangular	0.05 – 0.85	25 - 40
Rao et al. [17]	Numerical	Rectangular	0.05 – 0.85	36 - 50
Yu et al. [18]	Experimental Analytical	Rectangular	0.8	27
Tamayol et al. [19]	Experimental Analytical	Rectangular	0.75	50
Guglielmini et al. [20]	Experimental	Staggered	0.05 – 0.85	25 - 40
Aihara et al. [21]	Experimental	Pin	0.9	19 - 48

1.4.2. Anodization of aluminum and its alloys

Anodization, as the most commonly used and cost-effective surface treatment technologies for aluminum and its alloys, is well adopted throughout the industry. It is an electrochemical process that will spur the growth of the original oxidation layer on the aluminum surface and convert into a thin anodic aluminum oxide (AAO) films. In general, the types (barrier-type and porous-type) of AAO film depends on the nature of electrolyte during the anodizing process. In particular, the porous-type has received considered attention and has extensive application in practice. Attributed to its porous structure, the AAO films become a perfect base or substrate for electroplating, painting, and semi-permanent decorative coloration [22]. Moreover, many superior engineering properties such as excellent hardness, abrasion, and corrosion resistance also can be found in porous-type AAO films yielded by the acidic anodization [23]. The mechanical strength of AAO layers is always of great interests for various applications [24][25][26] in the industries.

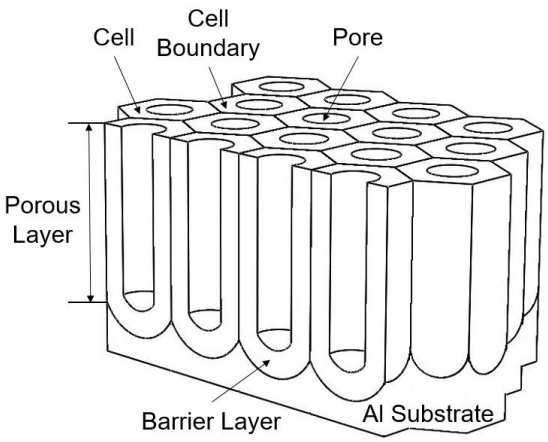

Figure 1.4 Schematic of Porous Anodic Aluminum Oxide (AAO) layers

The US Military specification [MIL-A-8625F] [27], categorizes the anodic coating for aluminum and its alloy into three types and two classes. Type I [Chromic acid anodizing] can generate an ultra-thin film ($\leq 17\mu m$) but with optimal properties for dyes adhesion and resisting corrosion. However, it only can be applied to the cases where high precision is required such as aerospace and military industries due to the fact that acidic residue will pose less risk to cause metal fatigue compared with sulfuric acid, despite that the adverse environmental impact of the by-products during the process. Nevertheless, Type II [Sulfuric acid anodizing] and Type III [Hard anodic coating] are more desired in conventional engineering applications. The Type II anodizing features a thinner film ($t \leq 25\mu m$) to better serve for the cosmetic purposes while the Type III [hard coat] anodizing, as its name suggested, often implements in the cases where it demands higher wear and corrosion resistance with the assist of the relative thicker AAO layer ($t \leq 115\mu m$).

The extraordinary thermal radiative properties of AAO layer is also noticed by the previous studies. Especially during the space age, the thermal control of the spacecraft is crucial, and radiation is the only fundamental heat transfer mechanism that can be used to dissipate the waste heat to the ambient in a vacuum environment, i.e., the cooling fluid does not exist. National Aeronautical Space Administration (NASA) performed a series of investigations of the thermal radiative properties of anodized aluminum as thermal control coatings in spacecraft design [28][29][30]. They found that the thermal radiative properties of anodized aluminum are promising, i.e., low solar absorptance and high thermal emittance., but it highly depends on the electrolytes and AAO film thickness. In addition, the degradation of anodized aluminum in the long duration orbital exposure experiment

was observable [31] [32]. Furthermore, subsequent studies focused on a variety of aluminum alloys and any potential adjusts to anodizing procedures that may have a profound influence on thermal emissivity. Kumar et al. [33] came up a novel approach to a white anodic oxide coating with special additive to the sulfuric acid bath and improved surface emittance up to 0.8 with lowest solar absorptance 0.15 on aluminum alloy 2024. Lee et al. [34] compared the effect of different acidic electrolytes and sealing methods on thermal emissivity where they found out that the oxalic acid with black sealing can result in the most substantial enchantment of thermal emissivity up to 0.91 in aluminum alloy 1050.

As such, there is a gap between the thermal radiation from heat sinks and thermal emissivity of the anodized surface in the existing literature. Most of the studies mentioned above solely emphasis on one aspect of the subject, either performance of heat sinks or anodization, and conjugated studies of both subjects are needed in order to provide a consistent and comprehensive understanding of the potential effect of anodization on the thermal radiation in finned heat sinks.

1.4.3. Natural convection from finned heat sinks

Natural convective heat transfer from various finned heat sinks has been explored extensively over the year, and the existing correlations of various fin shapes are well established by analytical, numerical and experimental approaches which have been further validated by many efforts. This section provides an overview of pertinent literature of different fin geometries, i.e., straight fins, inclined fins, interrupted fins, and pin fins, in the scheme of natural convection with various orientations.

The Newton law of cooling can be used to describe the total convective heat leaving the heat sink surfaces which is:

$$Q_c = hA\Delta T \tag{1.3}$$

Where h is the heat transfer coefficient, A is the surface area of the heat sink, and ΔT is the temperature difference between the heat sink surfaces to the ambient. In natural convection, the heat transfer coefficient is not only associated with fin geometry but also with the heat sink orientation given the fact that the driving force of the flow is assisted by

the gravity. It is also noticeable that both h and A are a function of fin dimensions including the spacing, height, length, and the diameter of the fins.

For natural convection problems, several dimensionless parameters (*Nu*, *Ra*, *Pr*) are crucial to describe the heat transfer and flow behavior. Nusselt number (*Nu*) measures the ratio of convection to conduction in the near-wall boundary layer. Rayleigh number (*Ra*) is associated with the buoyancy force and describe the state (laminar or turbulent) of the flow. Prandtl number (*Pr*) is defined as the ratio between the momentum diffusivity and thermal diffusivity, indicates the diffusion property of the fluid. Detailed information regarding these dimensionless parameters can be found in [12].

Straight fins: Natural convection from continuous straight finned heat sinks is a well-studied subject in the literature. Bar-Cohen and Rohsenow [35] performed a semi-analytical study of the optimum fin spacing for isothermal vertical placed parallel plates and developed a relationship between the average Nusselt number and Rayleigh number as:

$$Nu_s = \left[\frac{576}{\left(\frac{Ra_s S}{L}\right)^2} + \frac{2.873}{\left(\frac{Ra_s S}{L}\right)^{0.5}} \right]^{0.5} \tag{1.4}$$

This correlation has been widely used in future studies and designing of naturally cooled heat sinks (NCHx). Van de Pol and Tierney [36] presented an iterative mathematical model to analyze the free convection and radiation heat transfer from vertical straight fin arrays. Aihara [37][38][39], as well as Welling and Wooldridge [40], conducted a series of experimental studies of the vertical rectangular-fin arrays. Elenbaas [40], Churchill [41], Bodoia and Osterle [42], and Sparrow and Acharya [43] are also some of the examples with detailed analysis. The horizontal placed straight finned arrays also bring interests to many studies. Harahap and McManus [44] proposed a relation to calculate the average heat transfer coefficient for the horizontal placed straight finned heat sink. Jones and Smith [45] investigated the optimum fin spacing for horizontal placed rectangular fin surface by testing several heat sinks experimentally. Harahap and Setio [46] experimentally investigated the heat transfer from a horizontal plate-fin heat sink and correlated two types of empirical correlations. In terms of orientation effect on natural convective heat transfer, Starner and McManus [47] performed a study of the finned heat

sink with three different orientations, vertical, horizontal, and 45° inclined. They found that the heat transfer coefficient is 10% to 30% below those of similar vertical fin arrays. Leung and Probert [48] placed their interests in the effect of orientations on the thermal performance and found out the vertical placed rectangular finned heat sink always yield the best results. Shen et al. [49] examined the heat transfer from rectangular fin heat sink with up to eight inclined angles experimentally and numerically, and the thermal performance for 45°, 135°, 225°, and 315° are almost the same. Tari and Mehrtash [50] also investigated the effect of inclination in a naturally cooled rectangular finned heat sink and they suggested a set of correlations whose errors remain within the ±20%. It can possibly be used for application where the inclined heat sink is of great interest.

Inclined fins: Aside from the traditional continuous finned heat sink, the inclined fins take the idea of cutting long fins into small sections and rotate with a certain inclined angle. By doing so, the inclined fins have more surface area for heat transfer compared to the conventional continuing fins. It also can divert the air-flow to the inclined directions. As such, the inclined fins perform more equally at all orientations except pointing downwards. The heat sink of the IC series battery charger [Delta-Q Technologies] adopts the similar design, and the schematic of the inclined fins is showing in Figure 1.5.

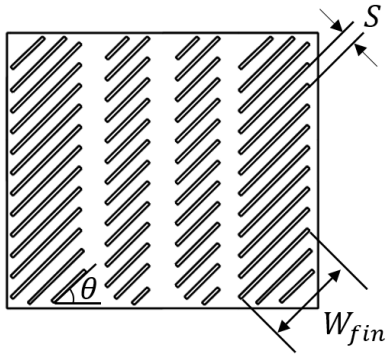

Figure 1.5 Schematic of inclined fins, IC650 heat sink design, Delta-Q Technologies

Natural convection from an inclined plate has been explored by several previous studies and not always been the main focus in the literature because the fin inclination is expected to reduce the buoyancy force along the vertical direction. However, the combined heat transfer performance from the inclined surface is increasing due to the discontinuity of the thermal boundary layer where it somehow resembles the flow pattern from a horizontal heated plate [51]. Some of the previous researches try to find the analytic solution for this types of natural convective heat transfer problem, such as Rich [52] who

suggested the natural convective heat transfer coefficient can be determined from the vertical plate by replacing the gravity factor to $gcos\theta$ in calculating the Rayleigh number. The results indicated the heat transfer is within 10% of the values from the vertical plate in the range of inclined angle between 0° to 40°. Kierkus [53] solved the boundary layer equations using a perturbation method for the incline angle up to 45°. Lee and Lock [54] numerically solved the laminar free convective problem along the isothermal inclined surface. Furthermore, Vilet [55], Fujii and Imura [56], Shaukatullah and Gebhart [57], Pera and Gebhart [58], Lloyd and Sparrow [59], Al-Arabi and Sakr [60], and Wei et al. [61] represent some of the efforts that focus on the inclined plates by either experimental and numerical approaches.

Ozoe et al. [62] [63] are one of the pioneering studies on the topic of natural convection from an inclined channel. They conducted a series of experimental and numerical studies and concluded the maximum rate of heat transfer occurs when the inclined angle is of around 50°. Azevedo and Sparrow [64] investigated an open-ended inclined channel experimentally and flow visualization results revealed the longitudinal vortices along the inclined channel do help improve the thermal performance when heated from below. Varol et al. [65] focused on the case when a corner heater existed in an inclined enclosure, and they found the maximum heat transfer happens when the heat sink is inclined at 135° and obtained the minimum heat dissipation rate when inclined at 60° through a sequence of studies. Some examples of natural convection from a single inclined channel can be found in [66]–[71].

However, there is not enough literature to support the natural convection from a heat sink made of inclined fins. Fujii [72] is one of the pioneering work, and he performed a sequence of experimental studies at vertical orientations. He concluded that 19% improvement could be gained from inclined fins with compare to the 90° straight fins when the fin inclination angle is of 60°. The correlated relationship from his experimental studies are:

$$Gr_s = \frac{g\beta S^3(T_w - T_a)}{\upsilon^2} \cdot \cos\left(\frac{\pi}{2} - \theta\right) \tag{1.5}$$

$$Nu_s = \frac{1}{24}(Gr_s Pr)\left(\frac{S}{W_{fin}}\right)\left[1 - e^{\frac{-12.5}{\left(\frac{Gr_s PrS}{W_{fin}}\right)^{\frac{3}{4}}}}\right] \tag{1.6}$$

Interrupted fins: Effect of fin interruptions in naturally cooled heat sinks (NCHx) is a well-established topic in the literature. The idea embedded with interrupted fins is forcing to reset and rebuild the entrance region of the thermal boundary layer where the maximum heat transfer happens. Da Silva et al. [73] arranged the heat source discretely to find the best distribution in the case of natural convection. Sobel et al. [74] compared the performance between the staggered fins and continuous fins experimentally, and interruption of fins leads to a significant improvement. Sparrow and Prakash [75] carried out a numerical study of a staggering array of discrete vertical plates where it can improve the overall thermal performance by a factor of two. Rao and Sastri [76] numerically obtained the solution for the staggered vertical channel, and they observed a three times thermal improvement compared to the parallel plate array. Daloglu and Ayhan [77] investigated a finned rectangular cross-sectional vertical channel and compared the experimental results with a smooth channel. Gorobets [78] developed a mathematical model and numerically calculated for a vertical surface with discrete fins arrangement, and his comparison shows the heat transfer was intensified by 50% - 70%. A continuous effort has carried out in the LAEC for the natural convection from interrupted finned heat sink by experimental, numerical and analytical methods including Golnoosh et al. [9][79] and Ahmadi et al. [80][81][82]. The results showed that the average heat transfer improvement in their designed heat sink was 500% better than commercially available heat sinks. In addition, Ahamdi [81] developed a novel analytical model using the integral technique, and a thorough parametric study of the interrupted fins was conducted.

Pin fins: The alternation of the rectangular fin into either a circular or square rod can also be an effective way to reduce the thermal resistance for natural convective heat transfer. However, the problem appears to be the trade-off between the pin spacing and the surface area, and both are greatly influenced by the pin diameter. The proper design of the pin fin can make it suitable for natural convection. Because of the geometrical complexity of the pin fin heat sink, the full analytical solution to the natural convection problem is rare, and most of the studies are done by either experimental or numerical methods. The reported empirical solutions are limited within certain range of the fin diameter and the phase of flow regime, i.e., laminar, transition, or turbulence. The alignment of the pins can be categorized into two types, staggered and in-line showed in Figure 1.6 as below:

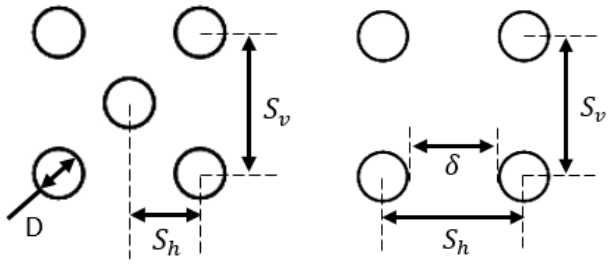

(a) (b)

Figure 1.6 Pin fin alignment: (a) Staggered; (b) In-line

Aihara et al. [83] carried out an experimental study on free convective and radiative heat transfer from staggering pin fins with vertical base and correlated empirical relations from the observed results. Zografos and Sunderland [84] found out that the in-line arrangement of the pins can yield up to 20% better thermal performance compared to the staggered pin arrangement under the regime of natural convection. They also discussed the effect of heat sink inclination (90° - 60°) on the thermal performance in which no significant difference has been observed. Lyengar and Bar-Cohen [85] performed an optimization study using least-material method for staggered aligned pin fins at a vertical orientation and concluded that the pin fin is more volumetrically efficient than other fin geometries, plate fins or triangular fins. Joo and Kim [86] proposed an analytical solution using the asymptotic method for staggered arranged pin fin arrays and considered four limiting cases. Their optimization studies show the optimized pin fins are performed better per unit mass compared to the plate fins at vertical orientation. Fisher and Torrance [87] came up with a semi-analytic solution to the vertical placed in-line pin fin arrays for optimization purposes, the optimal pin porosity decreasing with increasing of pin diameter and Rayleigh number. Sahray et al. [88] used both numerical and experimental approach to optimize the in-line square pin fin arrays in horizontal orientation, and an optimal pin density existed with pin spacing to width ratio approximately equals to 3.

In summary to this section, natural convection from finned heatsink is investigated thoroughly in terms of each fin geometry. However, the effect of orientation on heat sink performance and comparison between each fin geometry is less sufficiently in the existing literature. It is hard to determine which fin geometry are the best in the practical design with the same volume/base area footprint. In addition to this problem, there are fewer researches devoted to the inclined finned heat sink which can be an interesting topic as an alternative heat sink fin design to the application in power electronics.

1.5. Research objectives and chapter contents

In this thesis, the goal is to improve the overall heat rejection capability in IC650 battery charger, a commercially available product from Delta-Q Technologies, our industry partner of this project. The overall thermal resistance including the resistance for thermal radiation and natural convection is reduced by means of increasing the emissivity of the heat sink surface and alternating the heat sink fin geometry. In detail, chapter 2 records a comprehensive study of the thermal impact of anodization on the finned heat sinks and also the role of thermal radiation in passively cooled devices. Comparison of various heat sink fin geometries for natural convection in multiple orientations is explored in chapter 3 by prototyping and experimenting of four heat sinks that bear the same heat sink footprint, i.e., inclined fins (benchmark case) resembling the IC650 arrangement, inclined interrupted fins, straight interrupted fins, and pin fins. Chapter 4 further examines the thermal performance of inclined interrupted fins and a parametrical study on the various heat sink fin geometrical parameters is performed with developed validated numerical model.

Chapter 2.

Thermal impact of anodization and radiation

In this chapter, the main goal is to understand the effect of anodization on the thermal emissivity of the aluminum alloys and also the potential thermal improvement of the anodized IC650 heat sinks that resulted from the emissivity enhancement. The thermal emissivity of anodized samples is measured with Fourier Transform Infrared Reflectometer (FTIR). An experimental-numerical approach is adopted to investigate the enhancement of the thermal radiation of the anodized heat sinks. Results show that anodization could lead to a significant reduction in overall thermal resistance (15% maximally) in terms of both natural convection and thermal radiation. The radiative heat transfer can contribute up to approximately 41% of the overall heat dissipation.

As mentioned in the earlier section, Delta-Q Technologies uses aluminum die-cast technologies extensively to manufacture the heat sink of high power battery chargers attributed to the superior advantages that can create complex shapes with high precision yet low cost in mass production. Die-cast technologies require aluminum alloys with good castability where the aluminum-silicon alloys are by far the most widely used, particularly in automotive applications [89]. Aluminum alloy A380 is one of the most commonly specified aluminum-silicon alloys in the die-cast process which has been widely used in manufacturing the heat sink of the IC650 battery charger. Despite its widespread application in various industries, no in-depth study of the impact of anodization on A380 alloys can be found in terms of thermal emissivity as well as its surface morphology. In addition, the thermal impact of anodization on the machined Al alloy 6061 surfaces is also investigated.

2.1. Sample preparation

The sample preparation of aluminum substrates for anodization can be divided into two categories based on the types of the aluminum alloys, i) die-cast aluminum (A380) samples and ii) the machined 6061 T6 aluminum alloys samples. Because of the unique metallurgical process of die-cast technologies, it is impractical and of the high cost to customize the casting in a small volume. Thus, the prepared die-cast aluminum plates

[2.5cm×5.0cm] for emissivity measurement are the flat fins chopped off the IC650 heat sinks that provided by the Delta-Q Technologies. As for the machined 6061 sample plates [5.0cm×7.5cm], they are made from the 6061 T6 alloy plates bought in a local BC vendor [Metal Supermarket] and hand-machined in the School of Mechatronic Systems Engineering Machining Shop. Several unprocessed heat sinks were also prepared and cleaned in advance for anodizing and testing. The length [$L_{heatsink}$], width [$W_{heatsink}$], and height [$H_{heatsink}$] of the heat sink are 23cm, 17cm, and 7.5cm, respectively.

The anodization of all the samples was performed in a local BC surface finishing treatment company [Spectral finishing Inc.]. The anodizing process follows a procedure of cleaning, etching, acid desmutting, anodizing, coloring(optional) and sealing [90]. The intention of the first three steps is to remove any contamination on the surface during the manufacturing process and to etch away the original thin oxide layer which leaves the perfect aluminum substrate for anodizing. The coloring let the newly formed porous AAO layer to absorb color pigments sufficiently to reach the desired surface appearance. The last step, sealing, is a process of precipitating an additional layer of sealant, on top of the uncovered anodized surface to protect the pore structure and the dyes to extend durability and avoid absorbing impurities.

The anodizing was occurring in a 15% sulfuric acid bath with proprietary additives. The temperature control is crucial to control the growth of the AAO layers to the proper thickness and has a profound influence on surface morphology. For Type II anodizing, the temperature of electrolyte bath is approximately in the range of 20℃ to 30℃ while the Type III treatment needs lower electrolyte temperature [14℃] to minimize the resistance to reach the heavier thickness. Due to the dialectic property of the AAO layer, the control of current density applied to the parts need to be increased from their starting point [16 $mA \cdot cm^{-2}$] with regard to the development of the anodic layer as the anodizing process proceeds. In some alloys with greater than 5% copper or 8% silicon, such as aluminum A380 [7.5% to 9.5% silicon], Type III [hard coat] cannot be achieved [27]. In this case, the thickness of the AAO layer that formed on A380 alloys is confined to 25μm for either Type II or Type III anodization. As for the coloring, the metallic-based dyes are used in order to avoid degradation by the long term sunlight exposure, mainly UV light, compared with organic pigments. It also needs to note that the AAO thickness of dyed samples is relatively thicker to provide enough adhesion force compared with the clear samples in Type II treatment. Finally, the immersion of the anodized parts into cold nickel fluoride

solution was served as the last step to seal the uncovered AAO layer. Figure 2.1 shows the surface comparison before and after the anodization treatment. The surface darkness of dyed and clear samples is not significantly varied regarding different types, and the anodic layer itself reveals this dull and grey color.

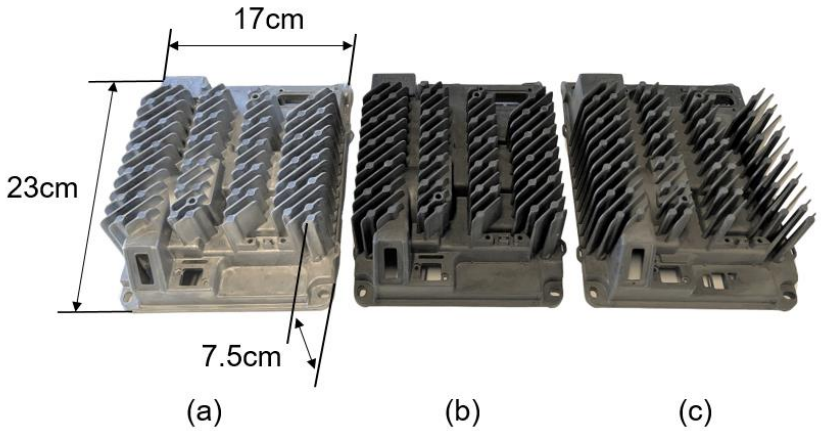

Figure 2.1 IC650 heat sinks before and after various anodizing treatment, (a) Bare; (b) Type II-Black; (c) Type III-Clear

Both Type II and Type III anodized samples were prepared with various thickness of the anodic layer and surface color [clear or black]. In each group, at least two samples were anodized in the same condition to ensure the repeatability of the measured results. Among the full treated samples, the unsealed plates were also prepared with interested to investigate the effect of sealing layer on the thermal emissivity, as well as allow us to observe the pore distribution of selected samples. The exact amount of samples prepared is listed in Table 2.1. It should also be noted that the mentioned thickness of the AAO layer is just used as a reference to differentiate the anodizing time in this context. Further efforts are required to perform investigation with precision to determine the accurate thickness of the anodic layer.

Table 2.1 Amount of samples prepared with various types of anodization

Amount of samples			Plates (A380)	Plates (Machined 6061)	Heat sinks (A380)
Untreated			2	2	2
Type II Sealed	Clear	15μm	-	2	-
		20μm	2	-	-
	Black	20μm	-	2	-
		25μm	4	-	2

Type III Clear	Sealed	25µm	4	-	2
		66µm	-	2	-
	Unsealed	25µm	2	2	-
		66µm	-	2	-

2.2. Emissivity measurement

2.2.1. Background

In general, all the objects not only constantly emit electromagnetic radiation as a result of the changes in the electronic configuration of the atoms and molecules induced by the random thermal motion [12] but also always receive the radiation from surroundings. This electromagnetic energy can be either reflected on the surface, transmitted through the body or absorbed. The reflected, transmitted, and absorbed energy should account for 100% of the total incident energy, as an indication of:

$$\gamma + \tau + \alpha = 1 \tag{2.1}$$

Where γ is reflectivity, τ is transmissivity, and α is absorptivity of the objects. However, no real body in practice exhibits perfect reflection, transmission, or absorption capability. The amount of radiative energy that can be reflected, transmitted, and absorbed is determined by material physical properties and varies from metals, woods, to bricks. For instance, polished metal surfaces such as gold, the reflectivity in the range of infrared spectrum can be as high as 0.98. Opaque bodies simply have the transitivity of zero under visible light spectrum where no visible light can penetrate through the body. Nevertheless, if a body shows the capability to absorb all incident radiation where we usually define it as an ideal blackbody. Not only the blackbody owns the ability to absorb all the incoming energy, but it will also emit the same amount of energy to maintain the thermal equilibrium. This can be extended to any arbitrary body when absorbing and emitting the same radiation within the same spectrum at the same time. In order to reach the thermodynamic equilibrium, the emissivity of an object is always equal to the absorptivity which is known as Kirchhoff's Law of Radiation:

$$\varepsilon = \alpha \tag{2.2}$$

According to Eq.2.1, the emissivity of a body in thermal equilibrium can be reformulated in terms of reflectivity and transmissivity:

$$\varepsilon = 1 - (\gamma + t) \tag{2.3}$$

Emissivity is a measure of how closely a surface approximates a black body, which has the emissivity of one, and it also varies depending on the surface temperature, wavelength, and directions. However, it should be noted that Kirchhoff's law of radiation does not hold when a considerable difference exists between the surface temperature and temperature of the source of irradiation.

Furthermore, the radiative behavior of the blackbody is also important and lays the foundation to better understand the emission of a real subject. The spectral emissive power of a blackbody can be determined by the Planck's Law as:

$$E_{b\lambda}(\lambda, T) = \frac{C_1}{\lambda^5[\exp(C_2/\lambda T) - 1]} \tag{2.4}$$

Where the C_1 and C_2 are the radiation constant which is 3.74177 × 10^8 W·μm^4·m^{-2} and 1.43878 × 10^4 μm·K. It is clearly to show that the emissive power of a blackbody is a function of the surface temperature and wavelength where it also increases with temperature. The Wien's displacement law expresses the spectral distribution of a blackbody with the corresponding wavelength to temperature as:

$$\lambda_{max} \cdot T = C_3 \tag{2.5}$$

Where the λ_{max} is the peak wavelength in the spectral distribution and C_3 represents the third radiation constant, 2898μm·K. The Wien's displacement law tells that the maximum spectral emissive power shifts to the shorter wavelength when the surface temperature of blackbody increases and almost entire emitted radiation fall into the range of infrared when the surface temperature below 800K [12]. In this research, we only focus on mid-wavelength infrared [MWIR] (3μm to 8μm) and long-wavelength infrared [LWIR] (8μm to 15μm).

In general, as above mentioned, the emissivity of a real surface depends on the surface temperature as well as the wavelength and directions of emitted radiation. There are different types of reported emissivity value, mainly divide into two categories

depending on whether it has been averaged with regard to all wavelengths or directions, i.e., spectral or total, directional or hemispherical. The most fundamental value that can be directly measured is the spectral directional (usually in the normal direction) reflectance, the corresponding emissivity are calculated based on Eq.2.3. However, the total hemispherical emissivity is widely accepted and reported in most textbooks where it specifies the emissivity averaged to all wavelengths and directions.

2.2.2. Equipment

The thermal emissivity of each anodized surface was measured using 400T Infrared Reflectometer from Surface Optics Corporation (SOC) available in Solar Thermal Research Laboratory (STRL) at the University of Waterloo. This is a Fourier Transform Infrared Reflectometer (FTIR) that designs for determining the spectral emittance of the samples in the range of wavelength from 2μm to 25μm. All measurements were performed under the room temperature. Ideally, it would be preferable to keep the sample measured at an elevated temperature so as to be consistent with the actual working environment but conditioning the equipment has some challenges. The spectrometer measures the reflectance repeatability of ±1%. The spectral measurement was performed in accordance with method C of ASTM E408-13 [91]. Detailed descriptions and comparison of SOC-400T can be found in [92].

A 1650K silicon carbide glow bar was used to provide a grey body source of light over the full spectral range. The modulation and collimation of the IR beam were done by a Michelson Fourier Transform Infrared Interferometer [MIDAC corporation]. A system of dual Compound Parabolic Concentrators (CPCs) gathered the reflected lights from the sample surface before entering the sensor, which is a 10mm pyroelectric deuterated triglycine sulfate (DTGS) mid-infrared detector.

Figure 2.2 The SOC 400T Spectral Reflectometer

The spectrometer was first calibrated by scanning the background room and recorded it as zero spectrum. The reference spectrum was recording by measuring the reference surface made of polished gold with constant spectral reflectivity of 0.98 in the measured infrared range. The sample reflectance is measured and corrected by zero and reference spectrum, as:

$$\gamma_{sample} = \frac{\gamma_{measured} - \gamma_{zero}}{\gamma_{reference} - \gamma_{zero}} \tag{2.6}$$

SOC 400T measures the directional-hemispherical reflectance directly, and the IR beam is coming at samples from a near-normal direction (20° off normal) while the reflected signal is measured hemispherically. The detected reflectance can be reduced to hemispherical-hemispherical reflectance by a factor of pi. Thus, the spectral hemispherical emissivity can be easily calculated by being substrate by one as:

$$\varepsilon_\lambda(\lambda, T) = \frac{E_\lambda(\lambda, T)}{E_{\lambda b}(\lambda, T)} = 1 - \frac{1}{\pi}\,\gamma_\lambda(\omega, \phi, T) \tag{2.7}$$

Where the *E* is emissive power and the subscript λ, b denote that the value is spectral and from the blackbody. The ω and ϕ characterize the zenith angle and the azimuthal angle of the incident light. The total hemispherical emissivity is simply the quotient between the integration of spectral emissive power and of that from the blackbody at the same temperature and can be formulated as:

$$\varepsilon(\lambda, T) = \frac{E(\lambda, T)}{E_b(\lambda, T)} = \frac{\int_{\lambda=0}^{\lambda=\infty} \varepsilon_\lambda(\lambda, T) E_{\lambda b}(\lambda, T) d\lambda}{\sigma T^4} \tag{2.8}$$

Because the spectrometer has the measured wavelength range from 2μm to 25μm, so the formulation for calculating the total hemispherical emissivity becomes:

$$\varepsilon(\lambda, T) = \frac{E(\lambda, T)}{E_b(\lambda, T)} = \frac{\int_{\lambda=2}^{\lambda=25} \varepsilon_\lambda(\lambda, T) E_{\lambda b}(\lambda, T) d\lambda}{\int_{\lambda=2}^{\lambda=25} E_{\lambda b}(\lambda, T) d\lambda} \tag{2.9}$$

2.2.3. Results

Figure 2.3 shows the comparison of total hemispherical emissivity between the die-cast A380 Al alloys and the machined 6061 Al alloys. The error bars represent the

repeatability of the measurement [1%] and standard deviation between the samples. Surprisingly, the surface of die-cast aluminum has the emissivity of 0.14 compared to the machined aluminum which is 0.03. This is consistent with the typical range of emissivity for metals that are from 0.1 to 0.4 for unpolished and 0 to 0.2 for polished [12]. It may indirectly indicate the potential thermal improvement can be seen on the bare die-cast made aluminum heat sinks compared with machined ones. Given the fact the die-cast procedures require the molten metal been injected directly into the mold with high pressure, the oxidation process may have been expedited and intensified which may result in thicker oxide layer leading to the relative high emissivity in die-cast samples. As for the machined 6061 Al alloy surface, the machining certainly increases the overall surface roughness but not able to compensate for the thinner oxide layer as a result of machining. In all, the measured emissivity of the machined aluminum surface has an indication of less thermal radiation contributed to the overall heat transfer. The spectral distribution of surface emittance can be found in Appendix A.

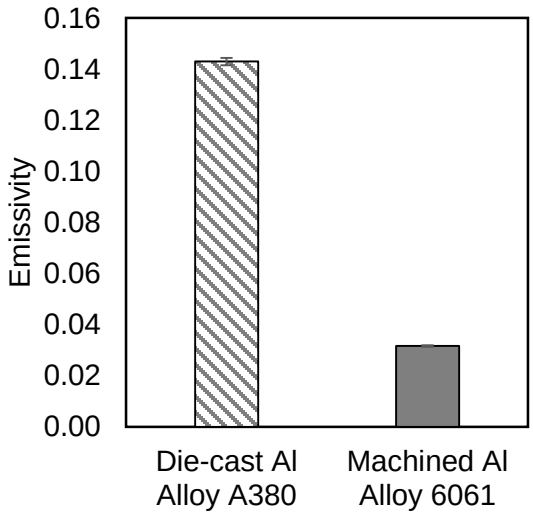

Figure 2.3 Total hemispherical emissivity of the metal surface, die-cast, and machined aluminum

The total hemispherical emissivity values for a range of anodized die-cast aluminum show in Figure 2.4. The Type II-Black treatment has the highest thermal emissivity of 0.92 while the Type II-Clear, Type III-Clear and Type III-Clear unsealed are able to increase the thermal emittance from bare die-cast aluminum surfaces to 0.86, 0.92, 0.91 respectively. Compared with the untreated surfaces, aluminum anodization could significantly improve the surface radiative emissive properties, up to seven times,

regardless of treatment types. The comparison between the dyed and undyed samples, i.e., Type II-Black and Type II-Clear, shows over 5% enhancement in thermal emissivity. This is a combined effect from the use of pigments as well as the thickness of the AAO layer where both of them may contribute to the emissivity improvement. Despite the difference of the anodizing process, the anodized surfaces by Type III-Clear treatment have almost the same thermal emittance as Type II-Black. In addition, the results also show the influence of sealing on the thermal emissivity as well. The cold nickel fluoride sealing method used by the surface finishing vendor does help the thermal emissivity of the AAO layer resulted from Type III treatment slightly increase from 0.91 to 0.92. However, it falls into the measurement error range where further efforts are required. Previous studies of various sealing methods on the thermal emissivity [34] concluded that this may be attributed to the nature of the precipitated sealants.

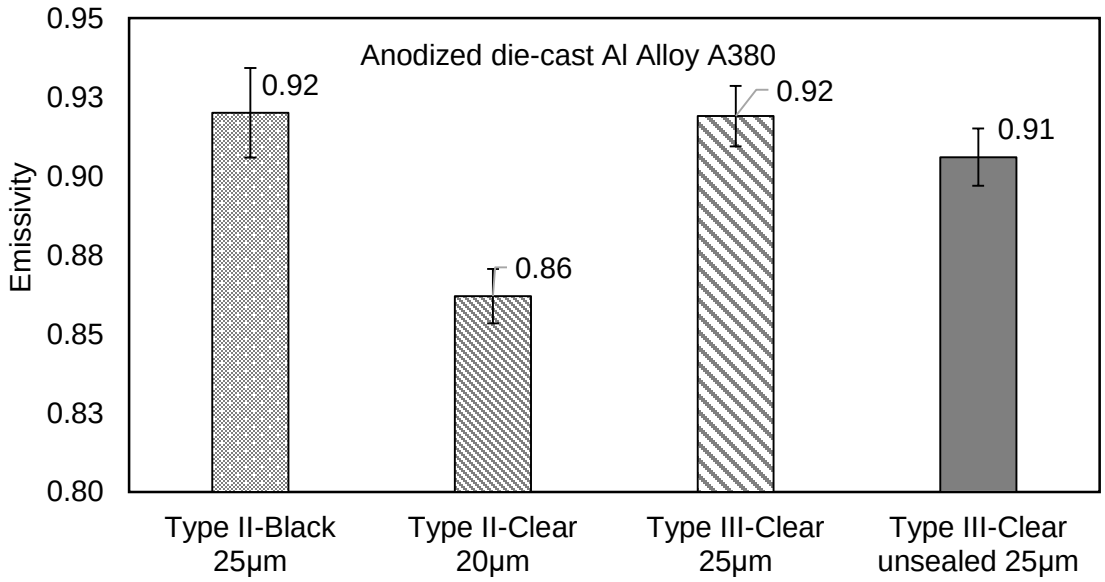

Figure 2.4 Total hemispherical emissivity for various anodized die-cast Al alloy A380 sample surfaces

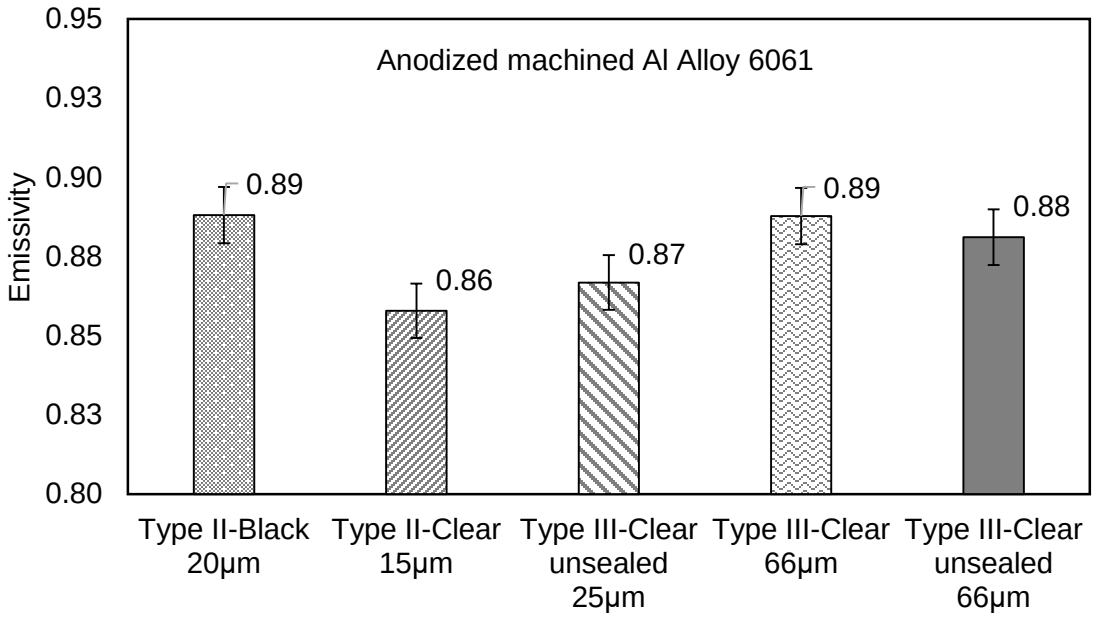

Figure 2.5 Total hemispherical emissivity for various anodized machined Al alloy 6061 sample surfaces

The results for the anodized machined Al alloy 6061 sample surfaces are presented in Figure 2.5. The same improvement of total hemispherical emissivity can be achieved but slightly decreased with respect to the anodized die-cast samples. Type II-Black and Clear anodized surfaces have the thermal emissivity of 0.89 and 0.85. It shows the same trend as anodized die-cast samples where the dyed surfaces always yield better performance. As for Type III anodization on machined 6061 surfaces, various samples are prepared that have different thickness and sealing conditions. The results show the thermal emissivity can be improved from 0.87 to 0.89 after the thickness of the AAO layer changing from 25µm [0.001in] to 66µm [0.0026in]. It also shows that the sealing method has a positive impact on the thermal emissivity to some extent, which has also been observed in the anodized die-cast samples.

2.3. Surface morphology

All the samples were imaged with a field emission scanning electron microscopy [Nova NanoSEM, Thermo Fisher Scientific] available in the 4D LABs at Simon Fraser University to capture the unique microstructures of anodic layers. The anodized samples were coated with 10nm iridium using a high vacuum sputter system [EM ACE 600, Leica Microsystems] before the imaging.

On anodized die-cast sample surfaces [Type III-Clear unsealed 25μm], two different surface structures are recorded as Figure 2.6, i.e., (a) the hexagonal textures, and (b) porous layer-stacked structures. Figure 2.6 (a) indicates that the anodic layer consists of individual areas in hexagonal shape where distinct boundaries separate each. The unevenly distributed pores are scattered around and hard to distinguish from the flakes stacked on top of each other within the area. On the other hand, Figure 2.6 (b) displays a rather different surface structure where the AAO films appear to pile layer-by-layer with miniature pores over the surface. We postulate that the formation of those two distinguishable yet different surface structures can be expressed as the surface imperfection in case of porosity. This commonly exists in the die-cast alloys that can be caused by several mechanisms to form voids and fine grain textures when gas being trapped and molten metal solidify at a different rate between the near-wall and internal regions, also the inclusion of impurities can create porosity in the die-cast parts. Additionally, the die-cast aluminum alloys have fairly amount of non-metal elements and impurities where the aluminum usually takes up only 80% to 90% of the compositions. The added constituents should have the undesired and opposite impact on the formation of anodic oxide (AAO) layer and account for this exceptional surface structure.

In terms of sealed AAO layers, Figure 2.7 presents a similar microstructure against the unsealed layer. Figure 2.7 (a) shows the completed surfaces after Type II-Black anodizing and (b) refers to the surface resulted from the Type III-Clear process. The boundaries that shape the cells are still partially visible on both surfaces from which it may indicate the thickness of sealant film is comparably thin. The stains or shadows on the dyed surface may be the residues of insufficiently absorbed coloring pigments that are attached on the surface due to the pore-less and layer-stacked microstructure. As for surface uniformity, Type III-Clear treated surface has comparatively high surface irregularity in contrast to the Type II-Black. It may indicate a potentially higher resistance to wear and corrosion.

Even with the different surface morphology observed on the completed surface finishes on the die-cast A380 Al alloy, the emissivity measurement from previous sections reveals the same improvement. What we may conclude from this observation is that the formation of aluminum oxidation or anodic oxidation lays the foundation for thermal radiative properties enhancement regardless of the auxiliary treatments, i.e., coloring and sealing, that may help to a limited extent.

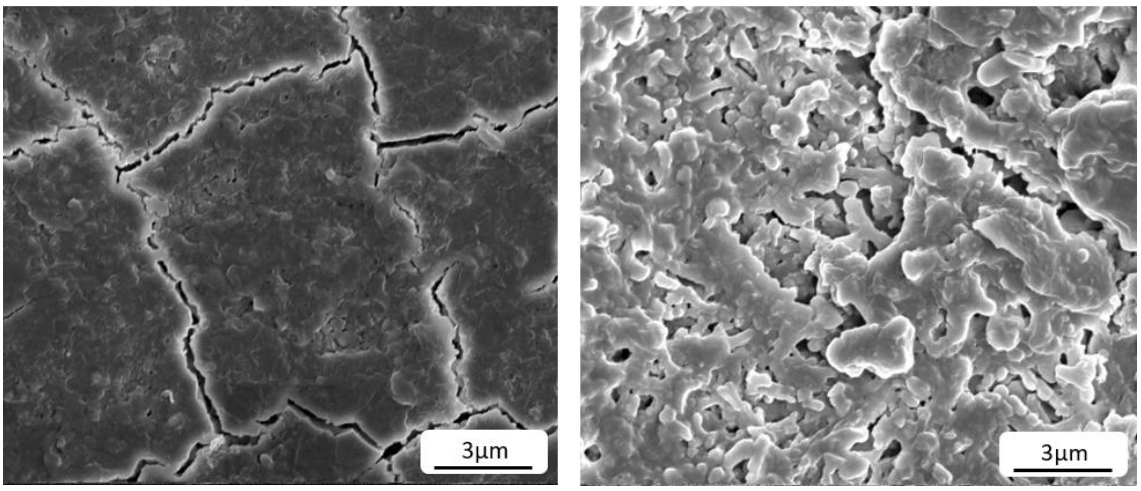

(a) (b)

Figure 2.6 Two different surface morphology observed from unsealed anodic layer formed on die-cast Al alloy A380: (a) "Hexagonally packed cells"; (b) Porous and layer-stacked structure

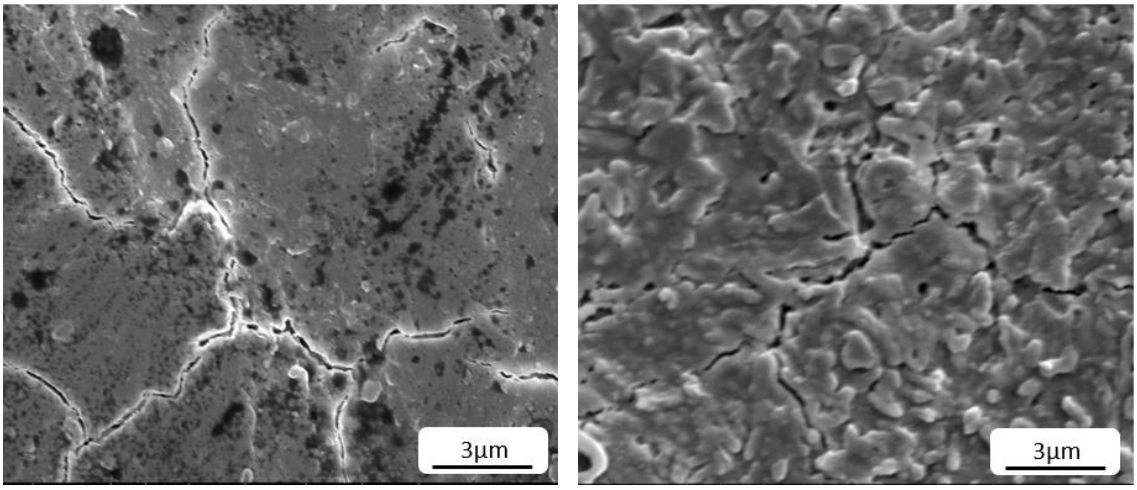

(a) (b)

Figure 2.7 Surface morphology of sealed anodized surface formed on die-cast Al alloy A380: (a)Type II-Black; (b) Type III-Clear

The surface structures of anodizing machined Al alloy 6061 [Type III-Clear unsealed 66µm] are including in Figure 2.8. The same hexagonal areas observed previously in the die-cast samples are also visible but on a smaller scale. With a higher magnification of 10,000X, the extreme miniature pores with an average diameter less than 10nm can be seen over the entire sample surface. The efforts have been made to apply the same magnification to the die-cast samples but we failed to observe any resembling structure. This explains the fact that Al alloy 6061 yields regular and much even surface

appearance compared with die-cast samples where the composition of aluminum alloys matters.

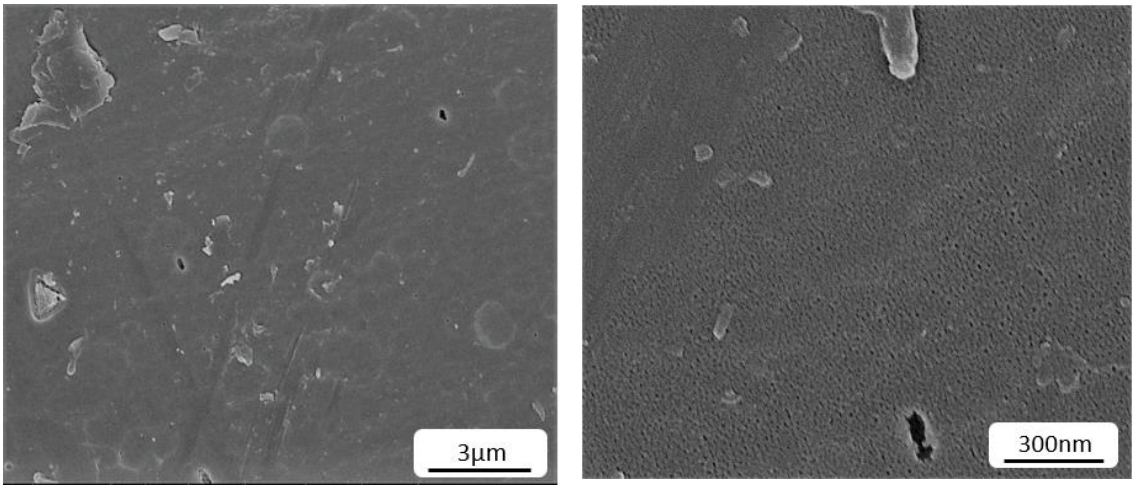

(a) (b)

Figure 2.8 Surface morphology of unsealed anodized surface formed on machined Al alloy 6061

2.4. Experimental setup

2.4.1. Testbed

The objective of this experiment is to investigate the thermal performance of the naturally cooled heat sinks (NCHx) made of die-cast aluminum alloy in case of natural convection and thermal radiation. A customized designed testbed was developed to perform the steady-state thermal test. As an effort to reduce the flow disturbance and provide a uniform radiation background, a specified test chamber [0.5m×0.5m×0.5m] was built with 4mm thick acrylic plastics. The surface emissivity of acrylic plastic is approximately 0.9 in the wavelength of infrared light with physical and thermal properties of density [ρ = 1180 kg·m^{-3}], thermal conductivity [k = 0.2 W·m^{-1}·K^{-1}], and specific heat [1470 J·kg^{-1}·K^{-1}]. Several ultra-thin polyimide film heaters with pressure sensitive adhesive were applied to the base of the heat sink to mimic the actual heat generation from electronic components. All the heaters have a power density of 1.6 W·cm^{-2} [10 W·in^{-2}] and are of three sizes, i.e., 1.3cm×5.1cm, 2.5cm×2.5cm, and 2.5cm×5.1cm. A programmable DC power supply [Chroma 62012P-100-50] was providing electrical power. T-type [copper-constantan] thermocouples were used to monitor the temperature distribution along the heat sink base, chamber ambient, and chamber walls. A NI-9212 [National

Instrument] temperature acquisition module and a NI-9229 [National Instrument] voltage analog input unit were connected to a compactDAQ [cDAQ-9174] chassis which transfers the recorded temperature and voltage measurement to the external computer to complete the data acquisition. The sample battery charger heat sinks were tested in the horizontal orientation as indicated in Figure 2.9. A centimeter-thick wooden plate board was placed underneath the heat sink to prevent any thermal leakage from the base of the heat sink. The front ports and gaps were also taped with aluminum foils to ensure the air-tight sealing for the internal region. Five ultra-thin polyimide film heaters and fourteen thermocouples were installed to conduct this thermal test. The detailed installing location of heaters and thermocouples can be found in the experimental schematic as Figure 2.9 where T7 and T11 were attached on the chamber wall to monitor the wall temperature.

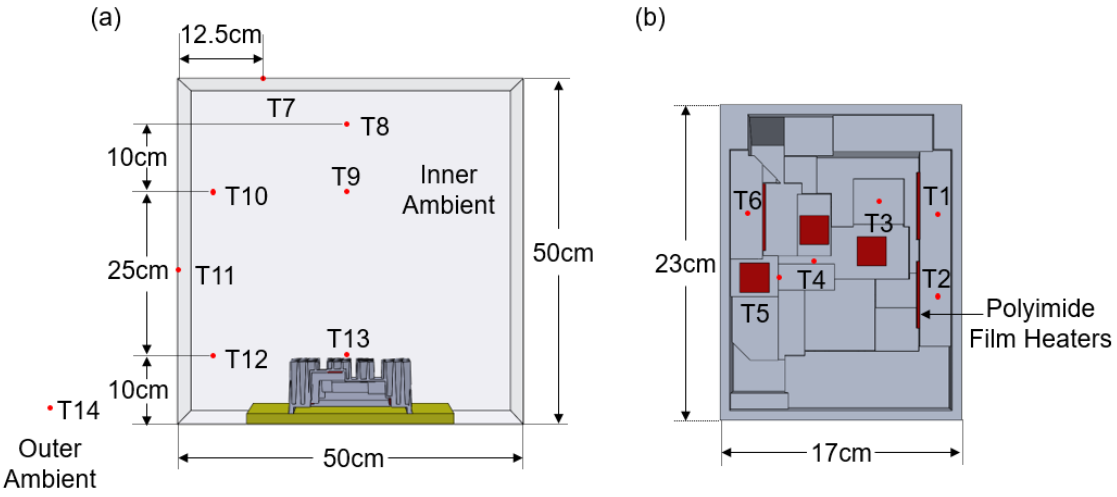

Figure 2.9 Schematic of the experimental setup, including locations of thermocouples and heating components (a) a customized-built test chamber; (b) back view of the tested heat sink

The thermal tests were performed in the open lab environment facing north, free of direct sunlight from the windows. The room temperature was steady and remain constant at 22℃. Each heat sink was tested with various power level from 20W to 80W. The steady-state condition was reached when the partial derivative of all temperature with respect to time $(\partial T/\partial t)$ was less than 0.001℃ for 30mins. This was considered as the thermal equilibrium on the interfaces of the tested heat sink and chamber wall, i.e., the summation of convective and radiative heat transfer leaving each interface became equal to the heat input into the battery charger heat sink. Thermal tests of each heat sink were

repeated at least three times to verify the validity of the experimental results. The actual data acquisition system and the testbed is shown in Figure 2.10.

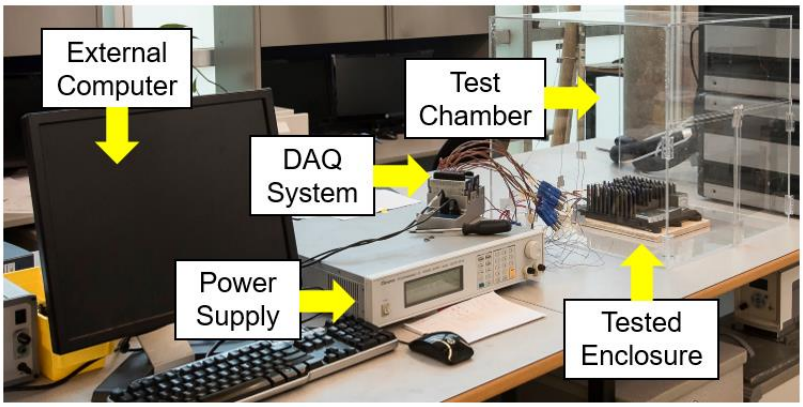

Figure 2.10 Components of the experimental setup

2.4.2. Uncertainty analysis

Voltage (U), current (I_0), and temperature (T) are three measured parameters in this experiment. The heat generation rate of the electrical heater should equal to the measured electrical power input of the systems which can be calculated as:

$$Q = P = U\, I_0 \tag{2.10}$$

According to the National Instrument datasheet, the voltage acquisition module has a maximum error of ±1.2% when it has not been calibrated. The error range for measured thermal input to the system has become ±1.7% based on the error propagation in Eq.2.11 as:

$$\frac{\delta \dot{Q}}{\dot{Q}} = \left[\left(\frac{\delta U}{U} \right)^2 + \left(\frac{\delta I_0}{I_0} \right)^2 \right]^{\frac{1}{2}} \tag{2.11}$$

T-type thermocouples have been used throughout the thermal test and have a maximum uncertainty of ±1℃ based on the manufacturer specification. Thus the uncertainty for temperature difference measurement between the heat sink surface and chamber ambient including the standard deviation of various runs can be expressed as:

$$\delta \Delta T = \left[(\delta T)^2 + (\delta T)^2 \right]^{\frac{1}{2}} \tag{2.12}$$

$$\delta\Delta T \cdot S = \left[(\delta\Delta T)^2 + {S_{\Delta T}}^2\right]^{\frac{1}{2}} \tag{2.13}$$

The maximum error for temperature difference is calculated as ±1.4℃ along with the standard deviation calculated based on the acquired experimental data. After obtaining uncertainty range for power input and temperature difference, the error for thermal resistance can be analyzed by:

$$\frac{\delta R}{R} = \left[\left(\frac{\delta \dot{Q}}{\dot{Q}}\right)^2 + \left(\frac{\delta T}{\Delta T}\right)^2\right]^{\frac{1}{2}} \tag{2.14}$$

The maximum calculated error for thermal resistance is ±6.4%.

2.5. Numerical analysis

The conjugated natural convective and thermal radiative heat transfer problem is highly couple via temperature where analytical approaches often fall short in predicting the rate of heat dissipation in terms of complex geometries. Numerical modeling, as an effective yet convenient tool, facilitates our deep understanding of the sophisticated behavior in conjugate heat transfer problem and enables us to decouple the amount of radiative heat transfer from the overall heat dissipation in the IC650 battery charger heat sink. Ansys Fluent 17.2 has been used to construct the numerical model where the results have been validated by the experimental data for the cases with various surface emissivity.

2.5.1. Assumptions

In this simulation, a 3-D numerical model is developed to seek out a steady-state solution for natural convective and radiation heat transfer from a commercially available heat sink. The fluid is assumed to be incompressible and the flow is within the laminar regime, i.e., Rayleigh number is below 10^8. The grey body assumption for the surface of the heat sink and chamber wall is used where the radiative properties, i.e., surface emissivity and reflectivity, are uniform and independent of the wavelength as well as surface temperature. Given that the thermal radiation between the heat sink surface and cooling fluid medium is small, we only consider the radiative heat transport phenomenon

on the surfaces in which any absorption, emission, and scattering effects happened in the cooling medium is ignored.

2.5.2. Governing equations

The general form of Naiver-Stokes equation for incompressible fluids, and along with the energy equation that governs the natural convective heat transfer problem are:

$$\nabla \cdot \vec{u} = 0 \tag{2.15}$$

$$\rho\vec{u} \cdot \nabla\vec{u} = -\nabla P + \mu\Delta\vec{u} - \rho g\nabla z \tag{2.16}$$

$$\vec{u} \cdot \nabla T = \alpha\Delta T \tag{2.17}$$

Where the gravity acceleration is parallel with *z* direction pointing downwards. ρ, μ, and α are the density, dynamic viscosity, and thermal diffusivity. Since the driving force for the fluid flow is provided by the buoyancy, the Boussinesq approximation is used for density-temperature relations, and it is assumed that the density is varying linearly with temperature when the difference between the heat source and the cooling medium is small, as:

$$\rho(T) = \rho_\infty\big(1 - \beta(T - T_\infty)\big) \tag{2.18}$$

$$\beta = -\frac{1}{\rho}\left(\frac{\partial\rho}{\partial T}\right)_P \tag{2.19}$$

Where β is thermal expansion coefficient and can be calculated using Eq.2.19. Substituting the density into the original equation and absorb the $\rho_\infty g$ into the pressure term with $\tilde{P} = P - \rho_\infty g$. Thus, the momentum equation with approximated buoyancy term becomes:

$$\vec{u} \cdot \nabla\vec{u} = -\frac{1}{\rho_\infty}\nabla\tilde{P} + \upsilon\Delta\vec{u} - g\beta(T - T_\infty)\hat{n} \tag{2.20}$$

Where ν is the kinematic viscosity that can be calculated as μ/ρ_∞ and $\hat{n}$ is the unit vector along the direction of gravity acceleration. The fluid properties needed for the modeling were acquired and calculated by the “online fluid properties calculator” available in Microelectronic Heat Transfer Laboratory (MHTL) in University of Waterloo [93].

Since we only consider the radiative heat transfer among surfaces, this “surface to surface” heat transmission analysis can be done by Fluent integrated “S2S” radiation model [94]. The total heat flux leaving a surface i with incident radiation from surfaces j can be represented as:

$$q_{out,i} = \varepsilon_i \sigma T_i^4 + \gamma_k \sum_{j=1}^{N} F_{ij} q_{out,j} \tag{2.21}$$

Eq.2.16 can be rewritten in the form of radiosity as:

$$J_i = E_i + \gamma_i \sum_{j=1}^{N} F_{ij} J_j \tag{2.22}$$

Where F_{ij} is called view factor between surface i and j that indicate the fraction of energy leaving surface j that incident on surface k. γ is the surface reflectivity and can be calculated as $\gamma = 1 - \varepsilon$ by Kirchhoff’s law of radiation. N represents the number of surfaces that interact with surface i and will shed radiation. The view factor between surface i and j is given by:

$$F_{ij} = \frac{1}{A_i} \iint_{A_k A_j} \frac{cos\theta_i cos\theta_j}{\pi r^2} \chi_{ij} dA_i dA_j \tag{2.23}$$

Where A, r are the surface area and distance. θ are the angle between the direction of radiation and surface normal. χ_{ij} is determined by the visibility of dA_i and dA_j where it equals to 1 if dA_i is visible to dA_j.

2.5.3. Boundary conditions

All solid walls, i.e., either heat sink surfaces and fluid domain walls, have the no-slip and non-penetration boundary conditions. For the frontal interface of the heat sink that in touch with the cooling medium where the heat is dissipated through the mechanism of natural convection and thermal radiation, the boundary conditions were set via system coupling. The adiabatic boundaries were imposed on the back surfaces of the heat sink given that we assume the heat can be only transferred out through the frontal faces. The constant volumetric heat flux conditions were given to the heat generating components

depending on the overall heat input into the systems resembling the actual experimental test. The chamber walls have a constant temperature, which was specified by the experimental results. The ambient temperature of the test chamber was first set to the room ambient, but because of the enclosed environment where heat will accumulate and can only be dissipated by the convection and radiation from chamber wall, the chamber ambient should increase and settle on a new temperature when the system final reaches the steady state.

The measured total hemispherical emissivity values were used as surface emissivity for the heat sink surfaces. The chamber walls have a uniform surface emissivity of $\varepsilon = 0.9$ as mentioned earlier.

2.5.4. Numerical schemes

The SIMPLE algorithm in Fluent 17.2 was used to solve the set of governing equations. The momentum and energy terms were discretized by the first-order accuracy Power Law scheme and PRESTO scheme was adopted in the discretization of the pressure term. Because of the high nonlinearity and instability of the natural convective flow, the Under-Relaxation Factors (URF) for momentum was set to 0.35 to dampen the solution and reduce oscillations.

When the variation of heat sink surface temperature was within 1×10^{-4} in last 100 steps while the residue for continuity, momentum, and energy was not diverging, we assumed the solution reached the steady-state and the iterations terminated. The calculation of radiation heat transfer has been carried out within each iterative step of fluid flow, and the convergence criteria were reached when its residue below 10^{-3}.

2.5.5. Mesh independence study

The mesh generation of this 3-D geometry was done by a universal meshing tool in Ansys Workbench 17.2, Ansys Mesh, due to its simplicity and versatility. It should be noted that the unstructured conforming mesh has been used due to the complex geometries of this problem, and the mesh elements were refined near interfaces as illustrated in Figure 2.11.

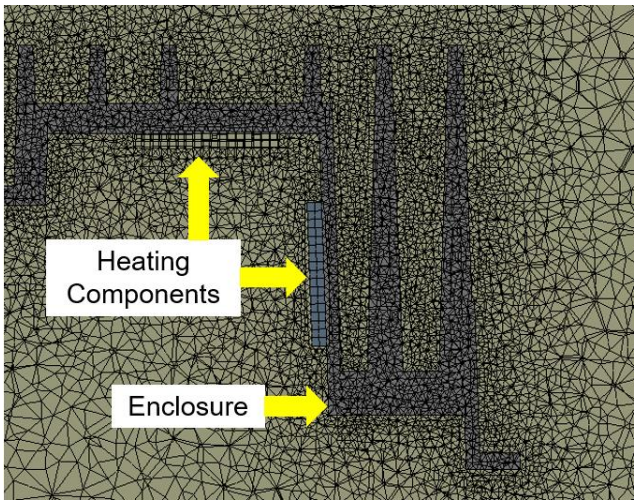

Figure 2.11 Unstructured conforming mesh elements of solid-solid (heating components and heat sink) and solid-fluid (heat sink and ambient fluid) interfaces

A mesh independence study was also carried out to investigate the effect of geometry sizing on the solutions. The benchmark case has been done with the thermal input of 40W in total and chamber wall with the temperature of 300K. The surface emissivity was chosen to be 0.92 to simulate the surface condition after the anodization. The heat sink was subjected to the horizontal orientation with gravity acceleration downwards. Other crucial numerical parameters were kept the same as described in the previous sections.

Figure 2.12 shows the results for the grid independence study where the average heat sink base temperature difference of the heat sink surface slightly varies with the number of mesh elements. The size of meshing on the heat sink surface was reduced proportionally from 3×10^{-3} to 1.5×10^{-3} with the sizing of the chamber reducing from 2.4×10^{-2} to 1.2×10^{-2}. As the number of elements increases from nearly 2,000,000 to 8,000,000, the temperature difference rises from 22.7℃ to 23.6℃. The results show the temperature difference was getting to a plateau when keep shrinking the geometry sizing. However, the computational cost should also take into account when the number of elements increases. Therefore, we took the finest mesh size of 1.5×10^{-3} and 1.2×10^{-2} on the heat sink surface and in the computational domain where the time cost and the result accuracy is acceptable.

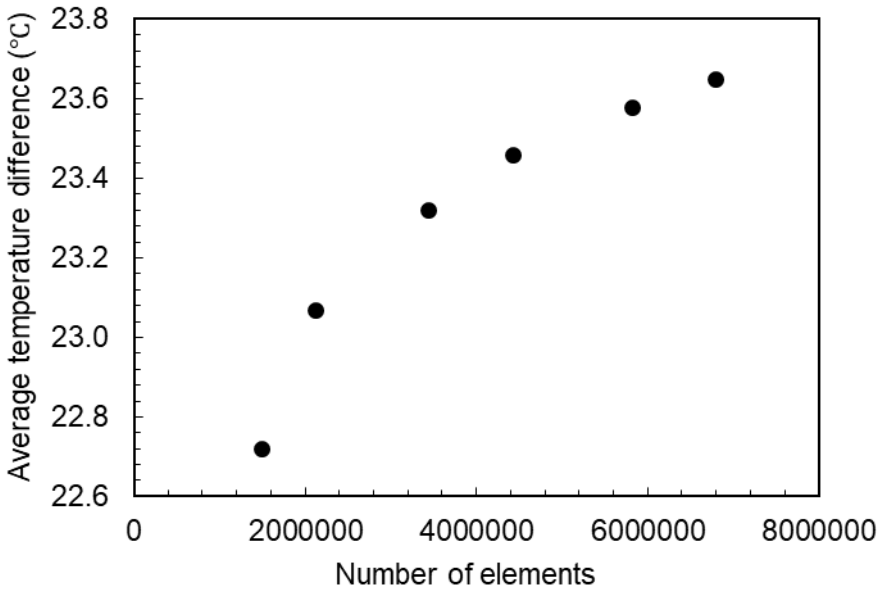

Figure 2.12 Mesh independency study, average temperature change with respect to the number of elements

2.6. Results and discussion

2.6.1. Experimental results

The thermal test results of bare and anodized heat sinks are provided in this section. The reported values are averaged to all recorded thermocouple readings within the last minute. The horizontal uncertainty bars represent the calculated error for input power measurements, which is ±1.7%. The vertical uncertainty bars are defined as the computed uncertainty for temperature measurement as well as thermal resistance. The maximum uncertainty thermal resistance is calculated as ±6.4%.

Figure 2.13 shows the average base temperature with reference to the average chamber ambient temperature, and Figure 2.14 represents the average heat sink base temperature. As shown, anodization significantly improves the overall thermal performance of treated heat sinks compared to the bare samples. The average base temperature difference drops approximately 6℃, 12.3% in relative term, for the input of thermal power 80W. Even for a thermal power of 20W, a reduction of 14.7% in average base temperature can be seen where thermal radiation is expected to be less prominent as the surface temperatures are lower.

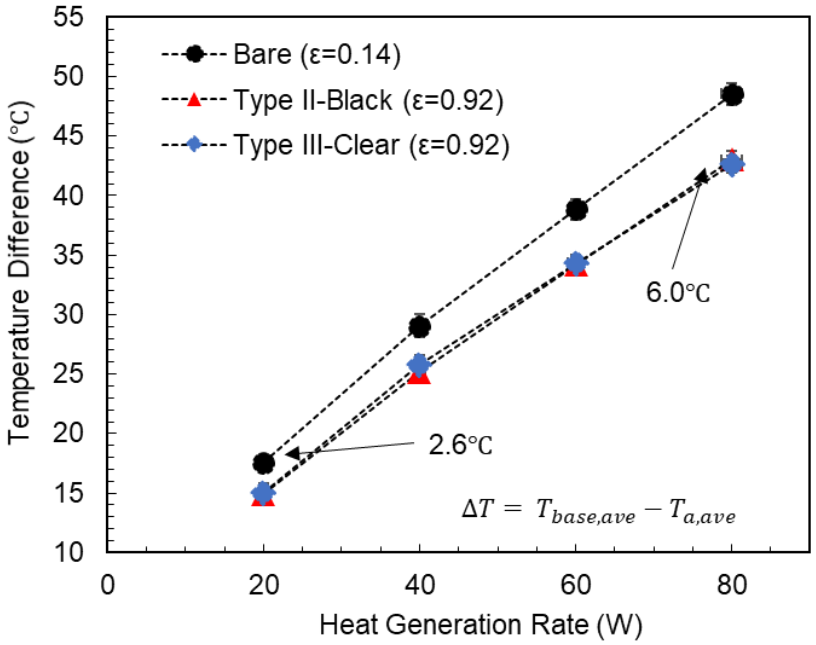

Figure 2.13 Average temperature difference between the heat sink base and chamber ambient

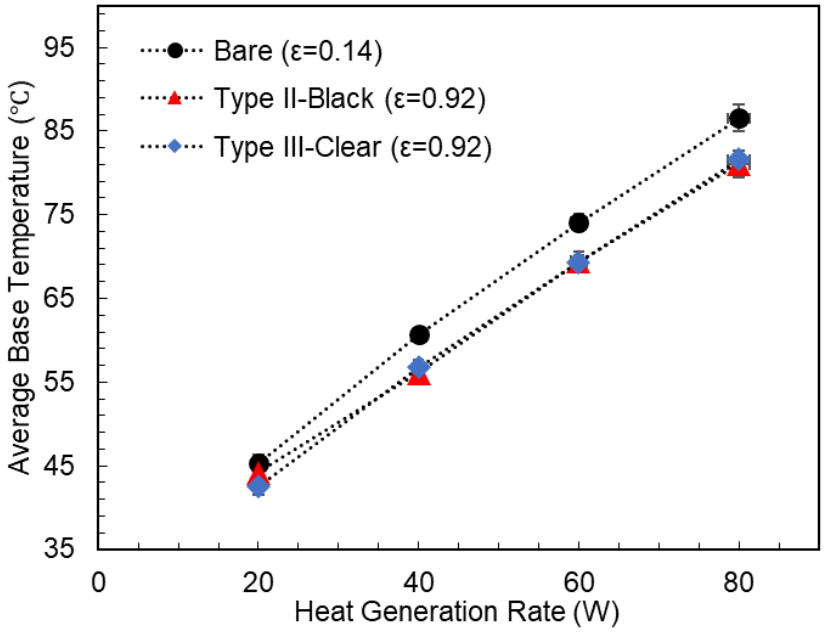

Figure 2.14 Experimental data of average heat sink base temperature

Figure 2.15 shows the overall thermal resistance including both radiation and convection. It is defined between the average heat sink base temperature and the total heat generation rate as:

$$R = \frac{T_{base,ave}}{Q} \tag{2.24}$$

The results indicate a significant improvement of 14.7% is achievable after anodization. The overall thermal resistance is reduced from 0.61K·W^{-1} to 0.53K·W^{-1} when the heat input is maintained at 80W. This further confirms the crucial impact of anodization on the thermal radiation and the overall thermal enhancement of die-cast heat sinks. It should also be noticed that the thermal resistance for natural convection and thermal radiation is decreased drastically when the power input into the system is increased from 20W to 80W; since the heat sink base temperature is increased notably. Indeed, higher temperature gradient provides more driving forces for the heat transfer which in turn leads to a reduction of the overall thermal resistance as shown in Figure 2.15. Nevertheless, the impact of anodization on the overall thermal resistance stay in line with reported temperature difference where a considerable enhancement could be found.

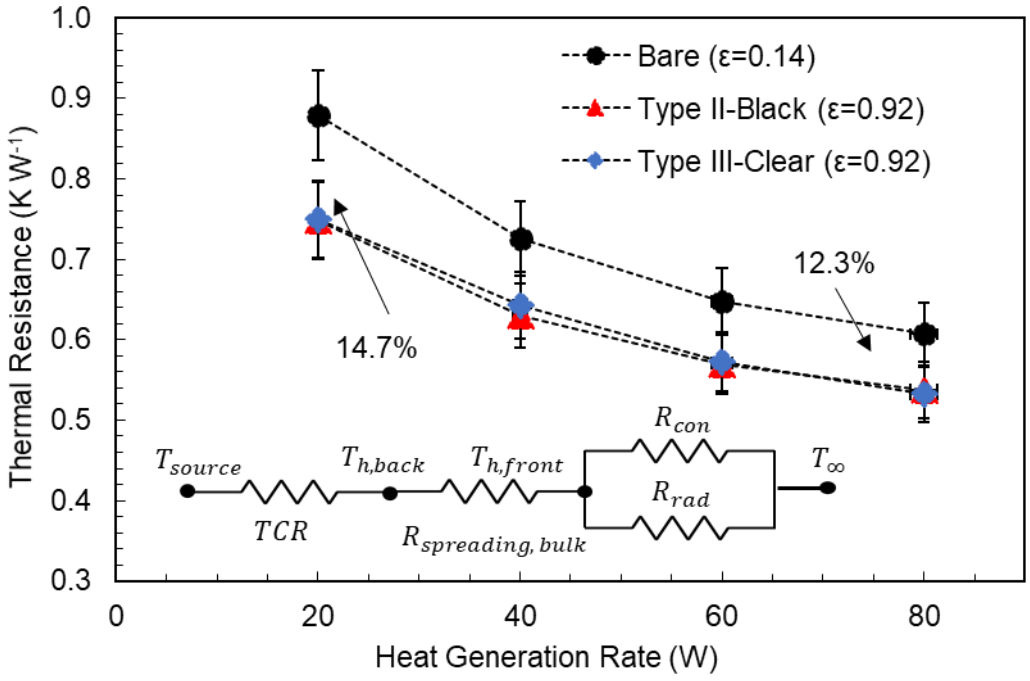

Figure 2.15 Total thermal resistance in case of natural convection and thermal radiation from various tested heat sinks

2.6.2. Numerical results

Figure 2.16 shows the comparison between the numerical results and the experimental data in the form of the temperature difference between the average heat sink

base and average ambient. The solid symbols represent the measured values from various experiments, and the solid lines denote the predictions from the numerical model. As shown, there is a good agreement between the numerical and experimental results with maximum relative differences of 2.1% and 7.0% in the case of surface emissivity of 0.14 and 0.92, respectively. After validation of the numerical model, it can be used to estimate the contribution of thermal radiative to the overall passive cooling capacity of such heat sinks.

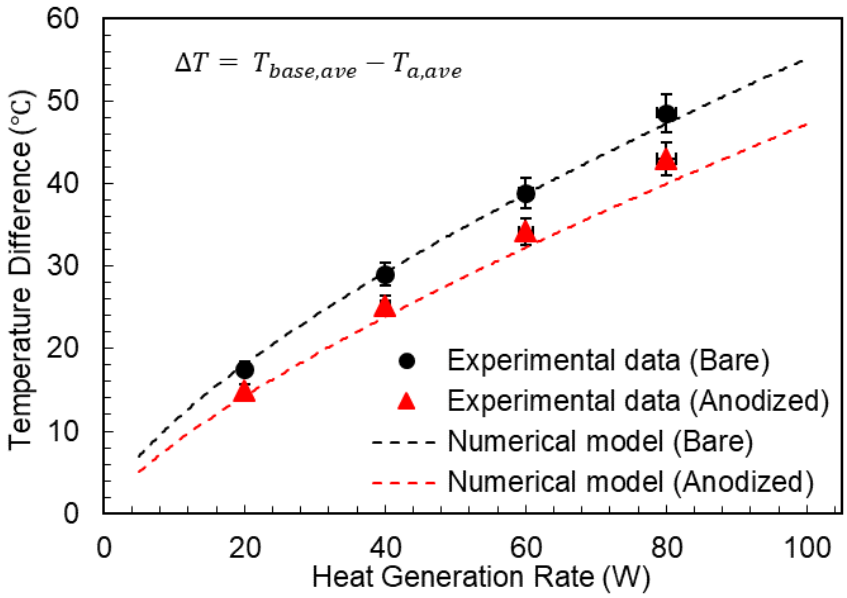

Figure 2.16 Comparison between presented numerical model (solid lines) and experimental data (solid symbols)

The importance of thermal radiation in our naturally cooled heat sinks (NCHx) is shown in Figure 2.17. The actual amount of the radiative heat transfer shows in Figure 2.17 (a), and the proportion of thermal radiation to the overall heat transfer is reported in Figure 2.17 (b). For bare heat sinks ($\varepsilon = 0.14$), the contribution of thermal radiation varies from 3.2W [16%] to 12.5W [12.5%] with increasing thermal power from 20W to 100W. As for anodized heat sinks ($\varepsilon = 0.92$), radiation plays a pivotal role as expected. For our heat sinks, the amount of radiation increases from 8.3W [42%] to 32.9W [33%] for an input varying from 20W to 100W. This clearly indicates that the potential for improving the radiation in naturally cooled heat sinks (NCHx). The results also show that the radiation plays an even more critical role when the temperature difference is smaller, i.e., where the driving force for natural convection is less substantial.

In principle, the radiation will expedite the heat dissipation rate and can be perceived as a decrease of the surface temperature where the driving force for the natural convective flow is minimized in the meantime. However, the experimental and numerical results show that the reduction in temperature difference has less impact on the combined thermal performance. The enhancement of surface emissivity not only can lead to a major improvement in thermal radiation but also it is an effective means to expand the heat removal capacity of heat sinks which is desirable and of great application in practice.

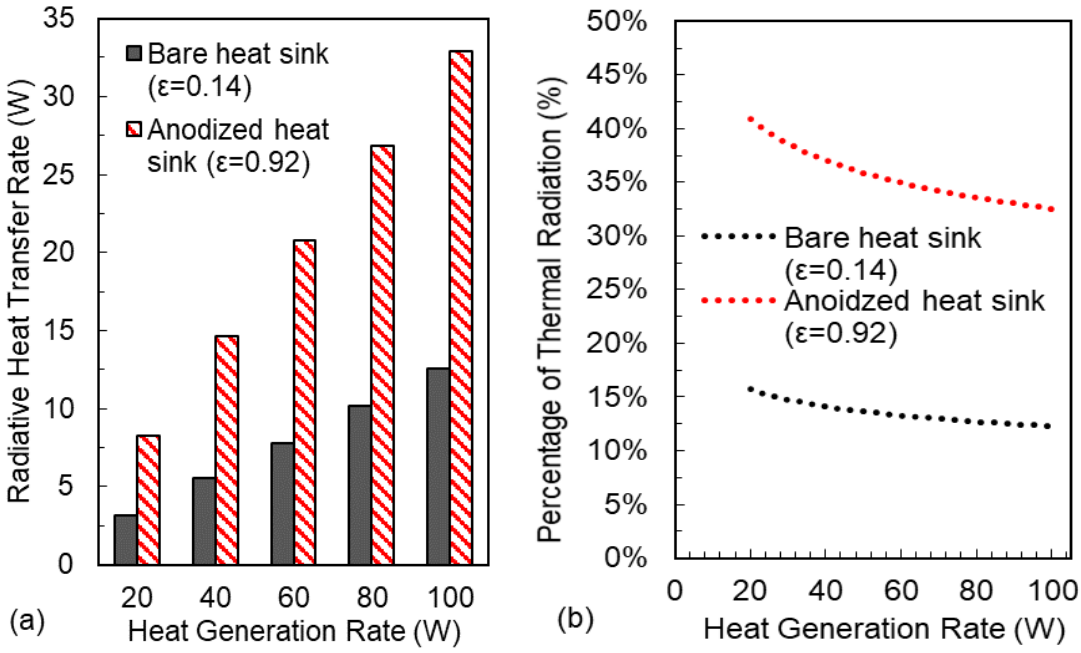

Figure 2.17 Radiative heat transfer from bare and anodized heat sinks (a) Radiative heat transfer rate; (b) Percentage of the thermal radiation in overall heat dissipation

2.7. Conclusion

A comprehensive study of surface radiative properties of anodized aluminum and its effect on thermal radiation from naturally cooled heat sinks (NCHx) is presented. The emissivity measurements suggest a great improvement from all types of anodizing treatment on either die-cast or machined aluminum alloys with a small variation of thermal emittance. A customized testbed was built, and a series of anodized naturally cooled heat sinks were tested. The experimental and numerical modeling results show an increase of thermal emissivity on the heat sink surface can considerably reduce the surface average temperature, eliminate regions with relatively higher temperature, and increase the heat

removal capacity. In this particular heat sink geometry, thermal radiation can account for maximally 41% of the overall heat dissipation.

Chapter 3.

Comparison between various fin geometries under natural convection and thermal radiation

The impact of various fin geometries on natural convection and thermal radiation is explored and studied experimentally and numerically in this chapter. A number of NCHx are prototyped and machined with various fin shapes and arrangements including, 1) benchmark design resembling original IC650; 2) inclined interrupted fins; 3) straight interrupted fins; 4) pin fins. The influence of orientation on the overall thermal performance is also investigated. The sample NCHx are tested subjected to three orientations which are horizontal, vertical, and sideways. In the case of tests where it has the surface emissivity of 0.03 (machined surfaces of aluminum alloy 6061), the results show only inclined interrupted fins can deliver the desired thermal improvement at all three orientations compared to the original IC650 design. The straight interrupted fins fail at sideways orientation, and pin fins only perform well at horizontal orientation. The test results of anodized heat sinks (surface emissivity of 0.89) unveil a reduction of thermal resistance up to 27% depending on the fin geometries and test orientations.

3.1. Problem statement

Fin shapes have a profound influence on the heat transfer behavior of a heat sink and the studies of various fin geometries have always been the focus in the exploration of efficient and cost-effective cooling methods. Especially for the natural convective heat sinks, a minute alternation of the fin geometries or directions can greatly impact the resistance for both fluid flow and heat transfer. The literature review on the topic of natural convection from finned heat sink can be found in section 1.4.3 where the previous efforts of the individual studies of straight, inclined, interrupted and pin fins have been reviewed and summarized. Despite the prior noteworthy works in each particular fin geometry, it is challenging to implement those results for the real design where most of the investigations are conducted with diverse heat sink footprints, i.e., base area, volume, and height. Furthermore, the vast majority of the studies regarding natural convection from finned heat sinks are only subjected to the vertical orientation where it is explicitly implied by the direction of gravity acceleration where the thermal, as well as the hydraulic resistance,

can be minimized. The understanding of orientation effects, particularly in respect of specific fin geometries, e.g., the inclined and interrupted fins, is needed to enable the idea of the adaptable heat sink that can operate under various orientations.

3.2. Heat sink prototyping

3.2.1. Die-cast manufacturing constrains

We intend to mimic the heat sinks that can be manufactured using aluminum die-cast technologies. However, there are some limitation of features resulting from the die-casting process and can be summarized as Table 3.1 [95].

Table 3.1 Preliminary comparison for heat sinks with 40 to 60 mm tall fins in die-casting

Description of features	Die-casting
Fin geometry (plate, pin, etc.)	All types
Minimum Enclosure wall thickness (mm)	2 - 4
Minimum fin to fin spacing (mm)	5
Minimum fin tip thickness (mm)	2.5 - 3
Minimum fin angle (degree)	1 - 1.5
Porosity (%)	3 - 7
3D near net shape rating (5 is best)	5
Surface quality rating (5 is best)	2
Leak tight rating (5 is best)	2
Aluminum Alloys	ADC 10 - 12 or 3xxx

3.2.2. Geometrical details

As mentioned earlier, four heat sink with various fin geometries were prepared and prototyped, bearing the same footprints as the existing IC650 heat sink from Delta-Q Technologies. All heat sinks were prototyped using CNC machining tool located in School of Mechatronic Systems Engineering, Simon Fraser University, with aluminum alloy 6061-T6 [thermal conductivity $k = 150$ W·m^{-1}·K^{-1}]. All the heat sinks had the base size of 18cm×16cm and the fin height of 6cm. The height of the heat sink base was maintained at 0.35cm. A draft angle was imposed on the fins, 1.5° for IC650 design and 1° for rest of

heat sinks, out of consideration to resemble the actual fins manufactured from the die-cast process that may have potentials to affect the overall thermal performance. Figure 3.1 shows the prototyped heat sinks. The detailed consideration and dimensions for each heat sinks were discussed as below.

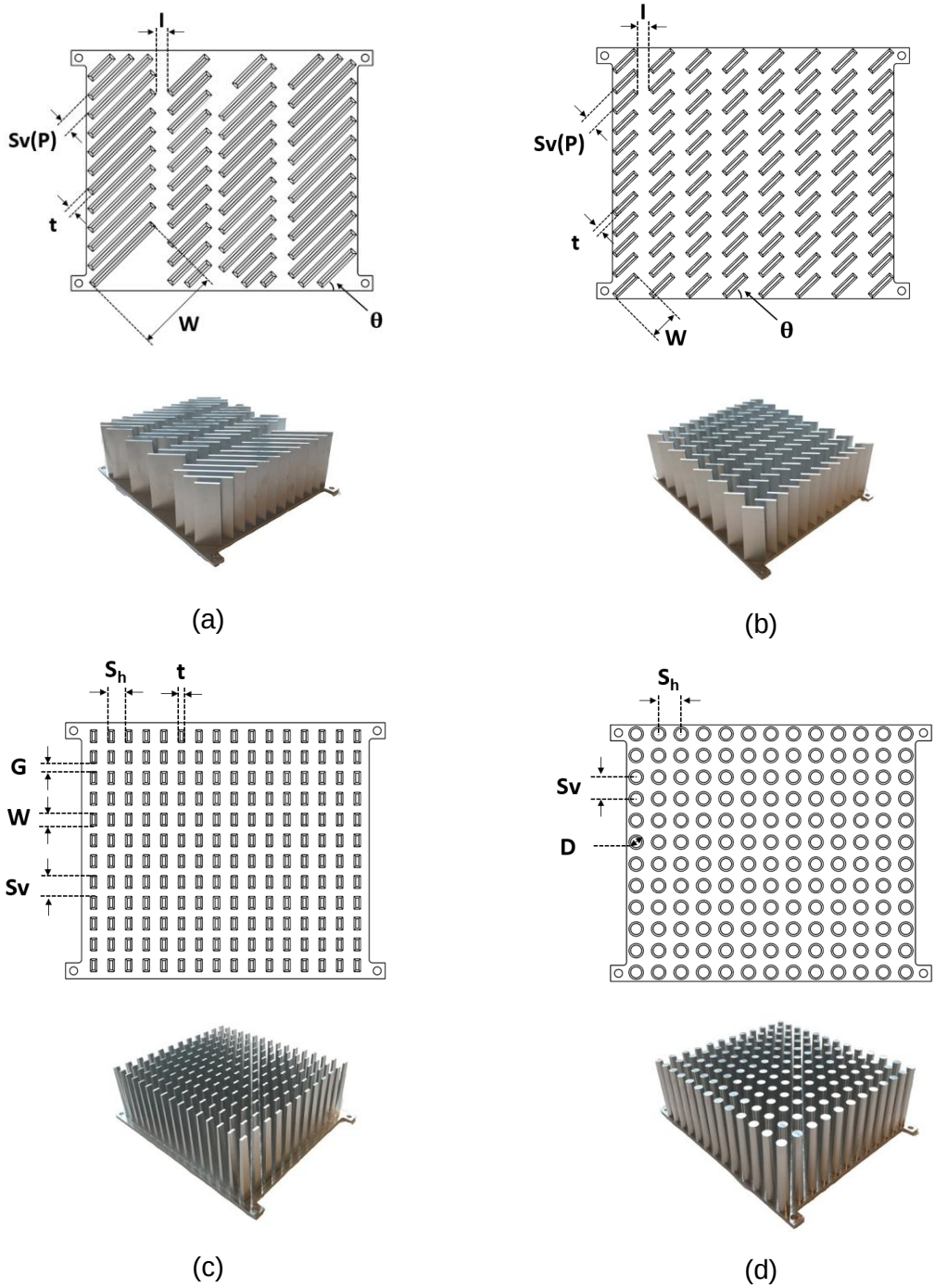

Figure 3.1 Prototyped heat sinks (a) IC650 design; (b) Inclined interrupted fins; (c)straight fins; (d) pin fins.

The IC650 heat sink design was provided by the company and served as the benchmark case to illustrate the potential improvement by varying the fin geometry. The inclined interrupted fins simply took the idea of interruption where the long inclined fins on the IC650 have been sectioned into shorter fins to interrupt the thermal and the velocity boundary layers so as to increase the overall thermal performance. In the inclined interrupted fin design, eight columns of the relative short fins replaced the initial four columns of long fins with varying lengths. The number of fins in each column were kept the same. The fin spacing of the new design was slightly expanded due to the reduction of the draft angle from 1.5° to 1°. The rest of the geometrical dimensions were maintained similar to the fin design of IC650.

The proposed straight interrupted fin design was based on the works by Ahmadi et al. [79][82] where they performed a series of studies with highlights on modeling, experiments to investigate the effect of interruption in straight continuous fins at the vertical orientation. A heat sink design procedure has been suggested to find the best fin arrangement to maximize the total heat transfer from interrupted fin heat sinks. They discovered that the optimum fin spacing for interrupted fins remains unchanged as compared with continuous fins, and it can be calculated by the correlation provided in [35]:

$$S_{opt} = 2.714\left[\frac{\upsilon\alpha L}{g\beta(T_w - T_\infty)}\right]^{\frac{1}{4}} \tag{3.1}$$

The chosen of gap distance is usually out of considerations such as manufacturing, cost, and weight because the increase of gap length has an adverse effect on the overall thermal performance as their study implies. Thus we settled on 0.5cm for a trial. The length of the fin was set to 0.8cm based on the optimal ratio of the fin length to the heat sink, which is approximately 0.5.

For the in-line arranged pin fins under natural convection at both horizontal and vertical orientation, many studies [84][88] suggest that the optimal ratio between pin diameter to spacing [center to center] was 1/3 with premises of small size of pins, the diameter is usually less than 0.5cm. Most of the empirical relations were correlated from limited experimental data sets, and cautiousness should be taken into accounts when performed an optimization study. In this case, the pin diameter was pre-set as 0.69cm as the same size of the ejector pins on the current die-cast model to mimic the actual castable

heat sinks. The pin diameter at the bottom was 0.90cm because of the draft angles imposed on the fins. Thus a numerical investigation on the effect of pin spacing was carried out based on the conjugate numerical heat transfer model developed in Section 2.5 from Chapter 2. The boundary condition for the fluid domain walls that were changed to pressure outlets to assume the opening conditions rather solid walls from the consideration of fast convergence rate.

The starting trial point for the vertical pin spacing was with the center to center distance of 1.31cm, and it has increased to 1.71cm steadily. The horizontal center to center spacing was always slightly larger than vertical spacing because the base size of the heat sink [18cm×16cm] which allow relatively bigger horizontal sizing even with one more column of fins was accommodated. The reason for choosing this particular dimension of the heat sink base, as mentioned earlier, was trying to match the actual dimension of product IC650 and keep the same footprint. Figure 3.2 (a) shows the varying trend of the vertical center to center distance regarding of horizontal face to face spacing. Figure 3.2 (b) shows the average temperature variation with regard to the vertical spacing. It clearly shows an optimal point existed for this particular case with a pin diameter of 0.9cm at the bottom. A competing trend resides between the heat transfer capability and overall surface area which are directly associated with the pin spacing. When fin space sizing is small, the heat removal capacity is greatly minimized by rejecting airflow through/around the pins despite the larger surface area can be gained by the small spacing and vice versa. The numerical modeling results show that the optimal horizontal center to center spacing is around 1.4cm for both horizontal and vertical orientations.

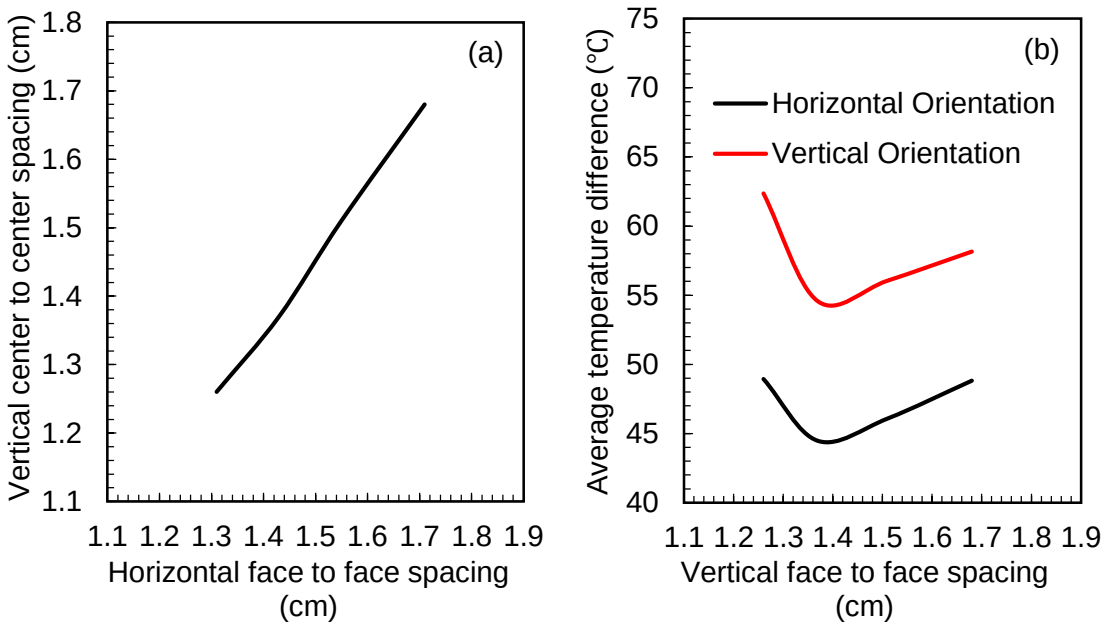

Figure 3.2 Preliminary parametrical study of pin spacing: (a) The varying trend of vertical to horizontal face to face spacing; (b) Effect of vertical face to face spacing on the average temperature difference

In summary, the comparison of geometrical dimensions between each heat sink is summarized in Table 3.2. The reported length values are the center to center distance at the bottom of the fins given the fact that a small difference of fins spacing existed between the top and bottom of the fins due to the introduced draft angles.

Table 3.2 Comparison of geometrical dimensions between each heat sink

Geometrical parameters	Inclined fins (benchmark)	Inclined Interrupted	Straight Interrupted	Pin Fins
Fin vertical spacing (S_v) [cm]	0.89	0.95	1.30	1.37
Horizontal Fin Spacing (S_h) / Column distance (l) [cm]	0.50/0.80	0.70	1.09	1.42
Fin Width (W) [cm]	3.50/6.00	1.90	0.80	-
Fin thickness (t) / diameter (D_t) at fin top [cm]	0.18	0.18	0.18	0.69
Fin thickness (t) / diameter (D_b) at fin bottom [cm]	0.49	0.39	0.39	0.90
Fin inclined angle (θ) [°]	45	44	-	-
Draft angle [°]	1.5	1.0	1.0	1.0

Number of Fins in each Columns (*n*)	12	12	12	12
Column number (*N*)	4	8	16	13
Surface area (*A*) [m^2]	0.31	0.26	0.25	0.26
Weight [kg]	1.47	1.07	0.92	1.52

All prototyped heat sinks were also anodized in the same local surface finishing vendor, “Spectral Finishing, Inc.”. Type II-Black anodization, as the most commonly used type of anodizing treatment in commercial products, was chosen as an example to investigate the potential thermal improvement by anodization. The emissivity investigation was also conducted that already presented in Chapter 2.

3.3. Experimental setup

The custom-built test chamber from anodization study was used to accommodate the prototyped heat sinks for the natural convection and thermal radiation experiments. The tested heat sink was mounted on an insulation substrate with a structure of wooden plate [1cm], Plexiglas foam [2cm], and wooden plate [1cm]. An electrically insulated Kapton heater of size 10cm × 15cm was applied at the back of the heat sink providing the thermal inputs to the system with high thermal conductive paste in between to minimize the thermal contact resistance within the heater and baseplate. Sixteen T-type thermocouples were used to monitor the temperature distribution along the heat sink base, chamber ambient, and chamber walls. The data acquisition systems of temperature [NI-9212] and voltage [NI-9229] from National Instruments as well as the Chroma programmable DC power supply [62012P-100-50] have comprised the rest of testbed. The schematic of the experimental setup displays in Figure 3.3.

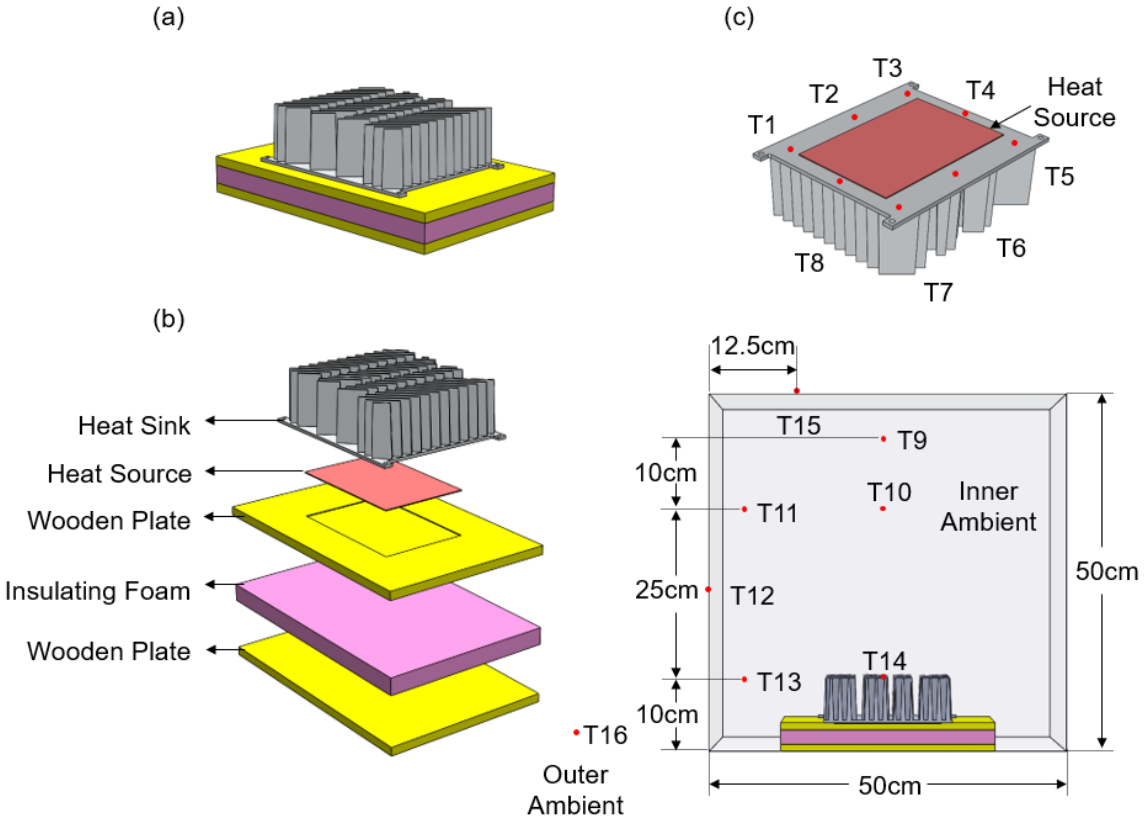

Figure 3.3 Schematic of testbed: (a) Assembled tested heat sink; (b) Split view of heat sink test substrate; (c) Location of thermocouples

All measurements were carried out in the open lab environment. Each heat sink was tested with regard to thermal power ranging from 20W to 100W at all three orientations, i.e., horizontal, vertical, and sideways. The ambient temperature in the lab was maintained at 22℃. Thermal tests of each heat sink were repeated at least three times with the steady-state criteria of $\partial T/\partial t$ is less than 0.001 for 30mins. Each prototyped heat sink was tested in the same manner before and after the anodization. Figure 3.4 shows the schematic of the heat sink test mechanism.

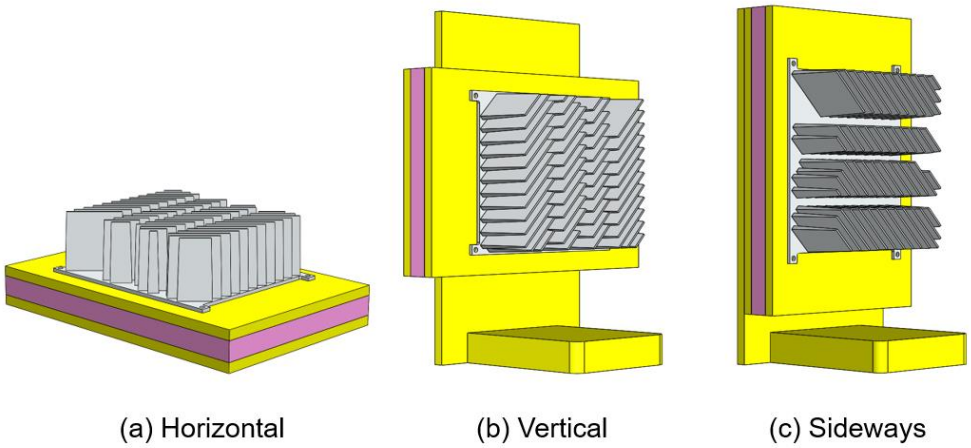

Figure 3.4 Test orientations: (a) Horizontal; (b) Vertical; (c) Sideways

The uncertainty for the temperature measurement can be propagated through the same set of the equations in Section 2.4.2, Chapter 2. The maximum error for uncalibrated voltage sensor is ±1.2% and T-type thermocouple is ±1.0℃. The calculated error for input power is ±1.7%, and the uncertainty for temperature difference is ±1.4℃ with the standard deviation of experiment data.

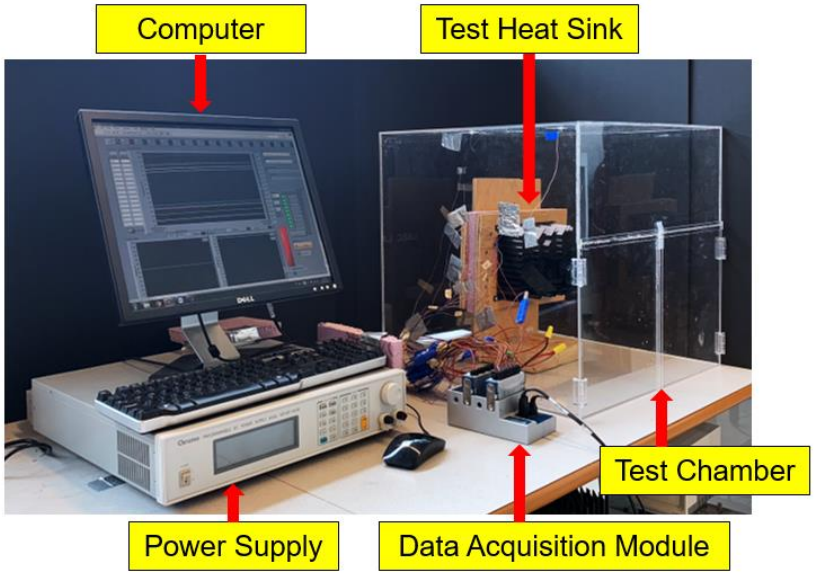

Figure 3.5 Experimental Setup in case of the anodized heat sink with IC650 fins tested at vertical orientation

3.4. Numerical analysis

A 3-D numerical model was developed by Ansys Fluent 17.2 in order to investigate the thermal performance of targeted heat sinks for natural convection and thermal radiation. The laminar model for fluid flow and surface to surface [S2S] radiation model was used. The Boussinesq assumption was imposed to the air density as a function of temperature. The detailed governing equations and assumptions were similar to the description in Section 2.5, Chapter 2. All the walls have non-slip and no penetration boundary conditions. For the heat sink walls, the boundary conditions were determined via system couplings. Constant heat flux was assumed at the back of the heat sink as the heat input. The fluid domain walls have a constant temperature with the measured value from the actual experiment. The surface thermal emissivity for the machined and anodized surface was 0.03 and 0.89 as obtained from emissivity study. The surface emittance for the ambient walls were 0.9 throughout all simulations.

3.4.1. Mesh independence study

The mesh independence study was conducted in the case of current IC650 fins to ensure the validity of the numerical solution. Figure 3.6 shows the alteration of average base temperature with regard to the number of elements where the thermal input of the system remained at 80W with the wall temperature of 300K and surface emissivity of 0.98. The numerical solutions were attained where the gravity acceleration was pointing downwards. As the size of mesh elements reduce in which the number of elements increases, the rate of change of base temperature difference tends to minimize and further reduction of meshing size has no significant influence on the results. Ideally, if the computational cost is not a limitation, the finer grid always yields the most accurate results. However, a choice of mesh element number of approximately 6,000,000 shows a 0.11% deviation from the simulation with a number of meshing element around 8,000,000. At the same time, the computational demand for the former case is less severe and acceptable. Thus, we chose the element number of 6,000,000 for intended simulations where the meshing size on the heat sink surface is 1.5×10^{-3} and 1.2×10^{-2} for the chamber volumes.

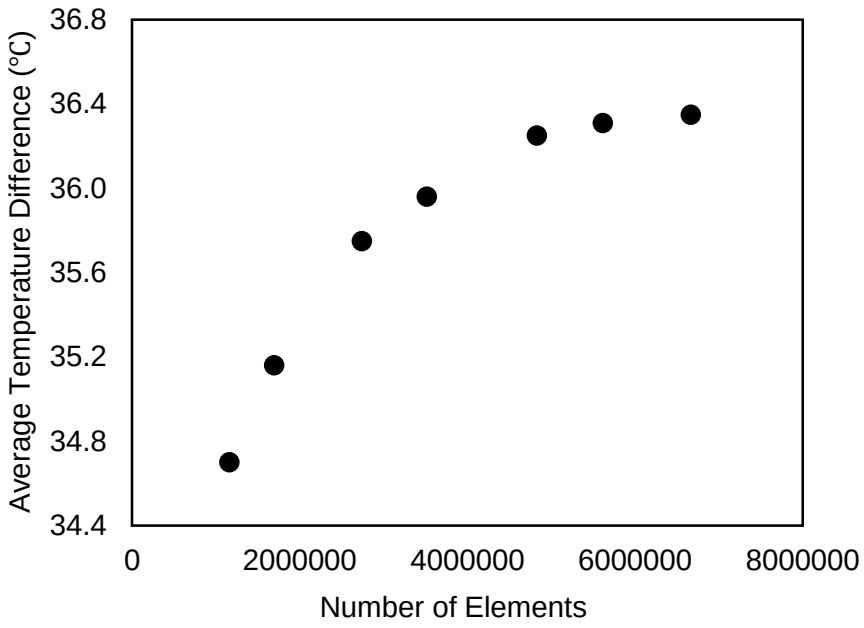

Figure 3.6 Mesh independence studies of benchmark geometry

3.5. Results and discussion

In this section, the experimental test results for prototyped heat sinks with various fin geometries are presented in an order of before and after the anodization. From the emissivity studies, we know that the measured surface emittance for the machined aluminum surface is 0.03 where most of the heat transfer happened on the heat sink surface are contributed by natural convection. After surface anodization, the thermal test results are used to validate the numerical model where the amount of radiative heat transfer can be extrapolated from the numerical simulation results.

3.5.1. Effect of fin geometries (ε=0.03)

Figure 3.7 shows a comparison between the experimental results for each prototyped heat sink with the bare surface (ε=0.03) and the numerical results at all three orientations. Temperature difference represents the average heat sink base temperature with reference to the average chamber ambient. The solid symbols indicate the experimental results and the numerical results are shown as solid and dash lines. As shown, the experimental results are in a good arrangement with the present model, with a maximum 5% difference in horizontal orientations, 4%, and 12% maximal discrepancies in vertical and sideways orientations, respectively. It should be noted that the heat flux

variance showed on the figure is a result of the difference in heat dissipation area where the proposed finned heat sinks have the relatively small surface area compared to the benchmark design. The following can be concluded from Figure 3.7 (a): i) overall thermal performance of all proposed heat sinks have improved compared with the inclined fins design at horizontal orientation; ii) both straight and inclined interrupted design can also yield a significant improvement, approximately 17% and 14% with a thermal input of 100W, while the pin fins can provide up to 20% reduction in average base temperature. In terms of thermal performance at vertical orientation shown in Figure 3.7 (b), the straight interrupted fin design offers the most considerable thermal improvement [15% at 100W] and inclined interrupted fins are also able to reduce the average base temperature around 5℃ with a heat input of 100W. On the other hand, the pin fins fail to have any improvement and it may cause by the relative larger pin diameter that we choose for this special case. As shown in Figure 3.7 (c), the heat sinks performance comparison for sideways orientation. Only the inclined interrupted design is capable to offer 11% reduction in average temperature difference where both straight interrupted and pin fins have a limited contribution to the overall heat transfer due to the geometrical constraints on the airflow. Overall, the thermal impact of fin geometries is prone to the orientation effects where most of the proposed heat sinks can only achieve the desired thermal performance at a specific orientation. However, the inclined interrupted fins design has the versatility to provide a notable amount of thermal enhancement at all three orientations.

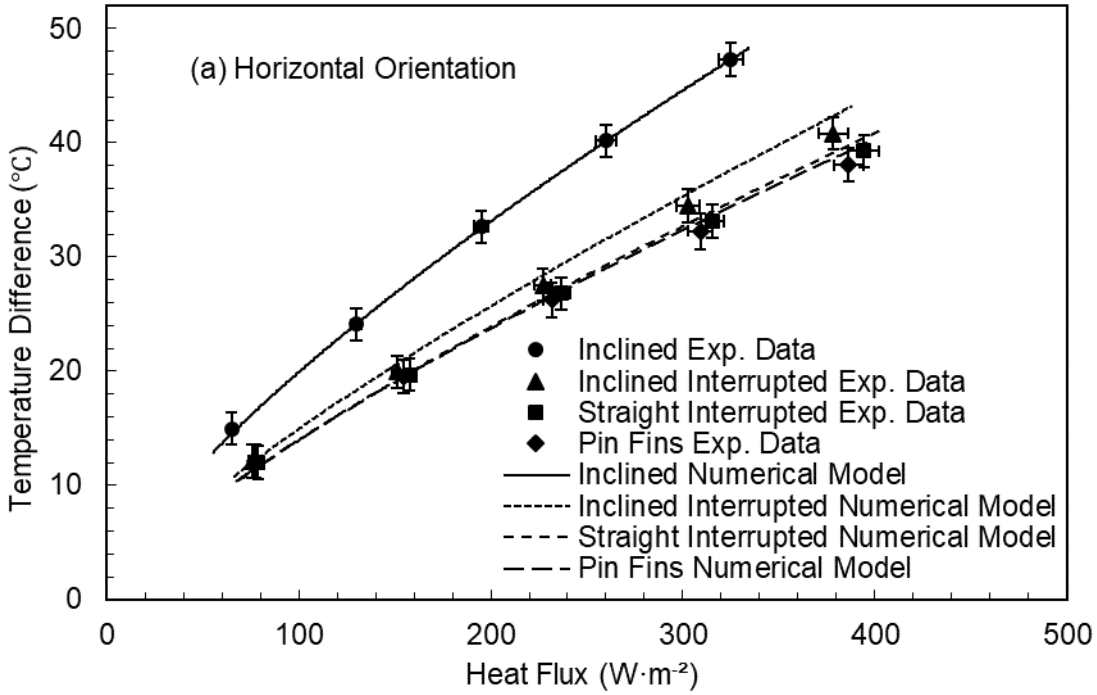
(a) Horizontal Orientation
Temperature Difference (°C)
Heat Flux (W·m⁻²)
0
10
20
30
40
50
0
100
200
300
400
500
Inclined Exp. Data
Inclined Interrupted Exp. Data
Straight Interrupted Exp. Data
Pin Fins Exp. Data
Inclined Numerical Model
Inclined Interrupted Numerical Model
Straight Interrupted Numerical Model
Pin Fins Numerical Model

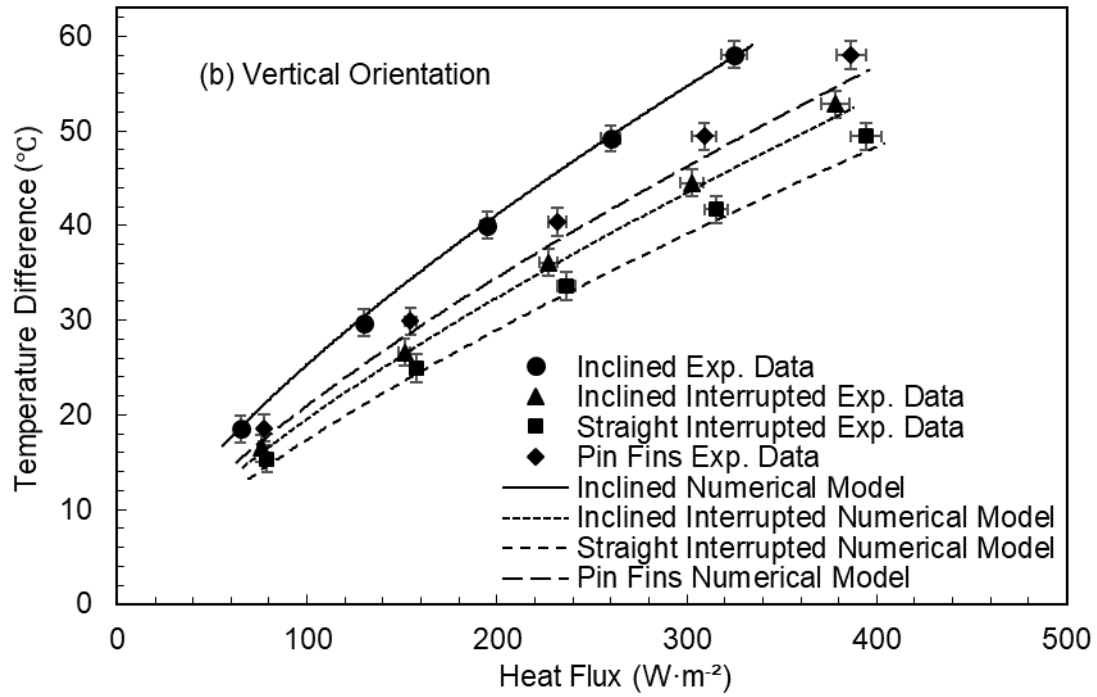
(b) Vertical Orientation
Temperature Difference (°C)
Heat Flux (W·m⁻²)
0
10
20
30
40
50
60
0
100
200
300
400
500
Inclined Exp. Data
Inclined Interrupted Exp. Data
Straight Interrupted Exp. Data
Pin Fins Exp. Data
Inclined Numerical Model
Inclined Interrupted Numerical Model
Straight Interrupted Numerical Model
Pin Fins Numerical Model

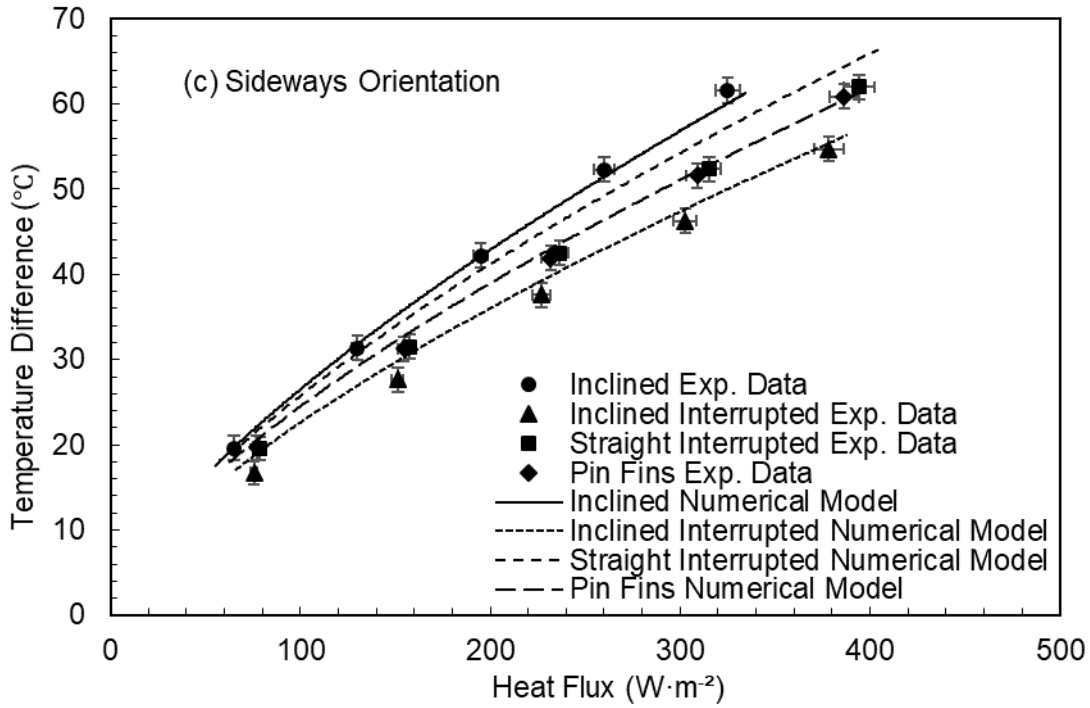

Figure 3.7 Comparison of experimental results (symbols) with numerical models (lines) of untreated heat sinks at three orientations: (a) Horizontal; (b) Vertical; (c) Sideways

Regardless of the surface conditions, all suggested heat sinks including the inclined fins design have their best performance at horizontal orientation while the sideways orientations yield the worst. It is probably because of the spacing between the fins are greatly reduced where less surface area can be in touch with the air-flow and contribute to the convection heat transfer when the heat sink is placed vertically and sideways.

3.5.2. Effect of surface anodization (ε=0.89)

All of our prototyped heat sinks also were anodized by Type II-black treatment, which was mostly adopted for cosmetic purposes. The effect of surface anodization on the thermal performance is shown in Figure 3.8 in contrast to the thermal performance of untreated ones. The horizontal axis denotes the test orientation as well as the surface conditions. The average temperature difference from the heat sink base with respect to the average chamber ambient is chosen as a performance indicator shown on the vertical axis. In all four prototyped heat sinks, a notable improvement can be seen after anodization depending on the fin geometries and test orientations. With horizontal

orientation, the inclined fins design has the most enhancement, approximately 13% in relative temperature difference, while the performance gain for the rest of the fin geometries is less than 8%. In vertical and sideways orientations, all finned heat sinks show between 10% to 15% thermal improvement. In spite of the thermal performance for sideways placed straight interrupted fins and pin fins are greatly improved after the anodization treatment, the average surface temperature difference is still higher than the case where the heat sink is placed vertically. It indicates that radiative heat transfer is insufficient to compensate for the weak natural convection performance caused by the sideways placed fins where it can greatly pose substantial resistances for airflow and heat transfer. The variation of thermal enhancement among different fin geometries and working orientations can also be explained by the fact that thermal radiation is proportional to the surface temperature to the fourth power. Higher surface temperatures will lead to considerable radiative heat transfer.

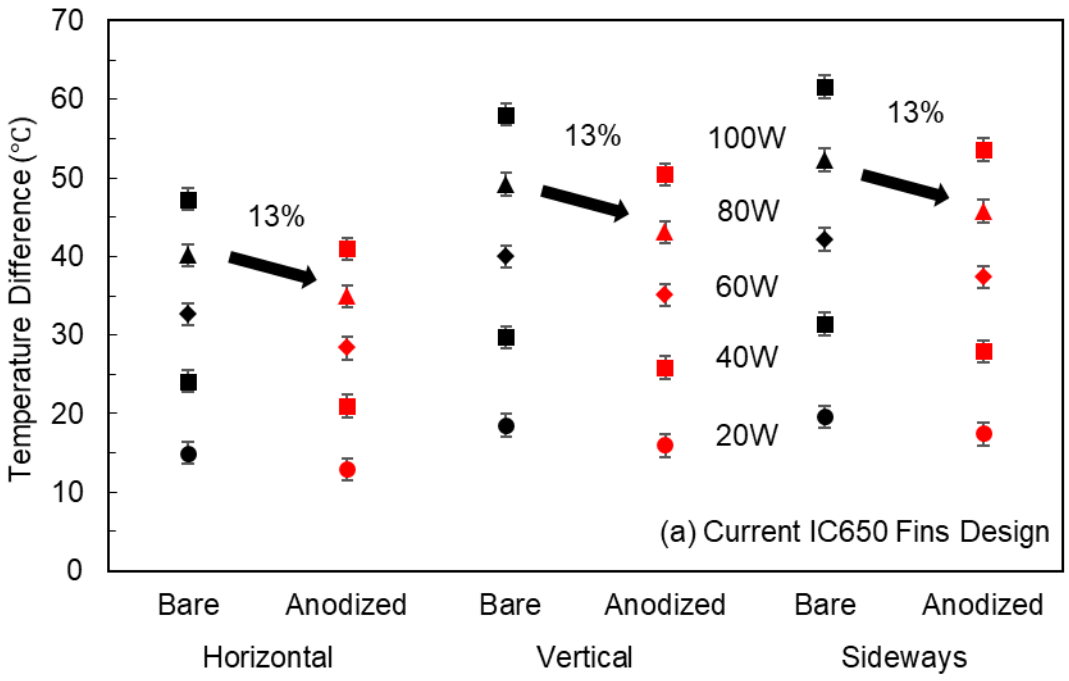

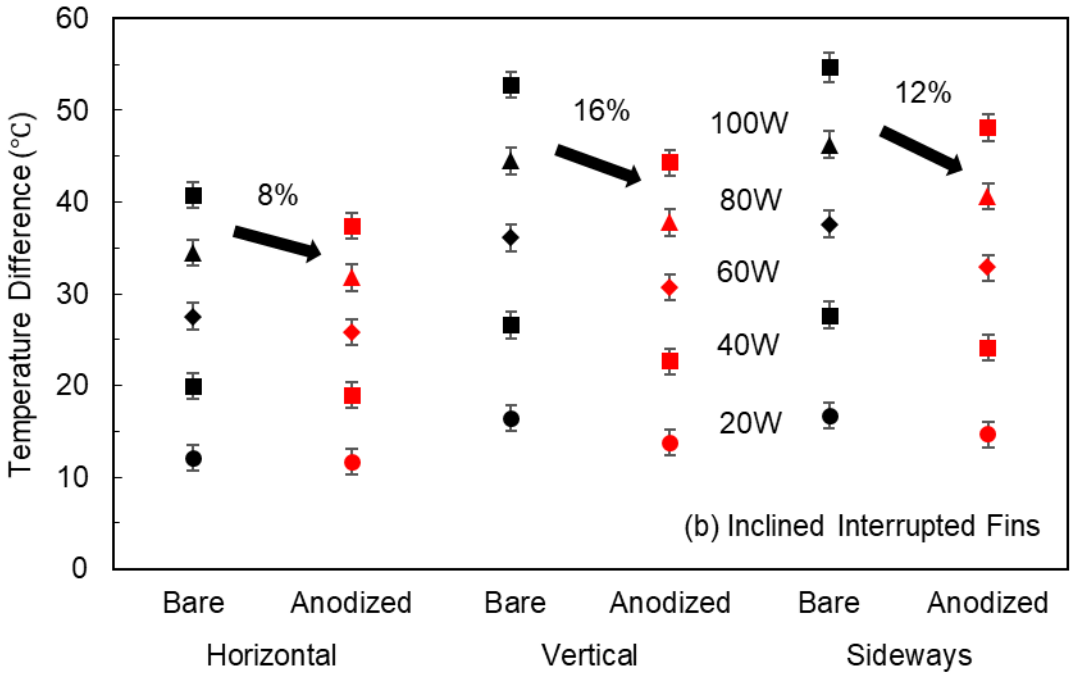
Temperature Difference (°C)
60
50
40
30
20
10
0
8%
16%
12%
100W
80W
60W
40W
20W
(b) Inclined Interrupted Fins
Bare
Anodized
Bare
Anodized
Bare
Anodized
Horizontal
Vertical
Sideways

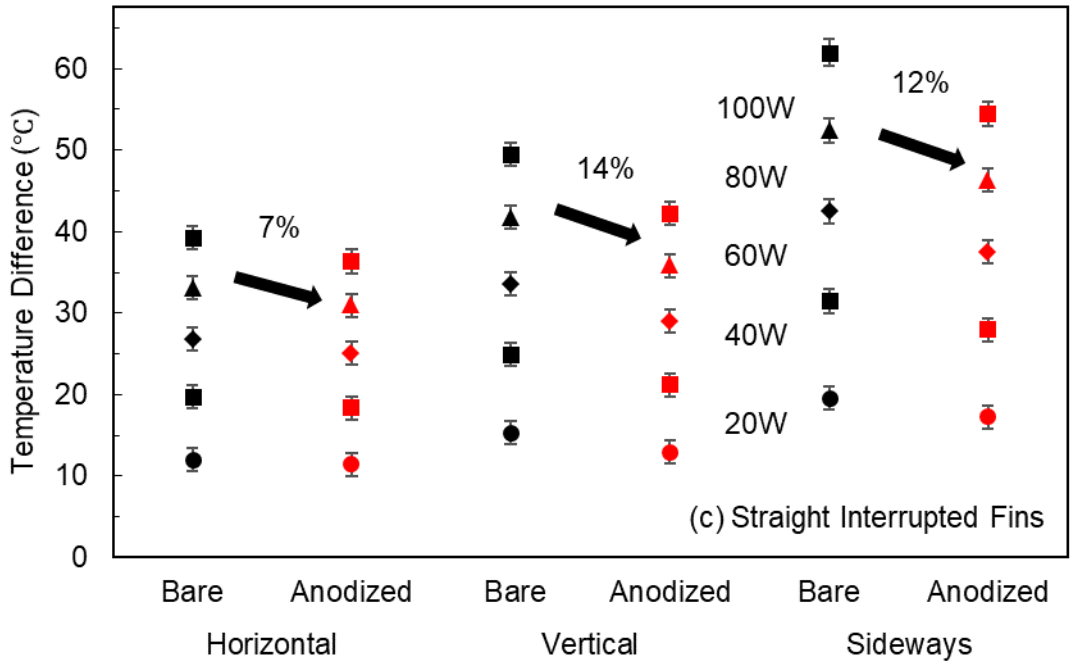
Temperature Difference (°C)
60
50
40
30
20
10
0
7%
14%
12%
100W
80W
60W
40W
20W
(c) Straight Interrupted Fins
Bare
Anodized
Bare
Anodized
Bare
Anodized
Horizontal
Vertical
Sideways

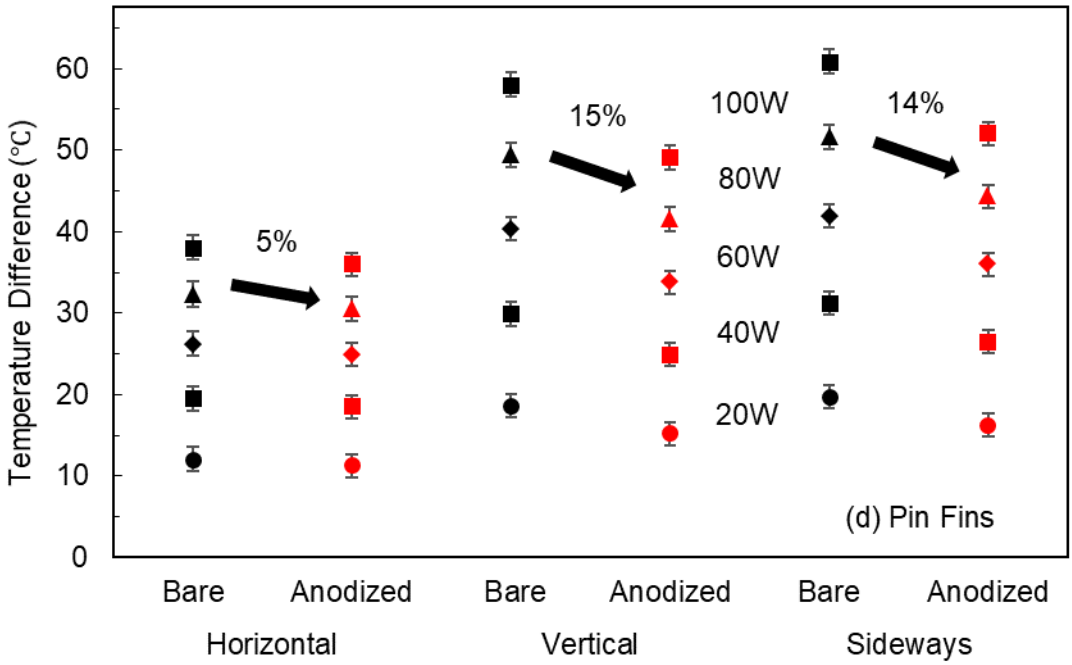

Figure 3.8 Comparison of thermal performance of each prototyped heat sink before and after the anodization at all three orientations: (a) Current IC650 design; (b) Inclined interrupted fins; (c) Straight interrupted fins; (d) Pin fins

In the meantime, the comparison among each anodized heat sinks reveals the identical enhancement to the inclined fins design without surface anodization treatment as it can be seen from Figure 3.9. At horizontal orientations, the inclined interrupted fins, straight interrupted fins, and pin fins have thermal improvement of 9%, 11%, and 12%. The relative enhancement is 9% and 15% for inclined and straight interrupted fins where the pin fins have the same performance as the inclined design at the vertical orientation. At sideways orientation, only the anodized inclined interrupted design can yield around 10% relative improvement to the anodized benchmark heat sink. This further indicates its versatility to operate at all three orientations.

Figure 3.9 also shows the validation of the present numerical model against collected experimental data. As can be seen in Figure 3.9 (a) to (c), the numerical model predicts the performance of each heat sink, considering both natural convective and radiation heat transfer. The maximum difference of the numerical model from experimental results is 8%, 5% and 4% for horizontal, vertical and sideways orientations, respectively, which is within the range of measurements uncertainty. The present numerical model also

enables us to calculate the contribution of radiation heat transfer and deconvolute it from the overall heat dissipation to further investigate anodization effect.

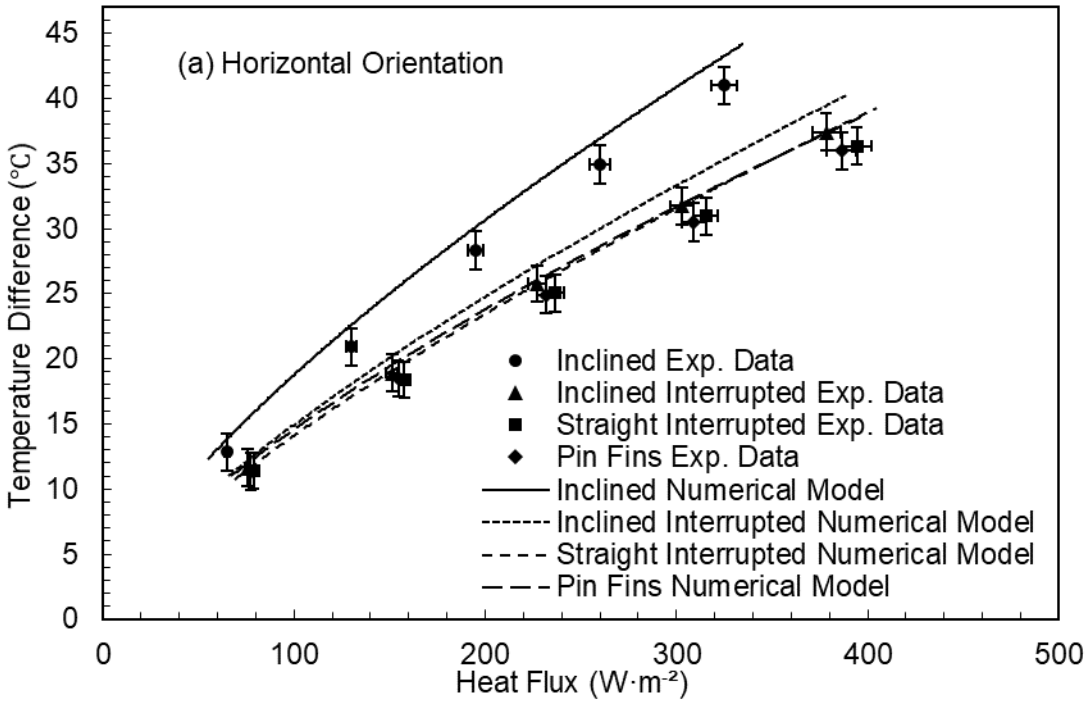

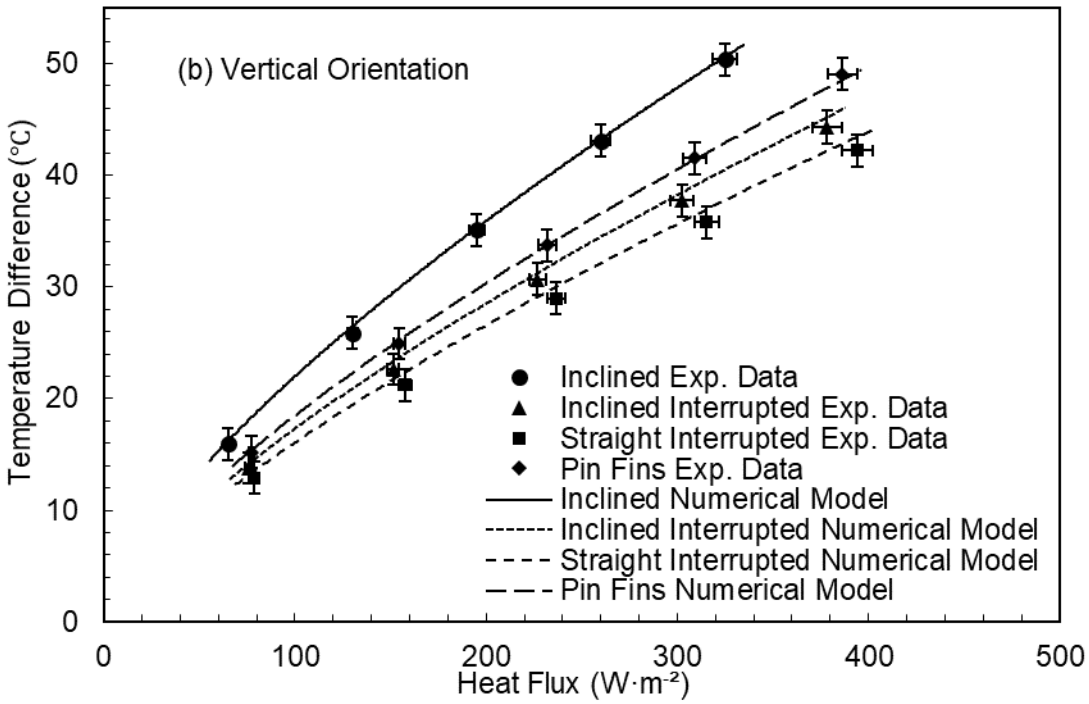

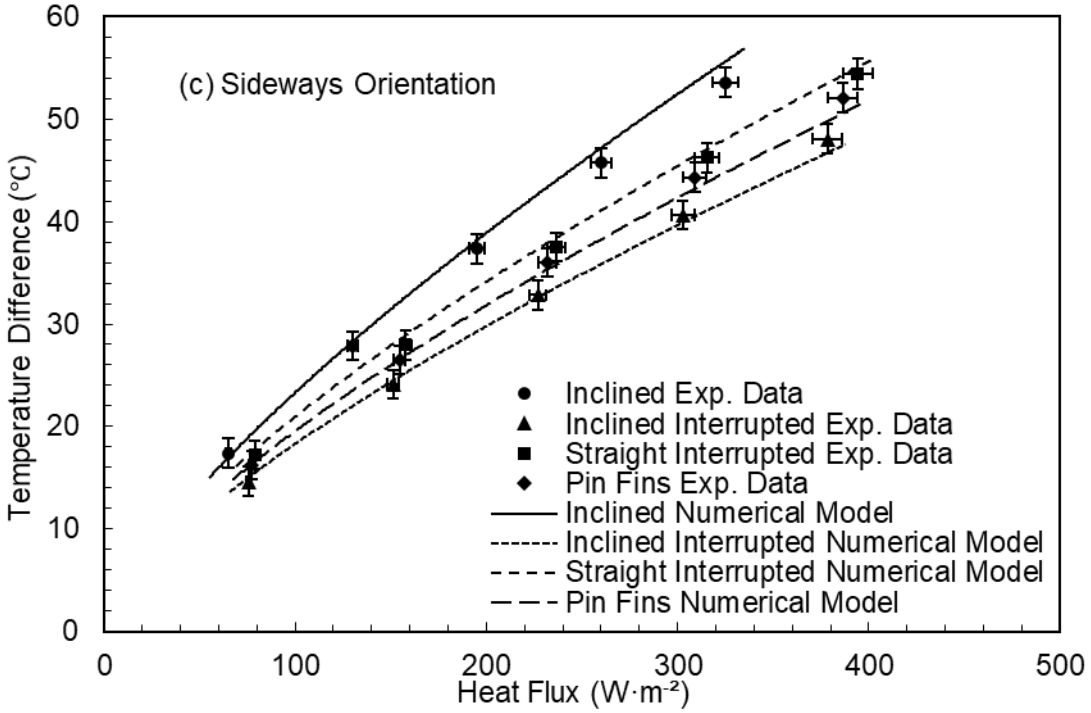

Figure 3.9 Comparison of experimental results (symbols) with numerical models (lines) of anodized heat sinks at three orientations: (a) Horizontal; (b) Vertical; (c) Sideways

Figure 3.10 shows the contribution of thermal radiation from each anodized heat sinks. The results are calculated from the numerical model after validation by experimental results. The curves represent the portions of the thermal radiation to the overall heat dissipation decoupled from the validated numerical model. As shown, the significance of radiative heat transfer depends on the fin geometries and working orientations. The contribution of radiative heat transfer varies between 20% to 27% for horizontal orientation while the range can expand to 22% to 32% and 25% to 35% for vertical and sideways orientations. This rising trend may be attributed to the relatively high surface temperature and lead by the fact the natural convective heat transfer is minimized when heat sinks are placed at vertical and sideways orientation. It is also observed that the relative contribution of the thermal radiation to the convection decreases with respect to the higher thermal input. The explanation lies in the fact that the driving force for the natural convection is greatly improved due to the higher temperature difference (temperature gradient) as the heat source power increase. The relative significance of thermal radiation can be mitigated despite the absolute share of radiation is rising. From the perspective of comparing the relative amount of radiation from each tested heat sink, the inclined interrupted fins and pin fins have the same rate of radiation heat transfer while the straight interrupted fins

yield the lowest when placed horizontally. At vertical orientation, the straight interrupted fins still have the lowermost radiation off the surface due to the excellent performance of natural convection. However, the inclined interrupted fins have the least amount of radiation at sideways orientations attributed to the versatility to operate which showed as to have the lowest surface temperature. The inclined fins, the straight interrupted fins, and the pin fins have almost the same contribution of thermal radiation in case of overall heat transfer at sideways orientation.

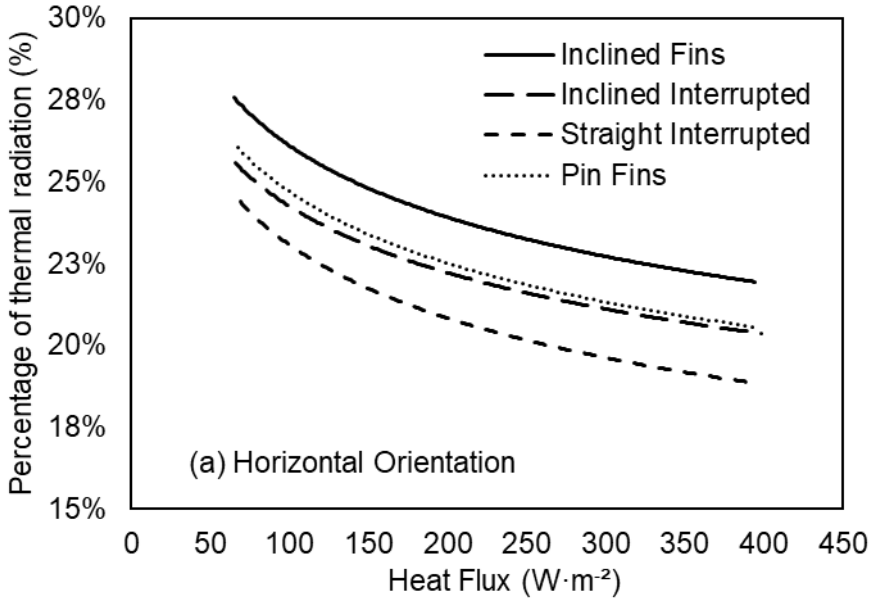

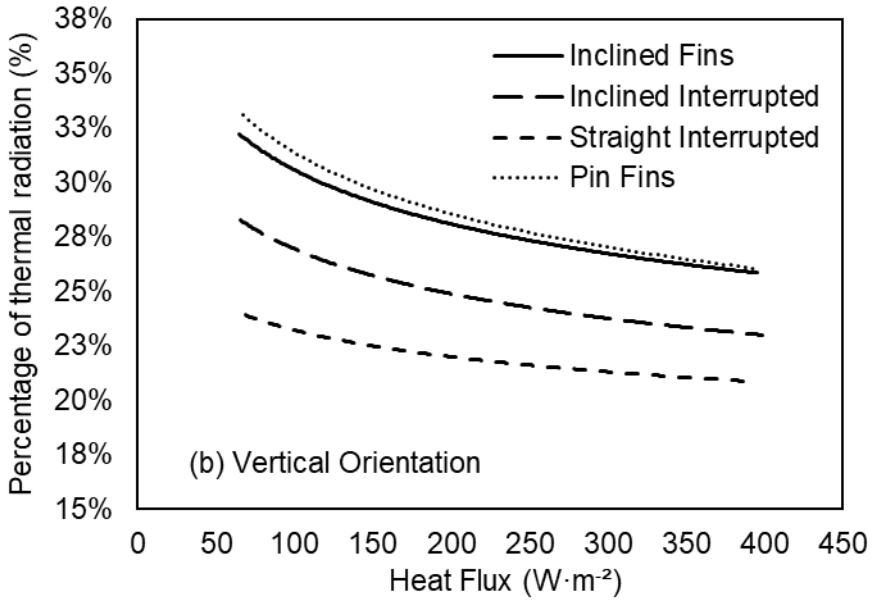

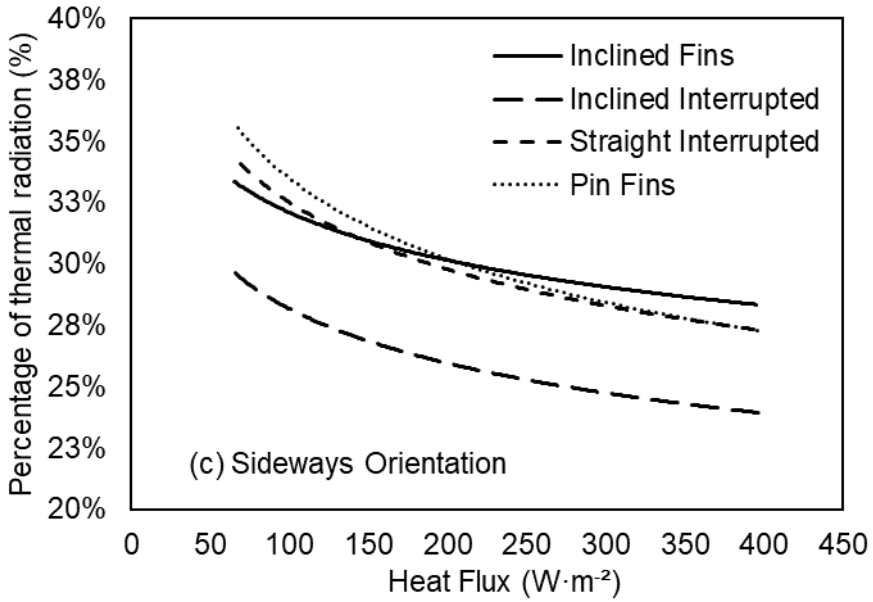

Figure 3.10 Percentage of thermal radiative heat transfer in overall heat dissipation from various fin geometries at three orientations: (a) Horizontal; (b) Vertical; (c) Sideways

In all, the proportion of thermal radiation from various finned heat sink varies between 20% to 35% depending on several factors including fin geometries, surface area, test orientations, and surface emissivity. Therefore, the effect of anodization on the overall thermal performance of above-prototyped heat sinks is substantial and should be utilized to improve the overall heat removal capacity of naturally cooled heat sinks (NCHx).

3.6. Conclusion

In this chapter, Natural convection and thermal radiation from battery charger heat sinks, with identical footprints, with various fin geometries were investigated through a series of experimental and numerical studies to improve the thermal design of a battery charger. The proposed fin geometries, including inclined interrupted fins, straight interrupted fins, and pin fins showed a notable thermal improvement in comparison with the inclined fins design, which resembles the existing thermal performance of the current battery charger (IC650) design and it served as the benchmark case. After anodization, the overall heat removal capacity of each prototyped heat sink was improved due to the increase of surface thermal emissivity. The major findings of this chapter can be concluded as:

1). An enhancement of 20% can be gained by adopting the pin fin design at horizontal orientation, however, the improvement was less prominent for vertical and sideways orientations in case of surface emissivity of 0.03.

2). The bare straight interrupted fins can lead to a 15% reduction in average heat sink base temperature difference for vertical orientation while only 5% is noticed for the sideways orientation.

3). The inclined interrupted fins had the versatility to operate at all three orientations where the improvement of 14%, 9%, and 11% was achieved before anodization.

4). A 5% to 16% additional reduction in temperature difference was observed compared to each untreated heat sink based on fin geometries and test orientations through anodization treatment.

5). Considering both the effects of fin geometries and anodization, compared to the inclined fins without surface anodization (benchmark case), the maximal overall improvement, 27%, was gained in vertically placed straight interrupted fins.

6). The overall enhancement for inclined interrupted fins, the most versatile and promising fin geometry for the future applications, was 21%, 24%, and 22%, respectively.

.

Chapter 4.

Thermal performance and parametric study of the Inclined interrupted finned heat sink

Comparison of thermal performance between various finned heat sink from Chapter 3 shows the potential to gain identical improvement at all three orientations for inclined interrupted fins. It outperforms the straight interrupted fins and pins fins where the former is able to bring the most improvement at vertical orientation, and the latter performs the best at horizontal orientation. Thus, a further study of the versatility to operate at various orientations and effect of the geometrical parameter in inclined interrupted fins is performed and presented in this chapter. A modified experimental testbed developed from previous studies is used to conduct the thermal test. A numerical model developed in Ansys Fluent 17.2 validated by experimental results is adopted to conduct the investigation of the impact of geometrical parameters, i.e., fin spacing, inclined angle, fin length as well as column distance. An additional inclined interrupted finned heat sink with eight columns of fins is prototyped with CNC machining at Machining Shop located in the School of Mechatronic Systems Engineering, Simon Fraser University. The results reveal an optimal value for fin spacing and column distance. However, the effect of inclined angle and fin length on the overall thermal performance is highly coupled and the selection of detailed dimensions should be based on the applications and targeted heat transfer capability.

4.1. Problem statement

Figure 4.1 shows the schematic of the inclined interrupted fins. In this parametric study, we chose to focus on the spacing (S), width (W_{fin}), inclined angle (θ) of the fin and the column distance (l) because of their profound thermal influence. By varying these geometrical dimensions, a competing tend shows between the overall heat dissipating area and heat transfer coefficient. The larger fin spacing can greatly minimize the heat dissipating area but it allows for more airflow that results in the higher heat transfer rate per unit area and vice versa. An optimal combination for the geometrical size of the inclined interrupted fin should exist in terms of heat removal capability. At the same time,

the effect of orientations is also taking into account where our focuses are not only placing on the horizontal yet the vertical and sideways orientations.

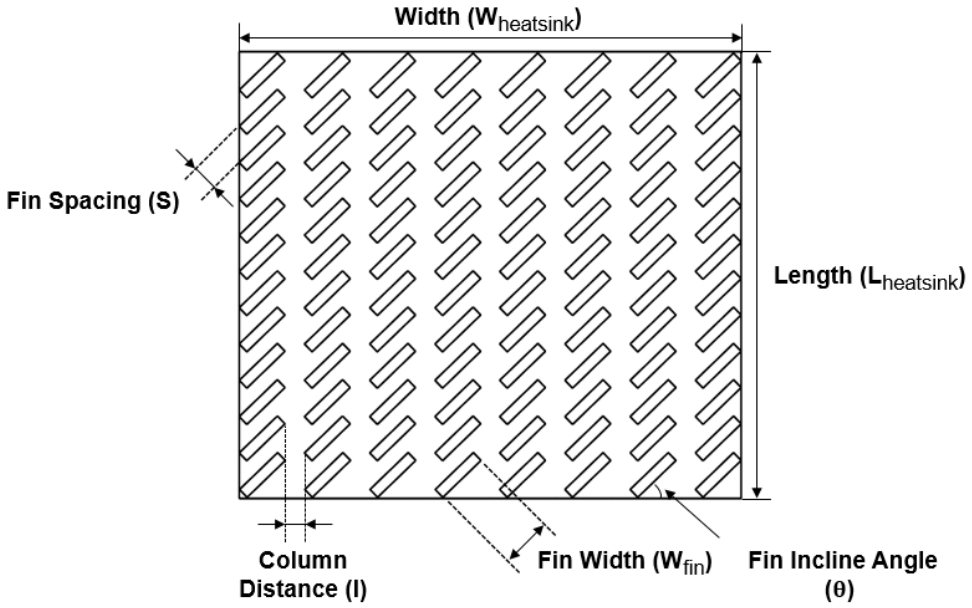

Figure 4.1 Schematic of heat sink comprised with inclined interrupted fins

4.2. Methodology

The approach follows the manner of varying one parameter at a time and maintains the rest of dimensions unchanged rather the traditional Design of Experiments (DOE) approach where the input parameters are tuned in a combination with different levels for two reasons. Firstly, the control variables are highly dependent on each other in which a change of dimension in one parameter pose constraints for the associated ones. Secondly, the level of each factor (or variables) are different and some can have as much as 15 or 20 levels where the huge amount of time and computational resources are required.

A newly developed numerical model has been used to investigate the thermal performance of the various interrupted finned heat sink in Ansys Fluent 17.2. The numerical model has been validated with the experimental results of the inclined interrupted finned heat sink that manufactured from the previous study. An additional inclined interrupted heat sink was prototyped and manufactured with a choice of desired (optimal) geometrical dimensions based on the acquired results from the numerical parametric study. The validity of the parametric study from numerical results was further confirmed by the experimental test of this newly prototyped heat sink. The control

variables are the fin spacing (*S*) which was dictated by the number of fins in each column, the inclined angle (*θ*), the fin width (*W*) which is dependent on the inclined angle, and the column distance (*I*). The performance indicators or the output parameters was the average surface and base temperature. The exact dimensions of each geometrical parameter were calculated and assigned to the Ansys Fluent by a simple code written in Matlab. The constraints or the interactions between each dimension can be correlated as:

$$(n-1)\frac{P}{cos\theta} + W_{fin} \cdot sin\theta + t \cdot cos\theta = L_{heatsink} \tag{4.1}$$

$$N\left(W_{fin} \cdot sin\theta + t \cdot sin\theta\right) + (N-1)I = W_{heatsink} \tag{4.2}$$

Where *n* and *N* stand for the number of fins in each column and the number of columns and *t* is the fin thickness. The *H* and *L* is the length and width of the heat sink which is 16cm and 18cm respectively. Only the case where *N* equals eight and the fin thickness of 0.39 at the bottom was explored in this context and future efforts can be considered in terms of the potential thermal improvement. A draft angle of 1° has also been imposed on the fins to emphasize the thermal influence by the limitation of manufacturability. The height of fins and base remains the same as 6cm and 0.35cm as the previous approach and bears the same heat sink footprint.

4.2.1. Heat sink prototyping

The heat sinks prepared in this study have the same footprints as the existing IC650 heat sink from Delta-Q Technologies. They were prototyped by CNC machining tools in School of Mechatronic Systems Engineering, Simon Fraser University. Aluminum alloy 6061-T6 was used in the process of prototyping with its thermal conductivity of 150 $W \cdot m^{-1} \cdot K^{-1}$]. The base size of the heat sinks was 18cm×16cm with fin height of 6cm. The base height was 0.35cm. A draft angle of 1° was imposed to mimic the actual fins manufactured from the die-cast process that may affect the overall heat transfer rate.

4.3. Numerical analysis

The present numerical approach shares the same computational domain as the previous model. The discretization scheme and solution algorithm are consistent with the aforementioned approaches. The laminar model for fluid flow and surface to surface [S2S]

radiation model was used. The Boussinesq assumption was applied to the air density as a function of temperature. The major difference from the previously developed numerical model is the boundary conditions prescribed on the fluid domain wall where the solid wall boundary conditions have been replaced by the pressure outlets with the ambient static pressure and temperature (22℃). This enables the fast convergence showing as the mass balance in the systems. The Under-Relaxation Factors (URF) has been adjusted to 0.6 in momentum terms instead of 0.3. All the walls have the non-slip and no penetration boundary conditions. For the frontal heat sink surfaces (solid-fluid interfaces), the boundary conditions were determined via system couplings. Constant heat flux was assumed at the back of the heat sink as the thermal input. The surface thermal emissivity for the heat sink and computational domain walls are 0.03 and 0.9. The schematic of the numerical domain and thermal input shows in Figure 4.2. The simulations were considered as converged when all the temperature variation within the past 100 steps fall into the range of 1×10^{-4}. The convergence criteria for radiosity residual is 1×10^{-3}.

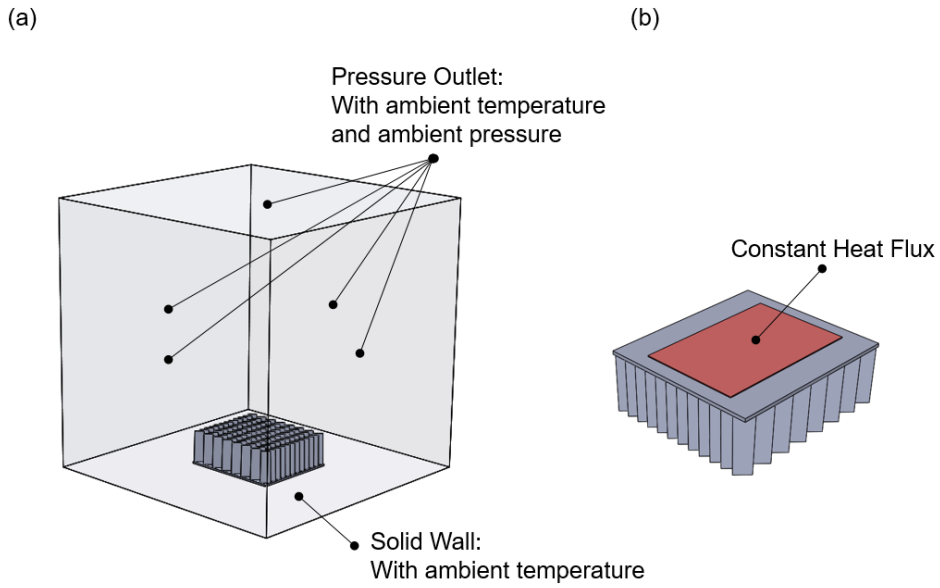

Figure 4.2 Schematic of computational domain: (a) Computational domain; (b) Thermal input at the heat sink base

Figure 4.3 shows the results of mesh independency study where the average heat sink surface temperature difference to the ambient are varying with reference to the number of meshing elements. The mesh independence study is done by selecting the inclined interrupted design with 12 fins in each column with a thermal input of 80W and thermal emissivity 0.89. As shown, the temperature difference slightly increases from

36.58 to 36.6, a 0.2% variation, when the meshing element expands from 6,202,176 to 6,810,448. It shows that the reduction of the meshing size has a limited improvement in results accuracy where more computational resources are required. Thus, a chose of meshing size on the heat sink surface is 1.5×10^{-3} and 1.2×10^{-2} for the chamber volumes where the number of mesh elements is around 6,202,176.

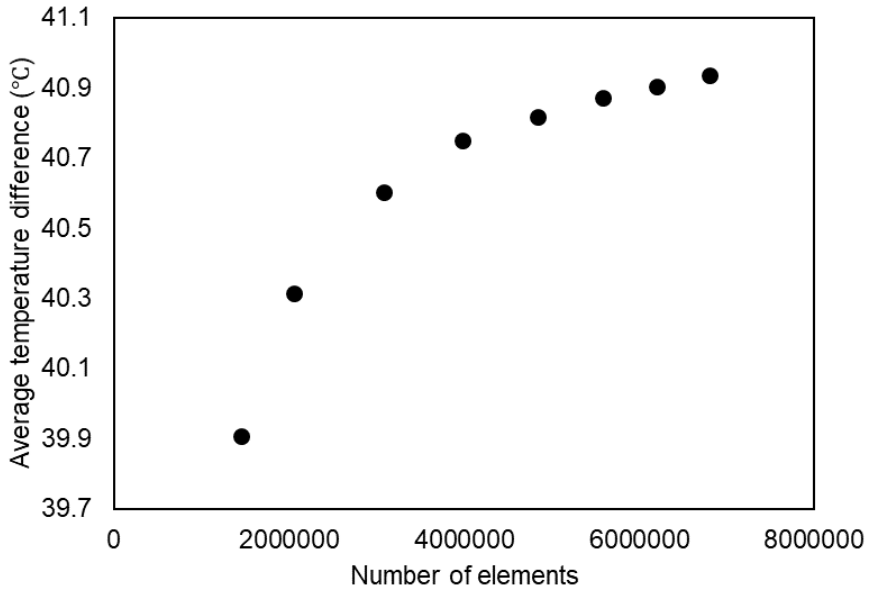

Figure 4.3 Mesh independency study of inclined interrupted fins, 12 fins in each column

4.4. Experimental setup

The testbed comprised of a structure of wooden plate [1cm], Plexiglas foam [2cm], and wooden plate [1cm] to provide sufficient thermal insulation. An electrically insulated Kapton heater of size 10cm × 15cm was applied at the back of the heat sink providing the thermal inputs to the system. The thermally conductive paste was placed between the heat sink base and heat source in order to minimize the thermal contact resistance (TCR). The temperature [NI-9212] and voltage [NI-9229] acquisition modules from National Instruments were employed to monitor the temperature distribution along the heat sink base and actual thermal input. The Chroma programmable DC power supply [62012P-100-50] was used to provide the electrical power to the system. Eight T-type thermocouples were installed at the heat sink base and an additional one were placed in the adjacent surrounding to record the ambient temperature. The schematic of the testbed and the locations of thermocouples are provided in Figure 4.4.

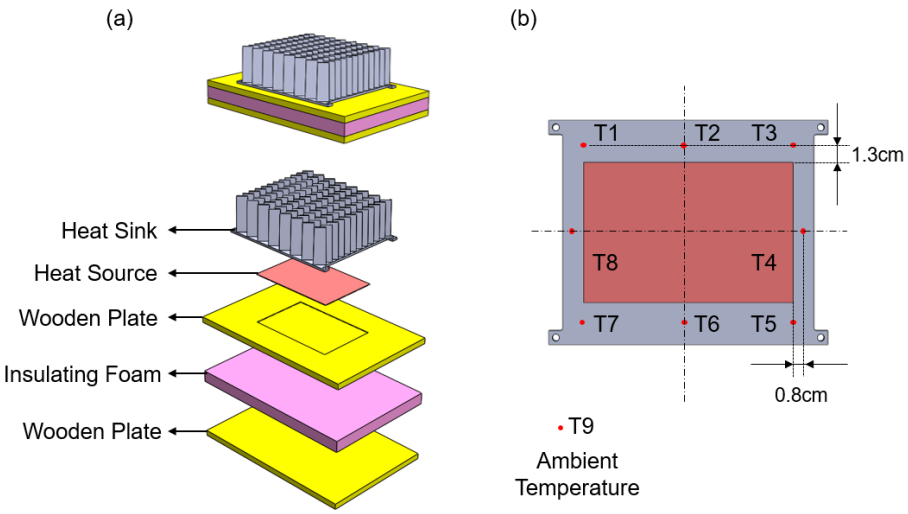

Figure 4.4 Schematic of experimental setup: (a) Testbed; (b) Location of the thermocouples

The thermal tests were performed in the open lab environment and the room temperature remain at 22℃. Each heat sink test repeated at least three times with thermal inputs varied from 20W to 100W at all three orientations, i.e., horizontal, vertical and sideways. The steady-state condition was reached when the partial difference of the temperature is less than 0.001 for 30mins. Three various test orientations are similar to the schematic showed in Figure 3.4 Test orientations: (a) Horizontal; (b) Vertical; (c) Sideways in Chapter 3.

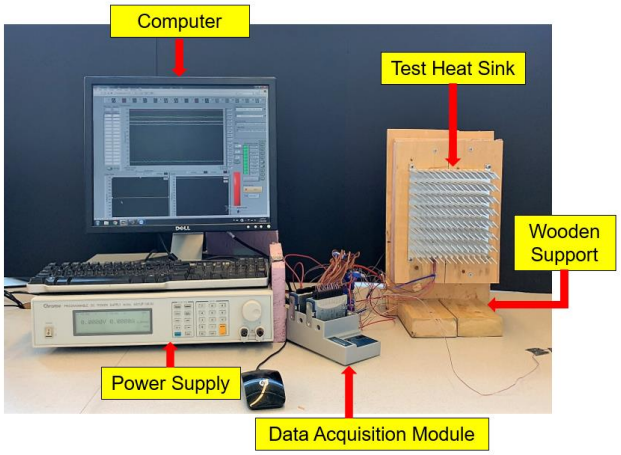

Figure 4.5 Experimental setup for heat sink test in ambient with sideways placed inclined interrupted fins shown in figure

The maximum error for T-type thermocouples we used is ±1℃ and the maximal error for voltage sensor ±1.2%. As calculated, the maximum uncertainty for thermal power input is ±1.7%. The error range for temperature difference is ±1.4℃ with the corresponding standard deviation of measured data. The detailed uncertainty propagation can be found in Section 2.4.2, Chapter 2.

4.5. Results and discussion

During the parametric study, the thermal input of the heat source remains at 80W which is similar to the heat generation rate in IC650 battery charger. This study investigates the impact of geometrical parameters in a less ideal case where further efforts are needed and may continue to provide a profound understanding of heat transfer behavior for future applications.

4.5.1. Numerical model validation

Figure 4.6 shows the comparison of experimental test data and numerical solution of the same heat sink with inclined interrupted fins from Chapter 3, where each column consists of 12 fins. The solid symbols represent the experimental data, and the numerical results exhibit as the solid and dash lines. A good agreement can be observed where the maximal deviation of numerical solutions from experimental results are 5%, 1%, and 6% at horizontal, vertical, and sideways orientation. The results showed in Figure 4.6 further unveil that the versatility of the inclined interrupted fins showing as identical thermal performance at both vertical and sideways orientations.

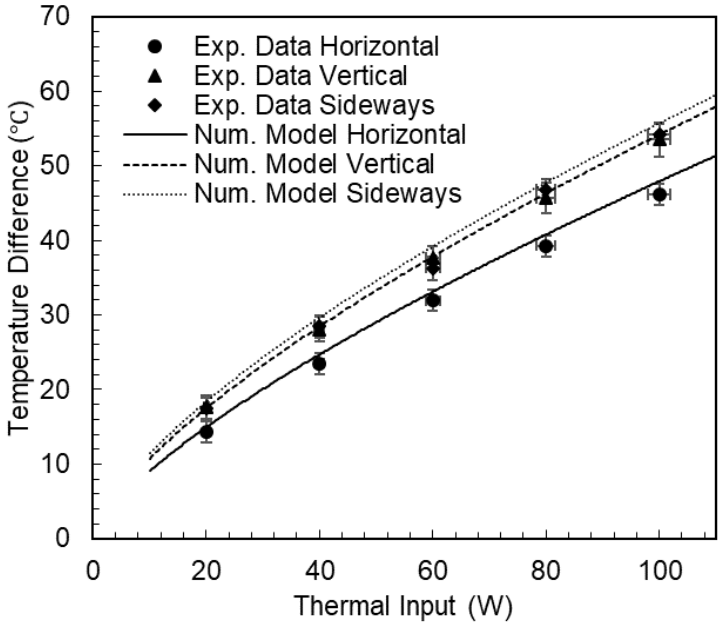

Figure 4.6 Comparison between the experimental data (solid symbols) and numerical model (lines) of inclined interrupted fins (fin number of 12 in each column)

4.5.2. Effect of fin spacing

Fin spacing represented in this context includes the clear distance between adjacent surfaces and fin thickness. The results for parametric study are acquired with the constant thermal input of 80W and surface emissivity of 0.03. The fin inclined angle was maintained as 44º and the column distance was 0.7cm. The fin width was also kept unchanged through the simulations as 1.9cm. As seen in Figure 4.7, an optimal value existed for all three orientations with minor offsets. The temperature difference denotes the variation between the average heat sink base and ambient temperature. Regardless of the working orientations, the average heat sink base temperature will have an acute drop as fin spacing increases where the fin number reduces. This is the phase where air-flow is greatly obstructed and the heat transfer coefficient is considerately minimized. Subsequently, the temperature difference reaches the lowest which is considered to be the balance joint between two competing trends between surface area (*A*) and heat transfer coefficient (*h*). Then the temperature difference gradually increases because of the losses in the overall heat dissipating area with an increment of the spacing distance. As can be seen in Figure 4.7, the optimal fin spacing for all three orientations are in the same range but differs slightly. The optimal value for horizontal and vertical orientation is

approximately 0.8cm compared with sideways orientations, which equals to nearly 0.95cm. This may have an implication that more resistance for air-flow and heat transfer are imposed when heat sinks placed sideways and relative larger fin spacing is required to balance the surface area. This finding is consistent with the thermal test results presented in the previous chapter.

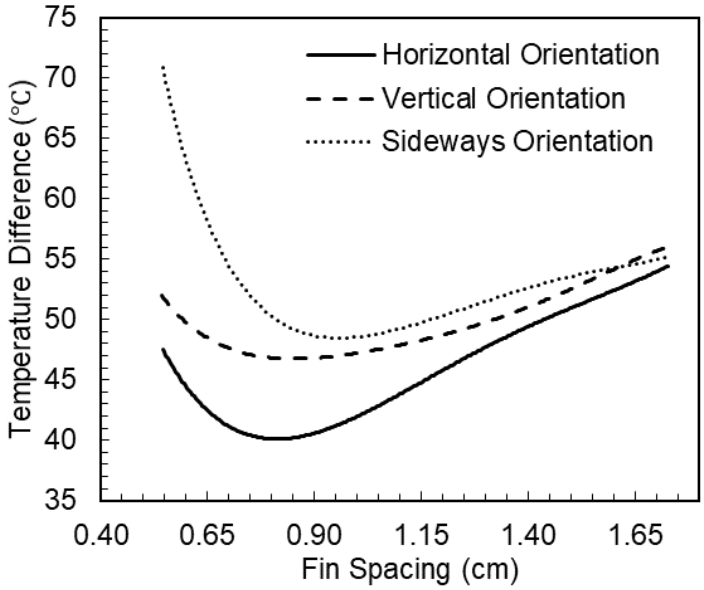

Figure 4.7 Effect of fin spacing on the average heat sink base temperature with a thermal input of 80W

4.5.3. Effect of fin inclined angle

Figure 4.8 shows the trend of varying fin width induced by the alternation of fin inclined angle. The fin width can be seen as a dependent parameter based on the fin inclined angle. As the fin inclination increases, the width of the fin is enlarged with the trend of reduction in fin numbers. As the fin inclined angles increasing, the shorter fins are replaced by the long fins in a manner of relatively small quantity. Figure 4.9 shows the effect of the inclined angle on the average heat sink base temperature with reference to the ambient temperature. As the fin inclined angle increasing, the average heat sink base temperature difference is increasing at horizontal and sideways orientation due to the fact the long fins minimize the effect of interruption that less air-flow is able to sweep through the heat dissipating surfaces. However, the thermal performance is greatly improved at vertical orientation as the inclined angle increases because this allows more air-flow passing through the inter-region between fins. At sideways orientation, the inclined

interrupted fins behave much resembling to the straight interrupted fins where the fins are nearly orthogonal to the direction of gravity as inclination increases. This leads to severely impediment to all air-flow and minimizes the heat rejection capability. In all, several conclusions can be drawn from Figure 4.9: i) the thermal performance of inclined interrupted fins is highly dependent on the fin inclined angles, especially at vertical and sideways orientation; ii) it should also be noted that the chosen of the fin inclination requires consideration and evaluation of several factors including dominant working orientation and desired heat dissipation capacity.

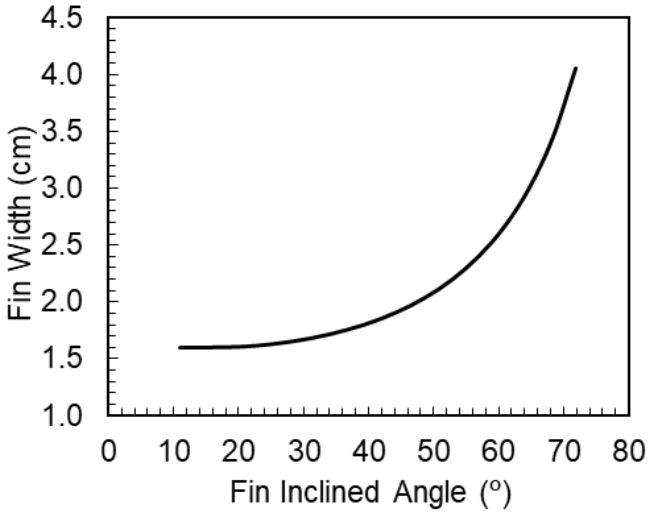

Figure 4.8 Effect of fin inclined angle on the fin width

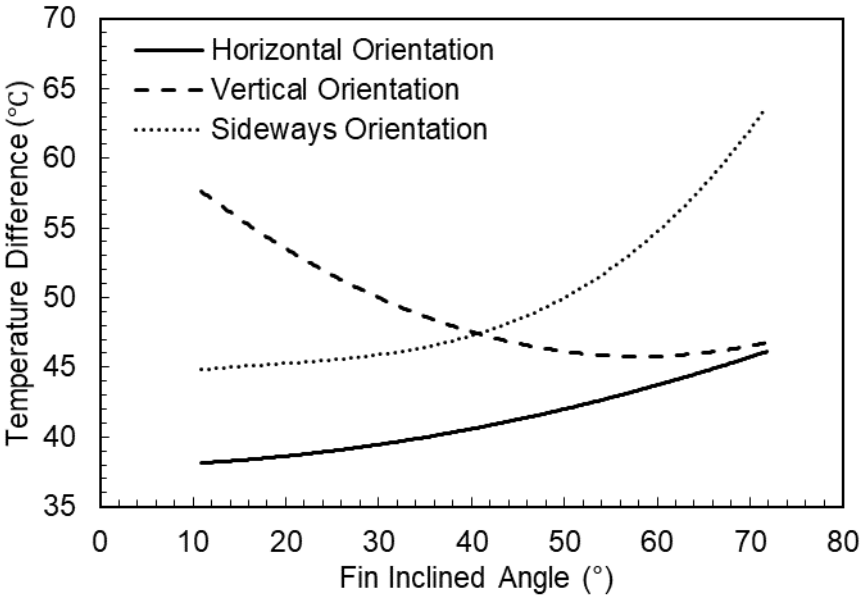

Figure 4.9 Effect of fin inclined angle on the average heat sink base temperature with a thermal input of 80W

4.5.4. Effect of column distance

Figure 4.10 indicates the linearly varying trend of fin spacing and width with column distance. Because of the predetermined heat sink footprint, i.e., base size, it is challenging to maintain these geometrical dimensions unchanged. As shown, both fin spacing and width vary linearly with reference to the column distance where the former is increasing in a small range while the latter decreases from almost 3cm to 1cm. The variation in these parameters can be attributed to the fixed fin inclination which is 44° in all simulations.

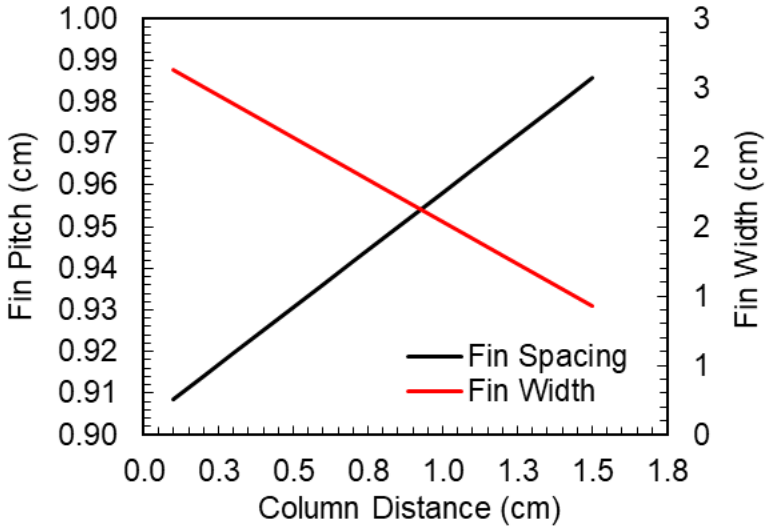

Figure 4.10 The varying fin spacing and fin width with regard to the column distance

Figure 4.11 shows the effect of the column distance on the overall thermal performance indicated as the average heat sink base temperature difference in respect to the ambient. It clearly shows that an optimal dimension for all three orientations presented in currently inclined interrupted fins design. As the column distance increases, the average heat sink temperature difference begins to reduce and then reach the optimal point where the products of surface area and heat transfer coefficient is maximal. When the column distance continues increasing, the increment in heat transfer coefficient is not enough to compensate for the area loss in heat dissipating fins which result in the rising tendency in average heat sink temperature difference, showing in Figure 4.11. In short, the optimal sizing is approximately 0.5cm, 0.9cm, and 0.6cm for horizontal, vertical, and sideways orientations. Nevertheless, the chosen of the dimension should also consider the manufacturing capability, availability, and cost where this parametric investigation merely offers as a reference.

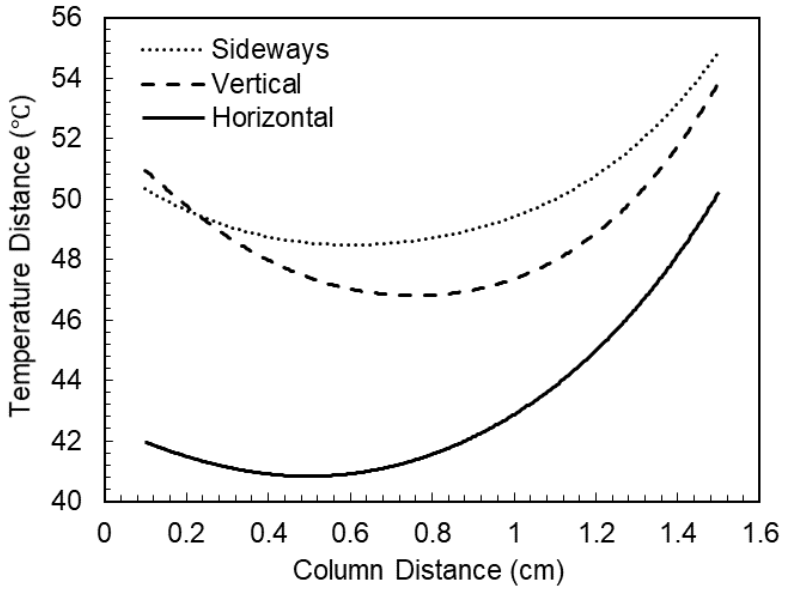

Figure 4.11 Effect of column distance on the average heat sink base temperature with a thermal input of 80W

4.5.5. Validation of parametric results

An additional heat sink was manufacture to verify the results from the parametric study and also further validate the numerical model. The dimension of this newly built heat sink refers to the optimal size of fin spacing for horizontal orientation acquired in this parametric study. The fin number in each column is maintained at 14, and the face to face spacing distance is 0.8cm. The detailed dimensions of this newly built heat sink are showing in Figure 4.12.

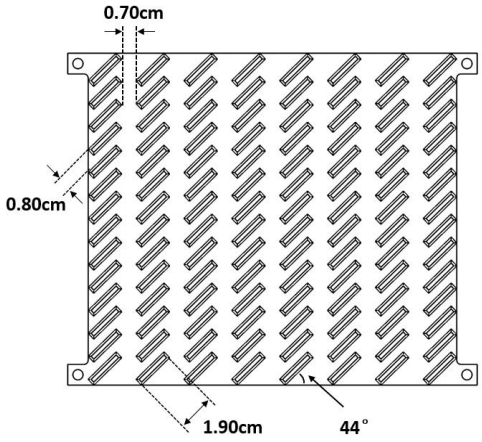

Figure 4.12 Schematic of inclined interrupted fins design with optimal fin spacing for horizontal orientation

Figure 4.13 shows the comparison between the experimental data and numerical model. The temperature difference denotes the variation between the heat sink base temperature to the ambient. The results reveal a maximum 6% difference of numerical model to the experimental data which happened at horizontal and sideways orientations. In vertical orientation, the numerical results only deviate 4% from the experimental data. This further indicates that the parametrical results along with the numerical model are valid and can be used as references.

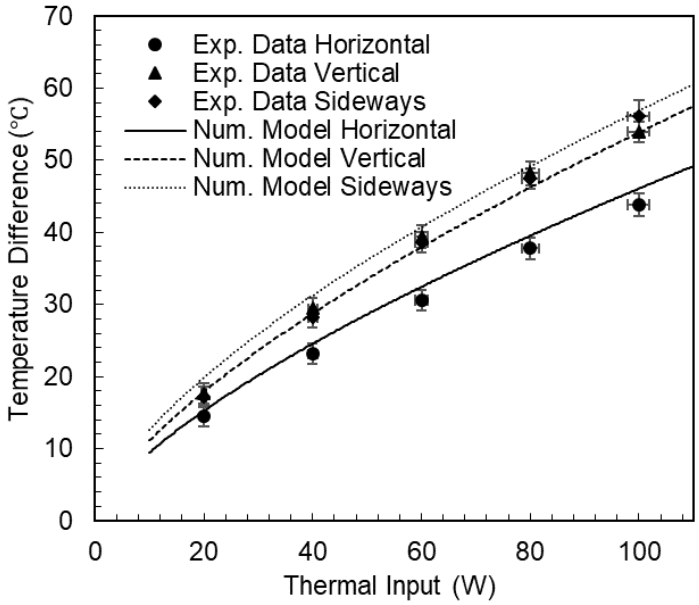

Figure 4.13 Comparison between the experimental data (solid symbols) and numerical model (lines) of inclined interrupted fins (fin number of 14 in each column)

4.6. Conclusion

In this chapter, the effect of various geometrical parameter on the thermal performance of inclined interrupted fins was carried out by a systematic numerical approach. The case with fixed column number [$N = 8$] and steady thermal input [80W] was considered. The numerical model used for the parametric study was validated by the experimental data with respect to the two prototyped heat sinks. The results show optimal values existed for the fin spacing and column distance at all three orientations. However, the chosen of the fin inclined angle highly depends on the dominant working orientation and desired heat transfer capability where no universal optimal value can be obtained.

Chapter 5.

Conclusions

5.1. Summary of thesis

This thesis explored the improvement of the heat removal capacity in naturally cooled power electronics heat sinks from two perspectives, including improvement in the thermal radiation by surface anodization and enhancement of natural convection by alternating the heat sink fin geometries. The parametric study of the inclined interrupted fins was also carried out and attempt at finding the optimal geometrical dimension for various heat sink working orientations. The combined effect of surface emissivity and fin geometries showed a promising enhancement in case of overall thermal performance. The following summarized the major findings and contributions in each chapter.

The thermal impact of surface emissivity was investigated in chapter 2. The surface emissivity of bare and anodized die-cast A380 and machined 6061 samples were determined. The thermal performance of the anodized die-cast battery charger heat sink was tested in a custom-built experimental setup, and a numerical model was developed as an effort to further understand the thermal radiative heat transfer in such heat sink. The results showed that anodization could significantly improve the surface emissivity, up to 0.92 where leads to maximal 15% reduction in thermal resistance. It also observed that thermal radiation could contribute up 41% to the total heat dissipation.

Chapter 3 compared the thermal performance of various fin geometries for natural convection and thermal radiation. The proposed finned heat sinks with inclined interrupted fins, straight interrupted fins, and pin fins were tested at all three orientations, and a notable improvement to the benchmark case was observed. The results also revealed that the inclined interrupted fins had the versatility to operate at all three orientations where the overall thermal improvement is 21%, 24% and 22% with the help of surface anodization.

The last part focused on the parametric study in the inclined interrupted fins with a validated numerical model developed in the previous efforts. The results showed an optimal dimension for fin spacing and column distance for all orientation while no universal optimal value can be observed for fin inclined angle.

5.2. Future works

The future work, as a continuation of the current study, can be categorized into some of the following items:

- The further efforts can be placed in pursuit of controlling and perfecting the procedure of anodization from the perspective of surface cosmetic value and may look into any other potential surface treatment methods, e.g., powder coating, spray painting, and e-coating;
- Explore the heat sink manufacturing technologies with low cost, especially to reduce the thickness of the fins, eliminate the restriction of face to face spacing, as well as the ejector pin posts and draft angles which all limits the overall thermal performance;
- Extend parametric studies of inclined interrupted fins with new geometrical parameters, such as column number [Figure 5.1], heat sink size, and explore new scenarios including varying the thermal inputs;
- Extend the steady-state thermal analysis of each finned heat sink to transient behavior with varied thermal loads;
- Investigate and compare the effect of thermal storage material with various novel fin geometries;

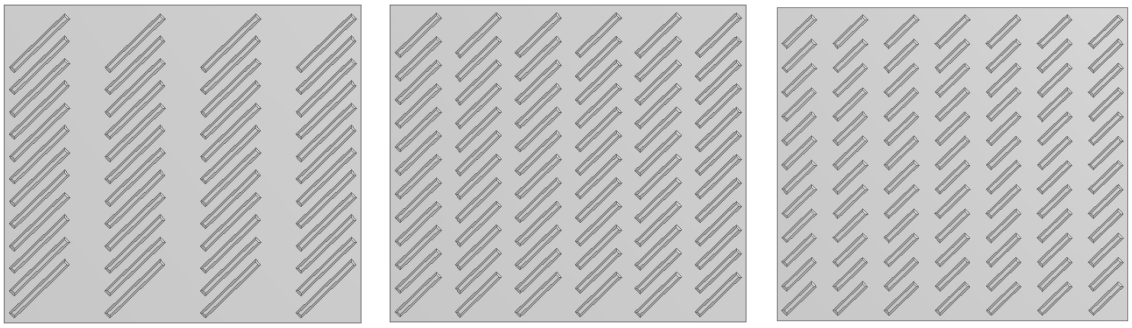

Figure 5.1 Proposed geometries in the parametric study for future work with various column numbers

References

[1] A. Trzynadlowski, *Introduction to modern power electronics*, Third Edit. John Wiley & Sons, Inc., 2016.

[2] BCC Research, “Electric Vehicles and Fuel Cell Vehicles: Global Markets to 2022,” 2018.

[3] MarketsAndMarkets, “Power Electronics Market by Material, Device Type, Application, Vertical, and Geography - Global Forecast 2023,” 2018.

[4] P. Y. Yu and M. Cardona, *Fundamentals of Semiconductors*. Springer, 2010.

[5] J. C. Whitaker, *The Electronics handbook*. CRC Press, 2013.

[6] N. Patin, *Power Electronics Applied to Industrial Systems and Transports*, First Edit. ISTE Press - Elsevier, 2016.

[7] Y. Shabany, *Heat Transfer: Thermal Management Of Electronics*. CRC Press, 2010.

[8] S. S. ANANDAN and V. Ramalingam, “Thermal Management of Electronics: A review of Literature,” vol. 12, pp. 5–26, 2008.

[9] G. Mostafavi, “Natural convective heat transfer from interrupted rectangular fins,” Simon Fraser University, 2012.

[10] M. Ohadi and J. Qi, “Thermal Management of Harsh-Environment Electronics,” in *Microscale Heat Transfer Fundamentals and Applications*, 2006, pp. 479–498.

[11] B. Shang, Y. Ma, R. Hu, C. Yuan, J. Hu, and X. Luo, “Passive thermal management system for downhole electronics in harsh thermal environments,” *Appl. Therm. Eng.*, vol. 118, pp. 593–599, May 2017.

[12] Y. A. Çengel, *Introduction to thermodynamics and heat transfer*, Fifith Edi. CRC Press, 2008.

[13] BCC Research, “The Market for Thermal Management Technologies - SMC024L,”

2019.

[14] J. Edwards and J. Chaddock, “An experimental investigation of the radiation and free convection heat transfer from a cylindrical disk extended surface,” *ASHRAE Trans.*, vol. 69, no. 1, pp. 313–322, 1963.

[15] E. M. Sparrow and S. B. Vemuri, “Natural Convection/Radiation Heat Transfer From Highly Populated Pin Fin Arrays,” *J. Heat Transf.*, vol. 107, p. 190, 1985.

[16] V. Rammohan Rao and S. P. Venkateshan, “Experimental study of free convection and radiation in horizontal fin arrays,” *Int. J. Heat Mass Transf.*, vol. 39, no. 4, pp. 779–789, 1996.

[17] V. D. Rao, S. V Naidu, B. G. Rao, and K. V Sharma, “Heat transfer from a horizontal fin array by natural convection and radiation-A conjugate analysis,” *Int. J. Heat Mass Transf.*, vol. 49, no. 19–20, pp. 3379–3391, 2006.

[18] S. H. Yu, D. Jang, and K. S. Lee, “Effect of radiation in a radial heat sink under natural convection,” *Int. J. Heat Mass Transf.*, vol. 55, no. 1–3, pp. 505–509, 2012.

[19] A. Tamayol *et al.*, “Assessment of thermal performance of electronic enclosures with rectangular fins: a passive thermal solution,” in *InterPACK2011*, 2011.

[20] G. Guglielmini, E. Nannei, and G. Tanda, “Natural convection and radiation heat transfer from staggered vertical fins,” *Int. J. Heat Mass Transf.*, vol. 30, no. 9, pp. 1941–1948, Sep. 1987.

[21] T. Aihara, S. Maruyama, and S. Kobayakawa, “Free convective/radiative heat transfer from pin-fin arrays with a vertical base plate (general representation of heat transfer performance),” *Int. J. Heat Mass Transf.*, vol. 33, no. 6, pp. 1223–1232, Jun. 1990.

[22] W. Lee and S. Park, “Porous Anodic Aluminum Oxide: Anodization and Templated Synthesis of Functional Nanostructures,” *Chem. Rev.*, vol. 114, no. 15, pp. 7487–7556, 2014.

[23] P. G. Sheasby, R. Pinner, and S. Wernick, *The surface treatment and finishing of*

aluminium and its alloys. ASM International, 2001.

[24] G. Goeminne, H. Terryn, and J. Vereecken, “Characterisation of conversion layers on aluminium by means of electrochemical impedance spectroscopy,” Elsevicr Science Ltd, 1995.

[25] L. Bouchama, N. Azzouz, N. Boukmouche, J. P. Chopart, A. L. Daltin, and Y. Bouznit, “Enhancing aluminum corrosion resistance by two-step anodizing process,” *Surf. Coatings Technol.*, vol. 235, pp. 676–684, Nov. 2013.

[26] A. C. Harkness and L. Young, “High resistance anodic oxide films on aluminium,” *Can. J. Chem.*, vol. 44, no. 20, pp. 2409–2413, Oct. 1966.

[27] “Anodic coating for aluminum and aluminum alloys - MIL-A-8625F,” 2003.

[28] J. T. Bevans, W. D. Miller, G. L. Brown, K. E. Nelson, E. E. Luedke, and D. A. Russell, “An investigation of the thermal radiation properties of certain spacecraft materials,” NASA Technical Report, 1962.

[29] J. R. Lowery, “Solar absorption characteristics of several coatings and surface finishes,” NASA.

[30] J. H. Hemmer, “Solar Absorptance and Thermal Emittance of Some Common Spacecraft Thermal-Control Coatings,” NASA Technical Report, 1984.

[31] J. L. Golden, “Anodized aluminum on LDEF*,” NASA.

[32] A. C. Tribble, R. Lukins, E. Watts, S. F. Naumov, and V. K. Sergeev, “Low Earth Orbit Thermal Control Coatings Exposure Flight Tests: A Comparison of U.S. and Russian Results,” NASA, 1995.

[33] C. Siva Kumar, A. K. Sharma, K. N. Mahendra, and S. M. Mayanna, “Studies on anodic oxide coating with low absorptance and high emittance on aluminum alloy 2024,” *Sol. Energy Mater. Sol. Cells*, vol. 60, no. 1, pp. 51–57, Jan. 2000.

[34] J. Lee, D. Kim, C. Choi, and W. Chung, “Nano Energy Nanoporous anodic alumina oxide layer and its sealing for the enhancement of radiative heat dissipation of aluminum alloy,” *Nano Energy*, vol. 31, no. November 2016, pp.

504–513, 2017.

[35] A. Bar-Cohen and W. M. Rohsenow, “Thermally Optimum Spacing of Vertical, Natural Convection Cooled, Parallel Plates,” *Trans. ASME*, vol. 106, no. 1, p. 116, 1984.

[36] D. Van de Pol and J. Tierney, “Free Convection Heat Transfer from Vertical Fin-Arrays,” *IEEE Trans. Parts, Hybrids, Packag.*, vol. 10, no. 4, pp. 267–271, Dec. 1974.

[37] T. Aihara, “Natural convection heat transfer from vertical rectangular-fin arrays : Part 2, heat transfer from fin-edges,” *Bulltin JSME*, vol. 13, no. 64, pp. 1182–1191, 1970.

[38] T. Aihara, “Natural convection heat transfer from vertical recangular-fin arrays : Part 3, heat transfer from fin-flats),” *Bulltin JSME*, vol. 13, no. 64, pp. 1192–1200, 1970.

[39] T. Aihara, “Natural convection heat transfer from vertical rectangular-fin arrays : Part 4, heat transfer characteristics of nonisothermal-fin arrays,” *Bulltin JSME*, vol. 14, no. 74, pp. 818–828, 1971.

[40] W. Elenbaas, “Heat dissipation of parallel plates by free convection,” *Physica*, vol. 9, no. 1, pp. 1–28, Jan. 1942.

[41] S. W. Churchill, “A comprehensive correlating equation for buoyancy-induced flow in channels,” *Lett. Heat Mass Transf.*, vol. 4, no. 3, pp. 193–199, May 1977.

[42] J. R. Bodoia and J. F. Osterle, “The Development of Free Convection Between Heated Vertical Plates,” *J. Heat Transfer*, vol. 84, no. 1, p. 40, Feb. 1962.

[43] E. M. Sparrow and S. Acharya, “A Natural Convection Fin with a Solution-Determined Nonmonotonically Varying Heat Transfer Coefficient,” *J. Heat Transfer*, vol. 103, no. 2, p. 218, May 1981.

[44] F. Harahap and H. N. McManus, “Natural Convection Heat Transfer From Horizontal Rectangular Fin Arrays,” *J. Heat Transfer*, vol. 89, no. 1, p. 32, Feb. 1967.

[45] C. D. Jones and L. F. Smith, “Optimum Arrangement of Rectangular Fins on Horizontal Surfaces for Free-Convection Heat Transfer,” *J. Heat Transfer*, vol. 92, no. 1, p. 6, Feb. 1970.

[46] F. Harahap and D. Setio, “Correlations for heat dissipation and natural convection heat-transfer from horizontally-based, vertically-finned arrays,” *Appl. Energy*, vol. 69, no. 1, pp. 29–38, May 2001.

[47] K. E. Starner and H. N. McManus, “An Experimental Investigation of Free-Convection Heat Transfer From Rectangular-Fin Arrays,” *J. Heat Transfer*, vol. 85, no. 3, p. 273, Aug. 1963.

[48] C. W. Leung and S. D. Probert, “Heat-exchanger performance: Effect of orientation,” *Appl. Energy*, vol. 33, no. 4, pp. 235–252, Jan. 1989.

[49] Q. Shen, D. Sun, Y. Xu, T. Jin, and X. Zhao, “Orientation effects on natural convection heat dissipation of rectangular fin heat sinks mounted on LEDs,” *Int. J. Heat Mass Transf.*, vol. 75, pp. 462–469, Aug. 2014.

[50] I. Tari and M. Mehrtash, “Natural convection heat transfer from horizontal and slightly inclined plate-fin heat sinks,” *Appl. Therm. Eng.*, vol. 61, no. 2, pp. 728–736, Nov. 2013.

[51] Incropera, DeWitt, Bergman, and Lavine, “Fundamentals Of Heat And Mass Transfer.” John Wiley, p. 997, 2006.

[52] B. R. Rich, “An investigation of heat transfer from an inclined flat plate in free convection,” *Trans. ASME*, vol. 75, pp. 489–499, 1953.

[53] W. T. Kierkus, “An analysis of laminar free convection flow and heat transfer about an inclined isothermal plate,” *Int. J. Heat Mass Transf.*, vol. 11, no. 2, pp. 241–253, Feb. 1968.

[54] J. B. Lee and G. S. H. Lock, “Laminar Boundary~Layer Free Convection along an Inclined, Isothermal Surface,” *Trans. Can. Soc. Mech. Eng.*, vol. 1, no. 4, pp. 189–196, Dec. 1972.

[55] G. C. Vliet, “Natural Convection Local Heat Transfer on Constant-Heat-Flux

Inclined Surfaces," *J. Heat Transfer*, vol. 91, no. 4, p. 511, Nov. 1969.

[56] T. Fujii and H. Imura, "Natural-convection heat transfer from a plate with arbitrary inclination," *Int. J. Heat Mass Transf.*, vol. 15, no. 4, pp. 755–767, Apr. 1972.

[57] H. Shaukatullah and B. Gebhart, "An experimental investigation of natural convection flow on an inclined surface," *Int. J. Heat Mass Transf.*, vol. 21, no. 12, pp. 1481–1490, Dec. 1978.

[58] L. Pera and B. Gebhart, "On the stability of natural convection boundary layer flow over horizontal and slightly inclined surfaces," *Int. J. Heat Mass Transf.*, vol. 16, no. 6, pp. 1147–1163, Jun. 1973.

[59] J. . Lloyd, E. . Sparrow, and E. R. . Eckert, "Laminar, transition and turbulent natural convection adjacent to inclined and vertical surfaces," *Int. J. Heat Mass Transf.*, vol. 15, no. 3, pp. 457–473, Mar. 1972.

[60] M. Al-Arabi and B. Sakr, "Natural convection heat transfer from inclined isothermal plates," *Int. J. Heat Mass Transf.*, vol. 31, no. 3, pp. 559–566, Mar. 1988.

[61] J. J. Wei, B. Yu, H. S. Wang, and W. Q. Tao, "Numerical study of simultaneous natural convection heat transfer from both surfaces of a uniformly heated thin plate with arbitrary inclination," *Heat Mass Transf.*, vol. 38, no. 4–5, pp. 309–317, Apr. 2002.

[62] O. Hiroyuki, S. Hayatoshi, and S. W. Churchill, "Natural convection in an inclined square channel," *Int. J. Heat Mass Transf.*, vol. 17, no. 3, pp. 401–406, Mar. 1974.

[63] H. Ozoe, H. Sayama, and S. W. Churchill, "Natural convection in an inclined rectangular channel at various aspect ratios and angles—experimental measurements," *Int. J. Heat Mass Transf.*, vol. 18, no. 12, pp. 1425–1431, Dec. 1975.

[64] L. F. A. Azevedo and E. M. Sparrow, "Natural Convection in Open-Ended Inclined Channels," *J. Heat Transfer*, vol. 107, no. 4, p. 893, 1985.

[65] Y. Varol, H. F. Oztop, A. Koca, and F. Ozgen, "Natural convection and fluid flow in inclined enclosure with a corner heater," *Appl. Therm. Eng.*, vol. 29, no. 2–3, pp.

340–350, Feb. 2009.

[66] O. Hiroyuki, Y. Kazumitsu, S. Hayatoshi, and S. W. Churchill, “Natural circulation in an inclined rectangular channel heated on one side and cooled on the opposing side,” *Int. J. Heat Mass Transf.*, vol. 17, no. 10, pp. 1209–1217, Oct. 1974.

[67] C. Y. Choi and A. Ortega, “Mixed convection in an inclined channel with a discrete heat source,” in *[1992 Proceedings] Intersociety Conference on Thermal Phenomena in Electronic Systems*, pp. 40–48.

[68] S. Kiwan and M. Khodier, “Natural convection heat transfer in an open-ended inclined channel-partially filled with porous media,” *Heat Transf. Eng.*, vol. 29, no. 1, pp. 67–75, Jan. 2008.

[69] J. Cadafalch, A. Oliva, G. Van Der Graaf, and X. Albets, “Natural Convection in a Large, Inclined Channel With Asymmetric Heating and Surface Radiation,” 2003.

[70] J. N. Arnold, I. Catton, and D. K. Edwards, “Experimental Investigation of Natural Convection in Inclined Rectangular Regions of Differing Aspect Ratios,” *J. Heat Transfer*, vol. 98, no. 1, p. 67, Feb. 2010.

[71] H. X. Yang and Z. J. Zhu, “Numerical study on transient laminar natural convection in an inclined parallel- walled channel,” *Int. Commun. Heat Mass Transf.*, vol. 30, no. 3, pp. 359–367, Apr. 2003.

[72] M. Fujii, “Enhancement of natural convection heat transfer from a vertical heated plate using inclined fins,” *Heat Transf. - Asian Res.*, vol. 36, no. 6, pp. 334–344, 2007.

[73] A. K. da Silva, S. Lorente, and A. Bejan, “Optimal distribution of discrete heat sources on a wall with natural convection,” *Int. J. Heat Mass Transf.*, vol. 47, no. 2, pp. 203–214, Jan. 2004.

[74] N. Sobel, F. Landis, and W. Mueller, “Natural convection heat transfer in short vertical channels including effects of stagger,” *Proc. 3rd Int. Heat Transf. Conf.*, vol. 2, no. 1, pp. 121–125, 1966.

[75] E. M. Sparrow and C. Prakash, “Enhancement of Natural Convection Heat

Transfer by a Staggered Array of Discrete Vertical Plates," *J. Heat Transfer*, vol. 102, no. 2, p. 215, May 2009.

[76] M. S. S. S. Rao and V. M. K. Sastri, "Natural convection heat transfer in staggered vertical channels," *Comput. Methods Appl. Mech. Eng.*, vol. 113, no. 3–4, pp. 263–269, Mar. 1994.

[77] A. Daloglu and T. Ayhan, "Natural convection in a periodically finned vertical channel," *Int. Commun. Heat Mass Transf.*, vol. 26, no. 8, pp. 1175–1182, Nov. 1999.

[78] V. G. Gorobets, "Heat Transfer for Vertical Surfaces with Discrete Fins in the Case of Free Convection," *J. Eng. Phys. Thermophys.*, vol. 75, no. 5, pp. 1130–1138, 2002.

[79] M. Ahmadi, G. Mostafavi, and M. Bahrami, "Natural convection from rectangular interrupted fins," *Int. J. Therm. Sci.*, vol. 82, pp. 62–71, Aug. 2014.

[80] M. Ahmadi, G. Mostafavi, and M. Bahrami, "Natural Convection From Interrupted Vertical Walls," *J. Heat Transfer*, vol. 136, no. 11, p. 112501, Sep. 2014.

[81] M. Ahmadi, "Pushing the Limits of Natural Convection Heat Transfer from the Heatsinks," Simon Fraser University, 2014.

[82] M. Ahmadi, M. F. Pakdaman, and M. Bahrami, "Pushing the limits of vertical naturally-cooled heatsinks; Calculations and design methodology," *Int. J. Heat Mass Transf.*, vol. 87, pp. 11–23, Aug. 2015.

[83] T. Aihara, S. Maruyama, and S. Kobayakawa, "Free convective/radiative heat transfer from pin-fin arrays with a vertical base plate (general representation of heat transfer performance)," *Int. J. Heat Mass Transf.*, vol. 33, no. 6, pp. 1223–1232, 1990.

[84] A. I. Zografos and J. Edward Sunderland, "Natural convection from pin fin arrays," *Exp. Therm. Fluid Sci.*, vol. 3, no. 4, pp. 440–449, 1990.

[85] M. Iyengar and A. Bar-Cohen, "Least-material optimization of vertical pin-fin, plate-fin, and triangular-fin heat sinks in natural convective heat transfer," in

ITherm'98. Sixth Intersociety Conference on Thermal and Thermomechanical Phenomena in Electronic Systems (Cat. No.98CH36208), 2002, pp. 295–302.

[86] Y. Joo and S. J. Kim, "Comparison of thermal performance between plate-fin and pin-fin heat sinks in natural convection," *Int. J. Heat Mass Transf.*, vol. 83, pp. 345–356, 2015.

[87] T. S. Fisher and K. E. Torrance, "Free Convection Limits for Pin-Fin Cooling," *J. Heat Transfer*, vol. 120, no. 3, p. 633, Aug. 1998.

[88] D. Sahray, H. Shmueli, G. Ziskind, and R. Letan, "Study and Optimization of Horizontal-Base Pin-Fin Heat Sinks in Natural Convection and Radiation," *J. Heat Transfer*, vol. 132, no. 1, p. 012503, Jan. 2009.

[89] R. N. Lumley, *Fundamentals of aluminium metallurgy : production, processing and applications*. Woodhead Pub, 2011.

[90] "The Process of Anodizing | Spectral Finishing." [Online]. Available: http://spectralfinishing.ca/home/the-process-of-anodizing/ [Accessed, 20 June 2019].

[91] ASTM, "Standard Test Methods for Total Normal Emittance of Surfaces Using Inspection-Meter Techniques," *Annu. B. ASTM Stand.*, vol. 71, no. July 1971, pp. 4–6, 1996.

[92] D. A. Jaworske, "Portable infrared reflectometer for evaluating emittance," vol. 791, no. February 2001, pp. 791–796, 2003.

[93] Microelectronics Heat Transfer Laboratory, "Fluid Properties Calculator," 1997. [Online]. Available: http://www.mhtl.uwaterloo.ca/old/onlinetools/airprop/airprop.html. [Accessed: 12-May-2019].

[94] ANSYS Corp., "Ansys Fluent Help Version 17.2." 2016.

[95] A. Sce and L. Caporale, "High Density Die Casting (HDDC): New frontiers in the manufacturing of heat sinks," *J. Phys. Conf. Ser.*, vol. 525, no. 1, pp. 0–10, 2014.

Appendix A. Spectral hemispherical emissivity.

The spectral hemispherical emissivity is defined as Eq.2.7 from section 2.2.2. This section is providing the detailed data from the measurement, and the measured spectral data are in a range from 2μm to 25μm.

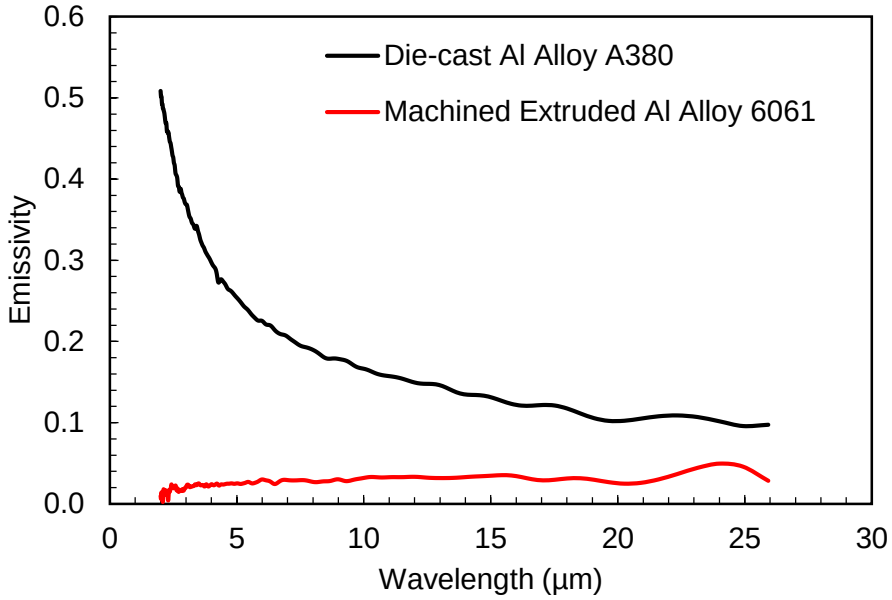

Figure A1 Spectral hemispherical emissivity for aluminum alloys surfaces

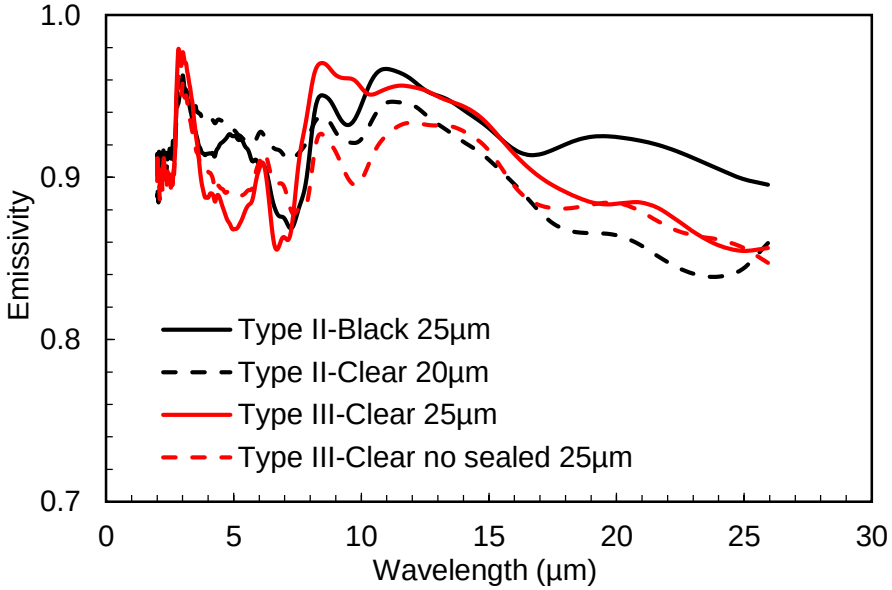

Figure A2 Spectral hemispherical emissivity for die-cast Al alloy A380 surfaces after various types of anodization

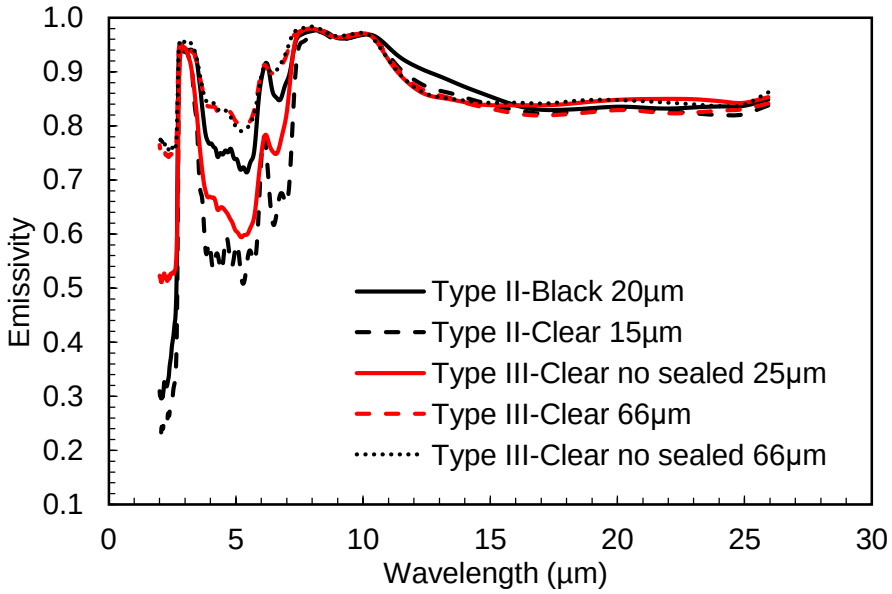

Figure A3 Spectral hemispherical emissivity for machined Al alloy 6061 surfaces after various types of anodization

The actually prepared samples for the emissivity measurement are showing in Figure A4. and A5. The corresponding anodized types are indicating on the top of each sample.

Figure A4 Bare and anodized die-cast aluminum A380 samples

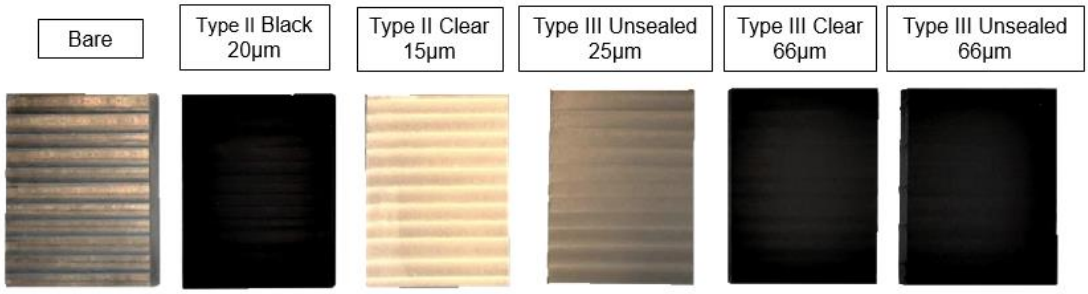

Figure A5 Bare and anodized machined aluminum 6061 samples

Appendix B. Tabulated data from experiments of bare and anodized IC650 heat sinks.

Table B1 Experimental data of bare IC650 heat sinks

Bare IC650 Heat sinks [Average]				
Thermal Power(W)	20	40	60	80
Temperature Difference (℃)	17.6	29.1	38.9	49.6
Standard Deviation	0.09	0.63	0.48	0.59
Ambient Temperature (℃)	27.7	31.6	35.2	38.0
Chamber Wall Temperature (℃)	25.5	28.1	31.0	32.0

Table B2 Experimental data of Type II-Balck anodized IC650 heat sinks

Type II-Black Anodized IC650 Heat sinks [Average]				
Thermal Power(W)	20	40	60	80
Temperature Difference (℃)	15.0	25.2	34.2	43.0
Standard Deviation	0.42	0.43	0.20	0.19
Ambient Temperature (℃)	27.6	30.9	35.2	38.1
Chamber Wall Temperature (℃)	26.0	28.0	30.9	32.9

Table B3 Experimental data of Type III-Clear anodized IC650 heat sinks

Type III-Clear Anodized IC650 Heat sinks [Average]				
Thermal Power(W)	20	40	60	80
Temperature Difference (℃)	15.0	25.7	34.3	42.6
Standard Deviation	0.38	0.20	0.33	0.07
Ambient Temperature (℃)	27.5	31.0	35.0	38.9
Chamber Wall Temperature (℃)	25.8	27.5	30.5	33.6

Appendix C. Tabulated data from experiments of bare and anodized prototyped heat sinks.

Table C1 Experimental data of bare IC650 Inclined Fins at horizontal orientation

Bare IC650 Inclined Fins [Horizontal]					
Thermal Power(W)	20	40	60	80	100
Temperature Difference (℃)	15.0	24.1	32.7	40.2	47.3
Standard Deviation	0.08	0.12	0.14	0.16	0.22
Ambient Temperature (℃)	28.7	33.1	37.1	39.9	43.4
Chamber Wall Temperature (℃)	25.6	28.2	30.2	31.5	33.5

Table C2 Experimental data of bare IC650 Inclined Fins at Vertical orientation

Bare IC650 Inclined Fins [Vertical]					
Thermal Power(W)	20	40	60	80	100
Temperature Difference (℃)	18.5	29.7	40.0	49.2	58.0
Standard Deviation	0.09	0.12	0.14	0.06	0.04
Ambient Temperature (℃)	28.4	32.1	35.5	38.8	41.8
Chamber Wall Temperature (℃)	25.4	27.3	28.9	30.6	32.1

Table C3 Experimental data of bare IC650 Inclined Fins at Sideways orientation

Bare IC650 Inclined Fins [Sideways]					
Thermal Power(W)	20	40	60	80	100
Temperature Difference (℃)	19.6	31.4	42.2	52.3	61.6
Standard Deviation	0.29	0.35	0.18	0.35	0.45
Ambient Temperature (℃)	27.5	31.4	34.7	37.4	39.6
Chamber Wall Temperature (℃)	25.4	27.8	29.4	30.9	31.6

Table C4 Experimental data of anodized IC650 Inclined Fins at Horizontal orientation

Anodized IC650 Inclined Fins [Horizontal]					
Thermal Power(W)	20	40	60	80	100
Temperature Difference (℃)	12.9	20.9	28.4	34.9	41.0
Standard Deviation	0.15	0.14	0.28	0.26	0.14
Ambient Temperature (℃)	25.7	29.1	32.3	34.7	37.5
Chamber Wall Temperature (℃)	24.2	26.5	28.6	30.1	31.9

Table C5 Experimental data of anodized IC650 Inclined Fins at Vertical orientation

Anodized IC650 Inclined Fins [Vertical]					
Thermal Power(W)	20	40	60	80	100
Temperature Difference (℃)	15.9	25.9	35.1	43.1	50.4
Standard Deviation	0.05	0.16	0.12	0.15	0.16
Ambient Temperature (℃)	28.0	31.4	34.4	36.8	39.0
Chamber Wall Temperature (℃)	26.7	29.2	31.1	32.5	33.8

Table C6 Experimental data of anodized IC650 Inclined Fins at Sideways orientation

Anodized IC650 Inclined Fins [Sideways]					
Thermal Power(W)	20	40	60	80	100
Temperature Difference (℃)	17.4	27.9	37.4	45.8	53.6
Standard Deviation	0.15	0.05	0.17	0.26	0.23
Ambient Temperature (℃)	24.9	27.7	30.2	32.1	35.0
Chamber Wall Temperature (℃)	24.8	27.6	29.9	31.2	33.7

Table C7 Experimental data of bare Inclined Interrupted Fins at Horizontal orientation

Bare Inclined Interrupted Fins [Horizontal]					
Thermal Power(W)	20	40	60	80	100
Temperature Difference (℃)	12.1	20.0	27.5	34.5	40.8
Standard Deviation	0.16	0.14	0.09	0.05	0.13
Ambient Temperature (℃)	29.2	33.8	37.6	40.5	43.9
Chamber Wall Temperature (℃)	25.7	28.1	30.1	31.4	33.2

Table C8 Experimental data of bare Inclined Interrupted Fins at Vertical orientation

Bare Inclined Interrupted Fins [Vertical]					
Thermal Power(W)	20	40	60	80	100
Temperature Difference (℃)	16.5	26.6	36.1	44.5	52.8
Standard Deviation	0.02	0.07	0.08	0.18	0.27
Ambient Temperature (℃)	27.8	31.1	34.6	37.1	40.4
Chamber Wall Temperature (℃)	25.6	27.2	29.2	30.6	32.5

Table C9 Experimental data of bare Inclined Interrupted Fins at Sideways orientation

Bare Inclined Interrupted Fins [Sideways]					
Thermal Power(W)	20	40	60	80	100
Temperature Difference (℃)	16.7	27.6	37.6	46.3	54.7
Standard Deviation	0.04	0.13	0.15	0.19	0.16
Ambient Temperature (℃)	24.7	28.0	31.3	33.9	35.9
Chamber Wall Temperature (℃)	23.1	26.2	29.0	30.9	32.2

Table C10 Experimental data of anodized Inclined Interrupted Fins at Horizontal orientation

Anodized Inclined Interrupted Fins [Horizontal]					
Thermal Power(W)	20	40	60	80	100
Temperature Difference (℃)	11.6	18.9	25.8	31.7	37.4
Standard Deviation	0.21	0.19	0.16	0.27	0.17
Ambient Temperature (℃)	25.3	28.8	31.3	33.3	36.2
Chamber Wall Temperature (℃)	24.4	26.8	28.0	28.9	31.1

Table C11 Experimental data of anodized Inclined Interrupted Fins at Vertical orientation

Anodized Inclined Interrupted Fins [Vertical]					
Thermal Power(W)	20	40	60	80	100
Temperature Difference (℃)	13.8	22.6	30.7	37.7	44.3
Standard Deviation	0.08	0.03	0.25	0.27	0.41
Ambient Temperature (℃)	24.6	28.4	30.9	32.6	34.7
Chamber Wall Temperature (℃)	23.7	26.9	28.4	29.1	30.4

Table C12 Experimental data of anodized Inclined Interrupted Fins at Sideways orientation

Anodized Inclined Interrupted Fins [Sideways]					
Thermal Power(W)	20	40	60	80	100
Temperature Difference (℃)	14.7	24.1	32.8	40.6	48.1
Standard Deviation	0.02	0.03	0.02	0.06	0.18
Ambient Temperature (℃)	24.9	26.9	28.8	30.1	35.4
Chamber Wall Temperature (℃)	24.1	25.5	27.1	28.0	33.2

Table C13 Experimental data of bare Straight Interrupted Fins at Horizontal orientation

Bare Straight Interrupted Fins [Horizontal]					
Thermal Power(W)	20	40	60	80	100
Temperature Difference (℃)	12.0	19.7	26.8	33.1	39.3
Standard Deviation	0.05	0.08	0.05	0.13	0.10
Ambient Temperature (℃)	28.3	32.4	36.4	39.5	42.6
Chamber Wall Temperature (℃)	25.3	27.7	29.9	31.5	33.1

Table C14 Experimental data of bare Straight Interrupted Fins at Vertical orientation

Bare Straight Interrupted Fins [Vertical]					
Thermal Power(W)	20	40	60	80	100
Temperature Difference (℃)	15.3	24.9	33.6	41.7	49.4
Standard Deviation	0.17	0.27	0.21	0.22	0.15
Ambient Temperature (℃)	25.6	29.4	33.3	36.3	39.0
Chamber Wall Temperature (℃)	23.0	25.1	26.9	28.4	29.6

Table C15 Experimental data of bare Straight Interrupted Fins at Sideways orientation

Bare Straight Interrupted Fins [Sideways]					
Thermal Power(W)	20	40	60	80	100
Temperature Difference (℃)	19.6	31.5	42.5	52.4	62.0
Standard Deviation	0.34	0.41	0.32	0.42	0.83
Ambient Temperature (℃)	27.7	31.6	35.1	39.9	43.5
Chamber Wall Temperature (℃)	23.6	25.0	26.1	28.9	30.9

Table C16 Experimental data of anodized Straight Interrupted Fins at Horizontal orientation

Anodized Straight Interrupted Fins [Horizontal]					
Thermal Power(W)	20	40	60	80	100
Temperature Difference (℃)	10.1	16.6	22.7	28.2	33.5
Standard Deviation	0.05	0.06	0.24	0.13	0.28
Ambient Temperature (℃)	30.9	30.2	33.1	35.7	38.6
Chamber Wall Temperature (℃)	26.2	25.7	27.2	28.6	30.5

Table C17 Experimental data of anodized Straight Interrupted Fins at Vertical orientation.

Anodized Straight Interrupted Fins [Vertical]					
Thermal Power(W)	20	40	60	80	100
Temperature Difference (℃)	12.9	21.2	29.0	35.8	42.2
Standard Deviation	0.02	0.08	0.06	0.20	0.12
Ambient Temperature (℃)	26.8	30.1	32.3	34.2	36.4
Chamber Wall Temperature (℃)	24.8	26.7	27.8	28.7	30.0

Table C18 Experimental data of anodized Straight Interrupted Fins at Sideways orientation

Anodized Straight Interrupted Fins [Sideways]					
Thermal Power(W)	20	40	60	80	100
Temperature Difference (℃)	17.2	28.0	37.5	46.3	54.5
Standard Deviation	0.18	0.06	0.04	0.12	0.48
Ambient Temperature (℃)	24.6	26.1	28.1	33.0	36.9
Chamber Wall Temperature (℃)	22.9	23.4	24.3	28.3	31.4

Table C19 Experimental data of bare Pin Fins at Horizontal orientation

Bare Pin Fins [Horizontal]					
Thermal Power(W)	20	40	60	80	100
Temperature Difference (℃)	12.1	19.5	26.2	32.3	38.0
Standard Deviation	0.20	0.39	0.37	0.69	0.38
Ambient Temperature (℃)	28.6	32.8	36.8	39.8	43.3
Chamber Wall Temperature (℃)	25.4	27.8	29.9	31.2	32.7

Table C20 Experimental data of bare Pin Fins at Vertical orientation

Bare Pin Fins [Vertical]					
Thermal Power(W)	20	40	60	80	100
Temperature Difference (℃)	18.6	29.9	40.4	49.4	58.0
Standard Deviation	0.09	0.20	0.26	0.31	0.36
Ambient Temperature (℃)	25.9	29.6	32.8	35.8	38.6
Chamber Wall Temperature (℃)	23.8	25.6	27.0	28.6	29.8

Table C21 Experimental data of bare Pin Fins at Sideways orientation

Bare Pin Fins [Sideways]					
Thermal Power(W)	20	40	60	80	100
Temperature Difference (℃)	19.7	31.3	41.9	51.6	60.9
Standard Deviation	0.14	0.03	0.30	0.29	0.27
Ambient Temperature (℃)	26.7	29.8	33.2	36.0	39.2
Chamber Wall Temperature (℃)	24.3	25.7	27.1	28.1	29.2

Table C22 Experimental data of anodized Pin Fins at Horizontal orientation

Anodized Pin Fins [Horizontal]					
Thermal Power(W)	20	40	60	80	100
Temperature Difference (℃)	11.3	18.5	24.9	30.5	36.0
Standard Deviation	0.15	0.11	0.25	0.44	0.17
Ambient Temperature (℃)	26.9	29.7	33.4	38.2	41.1
Chamber Wall Temperature (℃)	24.9	27.0	29.8	33.5	35.5

Table C23 Experimental data of anodized Pin Fins at Vertical orientation

Anodized Pin Fins [Vertical]					
Thermal Power(W)	20	40	60	80	100
Temperature Difference (℃)	15.2	24.9	33.7	41.5	49.1
Standard Deviation	0.10	0.16	0.13	0.26	0.20
Ambient Temperature (℃)	27.1	30.0	32.3	34.7	37.0
Chamber Wall Temperature (℃)	25.3	27.0	28.2	29.8	31.5

Table C24 Experimental data of anodized Pin Fins at Sideways orientation

Anodized Pin Fins [Sideways]					
Thermal Power(W)	20	40	60	80	100
Temperature Difference (℃)	16.2	26.5	36.0	44.3	52.1
Standard Deviation	0.07	0.11	0.03	0.02	0.07
Ambient Temperature (℃)	27.9	30.8	32.8	34.7	36.6
Chamber Wall Temperature (℃)	26.3	28.3	29.4	30.6	31.8

Table C25 Experimental data of bare Inclined Interrupted Fins [12 fins each column] tested at horizontal orientation outside the box

Bare Inclined Interrupted Fins (12) [Outside box] [Horizontal]					
Thermal Power(W)	20	40	60	80	100
Temperature Difference (℃)	14.3	23.5	31.9	39.3	46.2
Standard Deviation	0.11	0.22	0.16	0.33	0.30
Chamber Ambient Temperature (℃)	19.77	19.87	20.11	19.78	19.37

Table C26 Experimental data of bare Inclined Interrupted Fins [12 fins each column] tested at vertical orientation outside the box

Bare Inclined Interrupted Fins (12) [Outside box] [Vertical]					
Thermal Power(W)	20	40	60	80	100
Temperature Difference (℃)	17.64	28.10	37.72	45.70	53.53
Standard Deviation	0.06	0.27	0.71	0.36	0.34
Chamber Ambient Temperature (℃)	20.26	20.46	20.52	20.00	19.75

Table C27 Experimental data of bare Inclined Interrupted Fins [12 fins each column] tested at sideways orientation outside the box

Bare Inclined Interrupted Fins (12) [Outside box] [Sideways]					
Thermal Power(W)	20	40	60	80	100
Temperature Difference (℃)	17.45	28.44	36.29	46.84	54.27
Standard Deviation	0.57	0.83	0.44	1.57	1.78
Chamber Ambient Temperature (℃)	20.21	19.84	19.80	19.78	19.94

Table C28 Experimental data of bare Inclined Interrupted Fins [14 fins each column] tested at Horizontal orientation outside the box

Bare Inclined Interrupted Fins (14) [Outside box] [Horizontal]					
Thermal Power(W)	20	40	60	80	100
Temperature Difference (℃)	14.55	23.12	30.57	37.80	43.83
Standard Deviation	0.21	0.04	0.44	0.50	0.82
Chamber Ambient Temperature (℃)	22.59	21.99	22.55	22.43	22.58

Table C29 Experimental data of bare Inclined Interrupted Fins [14 fins each column] tested at Vertical orientation outside the box

Bare Inclined Interrupted Fins (14) [Outside box] [Vertical]					
Thermal Power(W)	20	40	60	80	100
Temperature Difference (℃)	17.16	28.17	38.65	47.43	53.97
Standard Deviation	0.46	0.35	0.12	0.14	1.77
Chamber Ambient Temperature (℃)	22.40	22.24	21.95	22.70	23.32

Table C30 Experimental data of bare Inclined Interrupted Fins [14 fins each column] tested at Sideways orientation outside the box

Bare Inclined Interrupted Fins (14) [Outside box] [Sideways]					
Thermal Power(W)	20	40	60	80	100
Temperature Difference (℃)	17.66	29.41	39.41	48.18	56.07
Standard Deviation	0.34	0.21	0.75	0.85	0.29
Chamber Ambient Temperature (℃)	23.20	22.72	22.14	22.59	22.78